

UNIVERSITY OF BIRMINGHAM

EXPERIMENTAL INVESTIGATION OF THE NON-UNIFORMITY OF JETS' VELOCITIES EXITING A MULTI-HOLE INJECTOR

By

CARLO CORATELLA

A thesis submitted to the University of Birmingham for the degree of

DOCTOR OF PHILOSOPHY

Department of Mechanical Engineering

University of Birmingham

January 2021

UNIVERSITY OF
BIRMINGHAM

University of Birmingham Research Archive

e-theses repository

This unpublished thesis/dissertation is copyright of the author and/or third parties. The intellectual property rights of the author or third parties in respect of this work are as defined by The Copyright Designs and Patents Act 1988 or as modified by any successor legislation.

Any use made of information contained in this thesis/dissertation must be in accordance with that legislation and must be properly acknowledged. Further distribution or reproduction in any format is prohibited without the permission of the copyright holder.

ABSTRACT

Over the last few decades, the global demand for vehicular mobility has seen an unstoppable growth on a worldwide scale, setting the stage for a faster depletion of fossil energy. Besides some implications of a geopolitical character, this scenario has also led to an increase in pollution levels. As a consequence, progressively stricter criteria of pollutants' levels from IC engines are being demanded by the emissions' regulations. The automotive field has thereby endeavoured to pursue the minimisation of the environmental impact of IC mobility, directing research efforts towards the development of cutting-edge solutions.

With regard to the fast exhaustion of oil supplies, this issue is deemed to significantly determine radical changes within the global automotive scenario in the next few years. This criticality has urged the automotive field to turn its attention both to investigation of fuel spray and to the development of biofuels, until the worldwide spread of electric vehicles becomes a viable pathway for green mobility.

The work in the present thesis thereby aimed to provide a further perspective when approaching these critical subjects. More specifically, the doctoral research developed an experimental framework to assess the variability of jets' velocities at early stages of injection, employing diesel and methylfuran-based biofuels. The scope was to provide a physical explanation of the combined impact of injection settings with the fuel properties and injector geometry on the uniformity of the jets' development.

The first stage of this study addressed the design of a sensor for the detection of needle lift in a diesel injector. This part was prompted by the key role of needle lift in the characterization of the injection process. Diesel injections were performed, demonstrating that the sensor is able to follow needle displacement over the injection process. Besides the accurate detection of needle motion, peculiarities of the sensor include a largely shorter realization time and a

higher cost effectiveness. With regard to the findings which emerged from the tests, it was observed also that along with injection pressure, backpressure plays a non-negligible impact on the time history of needle displacement over the injection process. More specifically, it emerged that, at unvaried injection pressure, higher backpressures boost needle lift as well as injector closure.

The analysis of the impact of injection settings on needle lift prompted the second stage of the present study. This stage aimed to assess the non-uniformity of diesel jets' velocities. From the tests, it emerged that besides the greater injection pressure, an increase in backpressure minimises the orifice-to-orifice variability of diesel jets' velocities at the early stages of the injection process. In this regard, keeping in mind that needle wobbles contribute to the imbalance of the injected flow rate, the combined impact of injection pressure with backpressure on needle motions was discussed.

The outcomes emerging from the second stage led the author to shift the focus to the combined impact of injection setting with the fuel properties on the variability of jets' velocities. For this purpose, injection tests were performed, employing diesel and 2-methylfuran/diesel blends (here referred to as MF30 and MF50, given the 30% and 50% volumetric content of 2-methylfuran in diesel, respectively). It was observed that MF30 jets' velocities are spread out over a wider range than diesel in most cases; whilst MF50 exhibited the lowest orifice-to-orifice variability. Besides the jets' velocities, the injection delays were also acquired. Afterwards, the combined action of the injection settings with the fuel properties both on the needle off-axis motion and on the injection delays was fully discussed.

The ascertained impact of the injection settings on the jet development prompted the author to assess the injection-induced pressure fluctuations taking place in the rail. Therefore, keeping in mind that injection pressure plays a pivotal role on the uniformity of jets' development, and

as the injection pressure is subjected to variations stemming from the precedent shot, it was deemed necessary to assess the injection-induced pressure fluctuations occurring in the rail. Injection tests were performed employing neat diesel and the aforementioned 2-methylfuran/diesel blends at various injection configurations. Besides the injection settings, the fuel properties of viscosity, surface tension, density, and bulk modulus were found to meaningfully determine rail pressure fluctuations. The injection tests showed that the furan-based blends, provided with greater bulk modulus, are subjected to lower pressure fluctuations, as well as the expected decrease in the injection-induced pressure drop from greater fuel viscosity. Moreover, higher backpressure was found to mitigate the diesel pressure drop within the rail. By contrast, MF30 and MF50 pressure drops tend to increase in response to increasing backpressure. It was observed also that, at unvaried injection pressure and greater backpressures, decreasing viscosity (but still higher than diesel) alleviates the increase in rail pressure drop in most cases.

PUBLICATION RECORD

The doctoral research was addressed to provide clear evidence of the combined impact of injection settings with fuel properties and injector geometry on the variability of jets' velocities. Within this scope, high-fidelity experimental injection tests were conducted, resulting in the following publication record.

Published papers

- **Coratella, C.**, Parry, L., Li, Y., & Xu, H. (2021). 'Experimental Investigation of the Rail Pressure Fluctuations Correlated with Fuel Properties and Injection Settings'. *Automotive Innovation*, 1-12.
- **Coratella, C.**, Parry, L., & Xu, H. (2020). 'Experimental Investigation of Injection Pressure Fluctuations Employing Alternative Fuels' (No. 2020-01-2122). *SAE Technical Paper*.
- **Coratella, C.**, Sahu, A., Parry, L., Xu, H., & Ma, X. (2020). 'Experimental investigation of the orifice-to orifice variability in jet velocities in a diesel injector' *Fuel*, 280, 118353.
- **Coratella, C.**, Parry, L., Sahu, A., & Xu, H. (2019). 'Optical Sensor for the Needle Lift Detection in the Common Rail Injector' (No. 2019-24-0193). *SAE Technical Paper*.
- Wang, C., Sahu, A., **Coratella, C.**, Xu, C., Saul, J., & Xu, H. (2019). 'Spray characteristics of a gasoline-diesel blend (ULG75) using high-speed imaging techniques' *Fuel*, 239, pp. 677-692.

Papers submitted and under peer-review

- **Coratella, C.**, Parry, L., Sahu, A., Li, Y., Xu, H. 'Experimental investigation of the non-uniformity of the diesel jets' velocity distribution compared to 2-methylfuran- based blend'. *Automotive Innovation* journal, AUIN-D-19-000106. Following a minor revision, the revised manuscript has been submitted.

- Wang Z., **Coratella C.**, Fushui Liu F., Xu H., Lee C., 'Experimental investigation on the effects of diesel nozzle geometry on nozzle internal flow and spray primary breakup'. *Automotive Innovation* journal, AUIN-D-20-00044 (under review).

The research activity included also the design of an optical-fibre-based sensor for the detection of needle lift within a diesel injector. Currently the sensor is under PCT patenting procedure.

https://www.birmingham.ac.uk/partners/enterprise/Fuel-injector.aspx

https://micragateway.org/our-services/ip-for-licence/fuel-injector-with-a-piston-motion-sensor/

ACKNOWLEDGEMENTS

A huge acknowledgement must go to Professor Hongming Xu for his constant support and utmost guidance throughout my doctorate. His precious advice and endless patience gave me the courage to believe any goal is accomplishable only with vivid spirit of initiative followed by thorough study and hard work. This work would not have been possible without his countless inputs.

I express my particular thanks to Lewis Parry and Dr Amrit Sahu for providing the needed assistance during the tests. Without their essential support, this research activity would not have had any margin of development.

Thanks also needs to be given to Dr Giulio Vita and Dr Soheil Zeerati Rezaei, who suggested additional background work concerning fluid dynamics applied to internal combustion engines.

I am grateful to the technicians Lee Gauntlett, Peter Thornton and Mark Wager, who always have readily contributed to obtain a highly reliable experimental set-up.

I am grateful to Dr Phil Atkins of the Department of Electronics, Electrical and Systems Engineering of the University of Birmingham, for his precious help in setting up the electric circuit feeding the optical sensor devoted to detect needle lift.

I express my special thanks to Dr Claudio Bordonali, manager of the Turbochargers Department at Seven Diesel S.p.A., for his valuable help in providing me with data useful for my research.

On a personal note, I need to thank my family and my wife Agnieszka for their support over these years. They have filled me with the calm necessary for the achievement of any goal.

I cannot express how thankful I am to my parents and my sister, who have always supported me, making sacrifices without hesitation, so as to enable me to reach this stage of my life.

My utmost thanks go to my wife Agnieszka, who has been with me throughout this life path. She has always supported me during the hard times typical of a doctorate, showing me that self-belief is essential to achieve any goal. I will forever owe her for what she has given me over these four years, Leonardo Jan included.

Thank you to my grandparents, who will read these words from somewhere.

Thank you to my cousin Duilio, and my uncles Italo, Lorenzo and Riccardo. I feel lucky to have grown up taking aspects of their personalities with me and applying them to my life.

Thank you to Aavishkar, Ahmed, Alessandro, Amrit, Bin, Giulio, Giuseppe and Marianna, Ji Li, Lewis, Majdi, Marco C. and Marco M. All of them have accompanied me through this path, providing escapism and mitigating my anxiety, to help me to succeed in achieving any goal.

I also need to acknowledge that this thesis was proofread for conventions of language, grammar and spelling by Janet's Proofreading Service.

"Whatever you do in your research of spray, it must be proven by fluid dynamics."

(Prof. Hongming Xu)

"Don't mind, keep going."

(Ji Li, Ph.D.)

"Ogni tua mancanza è un danno che arrechi al tuo prossimo."

(Prof. Ing. Arch. Francesco Mario Nanni)

"*La tua fantasia ha senso se sorretta dal rigore matematico. Non si sfugge!"*

(Prof. Ing. Arch. Francesco Mario Nanni)

"…e se non lo facciamo noi, chi se no?"

(Prof. Ing. Luciano Andrea Catalano)

"Sarete ingegneri. Ingegneri! Quindi ingegnatevi!"

(Prof. Ing. Antonio Ludovico)

"Quante volte ti si deve ripetere le cose?"

(Prof. Ing. Riccardo Amirante)

"….lo farai tu."

(Prof. Mauro Carnicella)

TABLE OF CONTENTS

ABSTRACT……1

PUBLICATION RECORD……4

ACKNOWLEDGEMENTS……....6

CHAPTER 1 - CURRENT IC MOBILITY AND FUTURE SCENARIOS……...…...28

Introduction……...28

1. The advent of electronically managed injection in IC engines ……..……..28

1.1. The gasoline direct injection……28

1.1.1. Brief historical background……...29

1.1.2. The GDI system……30

1.2. The introduction of common rail injection……...31

1.2.1. Brief historical background……...31

1.2.2. The CR injection system……...33

1.2.2.1. The Radialjet high-pressure pump……..33

1.2.2.2. The common rail……34

1.2.2.3. The CR injector……...35

1.2.2.3.1. The piezo-electric CR injector……37

1.2.2.3.1.1. The piezo-electric effect.……38

1.2.2.3.1.2. The working of the piezo-electric CR injector…..38

1.2.3. Successful racing applications of diesel-powered cars……39

1.2.4. Dieselgate.……39

1.3. Future fossil-fuels-related scenarios……..40

1.3.1. The advent of biofuels……...40

1.3.1.1. Categorisation of feedstocks for renewable fuels…….……..41

1.3.2. The wide spread of ethanol……...41

1.3.3. The furan-based blends…….42

1.3.4. Hydrogen as a solution for the growing mobility demand……42

1.4. The introduction of electric vehicles ……43

1.5. Objectives of the research activity…..……...44

1.5.1. Outline of the thesis…….45

1.5.1.1. Chapter 2 - The sensor for needle motion detection……...47

1.5.1.2. Chapter 3 - Experimental assessment of the hole-to-hole non-uniformity of diesel jets' velocities ……47

1.5.1.3. Chapter 4 - The hole-to-hole non-uniformity of the 2-MF-blend jets' velocities compared to diesel……..47

1.5.1.4. Chapter 5 - The injection-induced pressure fluctuations within the rail……48

1.5.1.5. Chapter 6 - Summary and future recommendations……...…….48

CHAPTER 2 - NOVEL SENSOR FOR DETECTION OF NEEDLE LIFT IN A COMMON RAIL INJECTOR……...…49

Introduction……...49

2.1. The key role of needle motion in the injection characterisation...……50

2.1.1. The influence of needle lift on the cavitation onset……..50

2.1.2. The impact of needle lift on the mass flow rate……51

2.2. The current devices for needle motion detection…….52

2.3. The optical fibre-based sensor……..54

2.3.1. The design of the optic fibre-based sensor……...54

2.3.2. The sensor's electric circuit……...57

2.3.3. Reasons motivating the optical fibre-based technique……..58

2.4. The experimental set-up……...58

2.5. The diesel injection tests……..61

2.6. The assessment of the time history of the needle motion……65

2.6.1. The assessment of needle lift……65

2.6.2. The assessment of the needle hold time……69

2.6.3. The assessment of the needle's downward motion ……..70

2.7. Summary……..72

CHAPTER 3 - EXPERIMENTAL INVESTIGATION OF THE HOLE-TO-HOLE NON-UNIFORMITY OF JET VELOCITIES IN A DIESEL INJECTOR……..……...…..…74

Introduction……...74

3.1. Literature review……...75

3.1.1. The impact of needle wobbles on the imbalance of injected fuel rate ……...75

3.2. The proposed approach……78

3.3. Experimental set-up……...79

3.3.1. High-pressure vessel (HPV)……79

3.3.2. The imaging set-up……..80

3.3.3 The image processing……..80

3.4. Methodology for the analysis of the hole-to-hole non-uniformity of diesel jets' velocities……...……82

3.5. Experimental tests……83

3.5.1. Tests conditions ……..83

3.5.2. Diesel properties……..84

3.5.3. The time development of the diesel plumes' length……85

3.5.3.1. Overlapping of PL curves at a backpressure of 20 bar……..87

3.5.3.2. Overlapping of PL curves at a backpressure of 40 bar……..87

3.5.3.3.Overlapping of PL curves at a backpressure of 60 bar……...88

3.5.3.3.1. The inconsistency referring to the 1400-60 bar case….88

3.5.3.4. Overlapping of PL curves at a backpressure of 80 bar……..……90

3.5.4. The injection delays of the diesel plumes……...…90

3.6. Discussion of the results……91

3.6.1. The assessment of the orifice-to-orifice variability in jet velocities……...91

3.6.1.1. Analysis of the standard deviations……...92

3.6.1.2. Analysis according to alternative statistical approach……...98

3.6.2. The assessment of averaged DOI……...99

3.6.2.1. The assessment of DOIs' standard deviation……...100

3.7. The physical principles governing the orifice-to-orifice variability……...101

3.7.1. Hypothesis about the impact of injection settings on needle wobbles …….102

3.7.2. The impact of injection settings on off-axis motions with respect to needle lift……...102

3.7.2.1. Needle lift correlated with eccentricity determining the unbalanced diesel flow……...103

3.7.2.2. The impact of injection settings on radial motion……..105

3.7.2.3. Discussion of the impact exerted by injection settings on radial motion according to the alternative statistical approach……...106

3.8. Summary……107

CHAPTER 4 - EXPERIMENTAL INVESTIGATION OF THE METHYLFURAN-DIESEL BLENDS' JET DEVELOPMENTS COMPARED TO DIESEL……...……..…..109

Introduction……109

4.1. Literature review and proposed study……110

4.1.1. State of the art of methylfuran-based fuel blends……110

4.1.1.1. The production technique of furan-based biofuels……...111

4.1.1.2. Literature review of MF-based fuels……112

4.1.2. The proposed study……..116

4.2. Experimental set-up……117

4.3. Methodology……...118

4.3.1. Methodology for analysis of hole-to-hole non-uniformity of jets' velocities.118

4.3.2. Calculation of fuel blend properties……119

4.3.2.1. Calculation of blend viscosity……...120

4.3.2.2. Estimation of blend density……...121

4.4. Experimental results……121

4.4.1. Temporal development of fuel jets' plumes……122

4.4.1.1. The assessment of the orifice-to-orifice variability in fuel plumes' velocity……..124

4.4.1.2. Assessment of hole-to-hole variability according to an alternative approach……128

4.4.2. The acquisition of injection delays……..131

4.5. Discussion of the results……..135

4.5.1. The impact of injection settings on needle motions……135

4.5.2. The impact of injector characteristics on needle motion……136

4.5.3. Influence of fuel properties on needle radial motion……...138

4.5.4. The impact of injection-induced pressure perturbation on needle radial motion……..139

4.5.5. The competition between shear stress and orthogonal stress on the needle…140

4.5.6. The assessment of injection delays……..141

4.5.6.1. The accentuation of internal frictions within fluid flow……...142

4.5.6.2. The impact of rail pressure fluctuations on DOIs……143

4.6. Summary……144

CHAPTER 5 - EXPERIMENTAL INVESTIGATION OF RAIL PRESSURE FLUCTUATIONS CORRELATED WITH INJECTION SETTINGS AND FUEL PROPERTIES……...……..147

Introduction……147

5.1. Injection-induced pressure fluctuations……148

5.1.1. Literature review of injection pressure fluctuations ……...148

5.1.2. The state of the art of MF-based blends.……154

5.1.3. The proposed study……..154

5.2. Test facilities……..155

5.3. Calculation of fuel blend properties.……..155

5.4. Experimental tests.……156

5.5. Analysis of the findings……..159

5.5.1. The assessment of rail pressure drops ……159

5.5.2. Analysis of rail pressure fluctuations.……165

5.5.2.1. Analysis of the retrieving time.……165

5.5.2.2. Analysis of amplitudes characterising rail pressure oscillations.……169

5.5.2.3. Analysis of time interval between injection pressure peaks.……170

5.5.3. The influence of backpressure on rail pressure fluctuations……...171

5.5.3.1. The influence of backpressure on rail pressure drop……171

5.5.3.2. The role of backpressure in rail pressure fluctuations..……174

5.5.3.3. The impact of backpressure on the amplitude of rail pressure fluctuations..175

5.5.3.4. The influence of backpressure on the time between rail pressure peaks…..176

5.6. The physical principles underlying the findings……177

5.6.1. Influence of the bulk modulus on wave propagation.……177

5.6.2. The impact of fluid elasticity on pressure oscillations……179

5.6.3. The impact of surface tension and fuel viscosity on pressure oscillations…..180

5.6.4. Peculiarities of MF-blends benefiting rail pressure fluctuations.……181

5.7. Summary…….……182

CHAPTER 6 - CONCLUSIONS AND FUTURE WORKS …….……..…..187

Introduction…….187

6.1. Summary of the thesis.……187

6.2. Summary of the findings…….188

6.2.1. The assessment of needle motion over the injection event……...188

6.2.2. The assessment of orifice-to-orifice variability of diesel jets' velocities……..189

6.2.3. The hole-to-hole variability of diesel jets' velocities compared to MF-based blends…….190

6.2.4. The investigation of injection-induced pressure fluctuations within the rail…190

6.3. Recommendations for future research activities……191

6.3.1. Technique for increasing injection pressure.……..**.....**191

6.3.1.1. Layout of the proposed method.……..192

6.3.1.2. Working principle of the proposed method.……....193

6.3.1.3. Possible drawbacks related to the induced increase in injection pressure...193

6.3.1.4. Further development of this research activity……..194

6.3.2. CFD for the assessment of the combined action of viscosity with density on needle wobbles……..194

6.3.3. The needle's off-axis sensor……..195

6.3.3.1. Main criticalities related to the detection of needle wobbles……...195

6.3.3.2. Possible techniques for the detection of needle wobbles…….196

6.3.3.2.1. Electromagnetic fields-based solution……...196

6.3.3.2.2. The optical technique……196

REFERENCES……198

LIST OF FIGURES

CHAPTER 1

Figure 1.1. The Mercedes "Gullwing" 300 SL, the first mass-production car provided with direct fuel injection (1954)……29
Figure 1.2. F1 cars provided with direct injection (from left to right): Mercedes W196 (1954-1955); Maserati 250F (1954-1960); Ferrari 158 (1964)……30
Figure 1.3. Sectional view of the traditional configuration of the modern GDI system…..….30
Figure 1.4. Alfa Romeo 156 JTD was the first car powered by an engine provided with CR injection……..32
Figure 1.5. The typical configuration of a CR injection system……...33
Figure 1.6. The sectional view of a CR high-pressure pump: 1 – pump shaft; 2 – eccentric cam; 3 – pumping piston; 4 – inlet valve; 5 – delivery ball valve; 6 – fuel inlet...34
Figure 1.7. The common rail…….35
Figure 1.8. The sectional view of a typical solenoid-driven CR injector…….36
Figure 1.9. A typical piezoelectric CR injector……38
Figure 1.10. The first CR-powered prototypes winning the 24 Hours of Le Mans: Audi R10 TDI and Peugeot 908 HDi FAP…….39
Figure 1.11. Schematisation of the injection event and topics investigated here.……...45
Figure 1.12. The schematised development of the thesis' work……...46

CHAPTER 2

Figure 2.1. The electromagnetic fields, arisen from the current signal, are captured by the eddy currents transducer as noise, affecting negatively the detection of the control piston displacement……52
Figure 2.2. The frusto-conical surface, machined on the control piston for the installation of the eddy current sensor, gives rise to greater mechanical weakness……..53
Figure 2.3. Schematic layout of the sensor: 1- Emitter, 2 - Receiver, 3 - Grooved cylinder placed within the detector, 4 - Optical fibre, 5 - Injector body, 6 - Electric circuit box……..54
Figure 2.4. Mutual position between the circles; indicative of the optical cable's end and the receiver, determining the intersection area, meaningful of the control piston's position…….55
Figure 2.5. The geometry of the holes on the injector body (a), (b) and on the control piston. The mutual position of the through holes at stand-by configuration of injector (b).....55
Figure 2.6. The slotted hole on the injector body…….56
Figure 2.7. The electric circuit feeding the optical sensor……57
Figure 2.8. Schematic diagram of the sensor's circuit……..57
Figure 2.9. The CR test bench, a STPiW2 type manufactured by Autoelektronika……...…..59
Figure 2.10. Test rig: 1 – Electric Motor; 2 - Transmission belt; 3 – Tank; 4 – Filter; 5 – Low-pressure pump; 6 – High-pressure Pump; 7 – Backflow fuel by the high-pressure

pump to heat exchanger; 8 – Highly pressurised fuel line; 9 – Common rail; 10 – Pressure regulating valve; 11 – Injector; 12 – Backflow fuel line; 13 – Heat exchanger; 14 – Return cooled fuel line; 15 – Emitter; 16 – Optical fibre; 17 – Receiver; 18 – High-pressure vessel; 19 – Pressure gauges; 20 – Pressurised air chamber; 21 – Pressurised air tank; 22 – Relief valve; 23 – Oscilloscope; 24 – Computer; 25 – Voltage supplier…….59
Figure 2.11. The fuel pressure sensor mounted onto the common rail……60
Figure 2.12. Front and side views of layout of the highly pressurised system: 1 – CR injector; 2 – Pressure gauge; 3 – High-pressure vessel; 4 – Relief valve; 5 – Pressurised air chamber……..60
Figure 2.13. Overall layout of the experimental set-up including the highly pressurised chamber, oscilloscope, frame supporting the circuit box and voltage supplier feeding the circuit……61
Figure 2.14. Needle motion detected at an injection pressure of 400 bar and various backpressures……...62
Figure 2.15. Needle motion detected at an injection pressure of 700 bar and various backpressures……...62
Figure 2.16. Needle motion detected at an injection pressure of 1000 bar and various backpressures……...62
Figure 2.17. Needle motion detected at an injection pressure of 1400 bar and various backpressures……...63
Figure 2.18. Needle motion referring to the pilot performed at 1400 bar and 60 bar. The energising time was set at 300 μs……64
Figure 2.19. Needle motion referring to the pilot performed at 1400 bar and 80 bar. The energising time was set at 150 μs……64
Figure 2.20. Needle motion referring to the pilot performed at 400 bar and 20 bar. The energising time was set at 650 μs……65
Figure 2.21. The variation in rise time of needle motion at various injection pressures and backpressures……...66
Figure 2.22. Pressurised fuel momentum can be discriminated into two components…….....67
Figure 2.23. The hold time varies with injection pressure and backpressure……...69
Figure 2.24. The injector's closing stage is a function of the injection pressure and backpressure……70

CHAPTER 3

Figure 3.1. The flow rate q_E through the eccentric annular gap differs from the flow rate q_C when the gap is concentric……76
Figure 3.2. Test rig: 1 - Electric engine; 2 - Transmission belt; 3 - Fuel filter; 4 - Low-pressure pump; 5 - High-pressure pump; 6 - High-pressure line; 7 - Rail; 8 - Pressure regulating valve; 9 - Injector; 10 - Backflow fuel line; 11 - Heat exchanger; 12 - High-speed camera; 13 - High-pressure vessel; 14 - Pressurised nitrogen chamber; 15 - Manometers; 16 - Pressure regulator valves; 17 - Pressurised nitrogen bottle;

18 - Relief valve; 19 - Computer; 20 - Halogen bulb; 21 - Mirror; 22 - Fuel tank……..…79
Figure 3.3. The fuel plumes' image processing via an in-house developed MATLAB script and time-stamps (p_{INJ} = 1400 bar, BP = 20 bar)……81
Figure 3.4. The fuel plumes' image processing via an in-house developed MATLAB script (ASOI = 480 μs, p_{INJ} = 1400 bar, BP = 20 bar)……81
Figure 3.5. The temporal PL developments related to each of seven holes and averaged over five injection shots, acquired at various injection pressures and backpressure of 20 bar (a), 40 bar (b), 60 bar (c) and 80 bar (d)……..86
Figure 3.6. The time-histories of PL exiting the holes. The charts refer to three single main injections before the statistical analysis……88
Figure 3.7. The PL time-histories referring to single injections performed at p_{INJ} = 1400 bar and BP = 60 bar, and not included in the statistical analysis……89
Figure 3.8. The surface plotting the standard deviation of the jets' velocities calculated at the orifice outlet during the early stages of injection……...93
Figure 3.9. The standard deviation of the jets' velocities measured at the outlet of the orifices……94
Figure 3.10. Surface plotting standard deviations of velocities at 200 μs after injection start and shown at reverse axis arrangements……..95
Figure 3.11. The time histories of standard deviations at various injection settings……96
Figure 3.12. Trend of averaged reduction in standard deviation referring to injections performed at constant ambient pressure and different injection pressures…..…97
Figure 3.13. The trend of the average of the standard deviations of jets' velocities if calculated via the alternative approach……98
Figure 3.14. The components compounding the force acting on the needle determine the axial and radial motions……..103
Figure 3.15. Sketch simplifying the typical VCO injector nozzle. The light blue needle refers to the highest position, whilst the grey one stands for the stand-by configuration……..104

CHAPTER 4

Figure 4.1. Schematisation of the process converting carbohydrates to MF……..111
Figure 4.2. The sequence of MF30 plumes' images' processing, via the in-house developed MATLAB code and related time-stamps……117
Figure 4.3. The sequence of the MF50 plumes' images' processing, via the in-house developed MATLAB code and related time-stamps……118
Figure 4.4. Time history of the averaged lengths of MF30 plumes……122
Figure 4.5. Time history of the averaged lengths of MF50 plumes……....123
Figure 4.6. The standard deviations of MF30 a), and MF50 b), fuel plumes' velocities as a function of injection pressure and backpressure……..125
Figure 4.7. The standard deviations of the averaged plumes' velocities measured at early stages (≈ 40 μs) of the injection event……..126
Figure 4.8. The standard deviations of plumes' velocities calculated according to the alternative statistical approach……129

Figure 4.9. Averaged DOIs referring to diesel, MF30 and MF50 at various injection settings……..134
Figure 4.10. Lower viscosity implies weaker shear stress on the needle. As a consequence, needle oscillations are alleviated, minimising the imbalance of fuel flow through the orifices……138

CHAPTER 5

Figure 5.1. The CR injector is mounted perpendicularly onto the flanged top of the high-pressure vessel……..155
Figure 5.2. The time-history of rail pressure at various injection pressures and a backpressure of 20 bar……...157
Figure 5.3. The time-history of rail pressure at various injection pressures and a backpressure of 40 bar……...157
Figure 5.4. The time-history of rail pressure at various injection pressures and a backpressure of 60 bar……...158
Figure 5.5. The time-history of rail pressure at various injection pressures and a backpressure of 80 bar……...158
Figure 5.6. The averaged reductions in rail pressure, arising after the injection start, at each of 16 injection settings……....164
Figure 5.7. Lower viscosity (a) results in a less thick boundary layer. This minimises the impact of the friction losses at the nozzle walls, boosting fuel flow velocity. By contrast, greater viscosity slows down fuel flow (b), because of accentuated friction at the orifice walls (c)……..165
Figure 5.8. The averages of time required by rail pressure to recover the value preceding the previous injection shot……169
Figure 5.9. The averaged amplitudes of rail pressure fluctuations at various injection pressures and backpressures……170
Figure 5.10. Time interval between two consecutive pressure peaks, at various injection pressures and backpressures……171
Figure 5.11. Increasing bulk modulus boosts the speed of the pressure wave, mitigating the effect on the surrounding fluid region, where a less accentuated gradient pressure arises…..……179

CHAPTER 6

Figure 6.1. The sketch of the proposed technique to induce greater injection pressures, so as to recover the pressure gaps originated from the dynamic effects within the rail: 1 – rail; 2 – CR injector; 3 – ECU; 4 – fuel pressure sensor; 5 – fuel acceleration duct; 6 – electronically managed shutdown valve; 7 – strain gauge; 8 – computer……192
Figure 6.2. The sketched layout of the optical solution: 1 – emitter; 2 – receiver; 3 – needle; 4 – nozzle; 5 – slot machined on the needle……197

LIST OF TABLES

CHAPTER 2

Table 2.1. The rise time of the needle at various injection and backpressures……66
Table 2.2. The impact of the dragging action of the control piston on the optical fibre at various injection settings……..……68
Table 2.3. The duration of the needle maximum position at various injection and backpressures……69
Table 2.4. The duration of the injector's closing stage at various injection and backpressures……70

CHAPTER 3

Table 3.1. Injection pressures and backpressures determining the tests conditions……83
Table 3.2. Injection settings set by authors of papers pertaining to the assessment of needle radial motion……..84
Table 3.3. The highest in-cylinder pressure detected in a diesel engine at various rotational speeds……84
Table 3.4. Properties of the employed diesel……85
Table 3.5. DOI (in μs) detected at various injection pressures and a backpressure of 20 bar..90
Table 3.6. DOI (in μs) detected at various injection pressures and a backpressure of 40 bar..91
Table 3.7. DOI (in μs) detected at various injection pressures and a backpressure of 60 bar..91
Table 3.8. DOI (in μs) detected at various injection pressures and a backpressure of 80 bar..91
Table 3.9. Standard deviation of fuel plumes' velocities (in m/s)……92
Table 3.10. Standard deviation of diesel plumes' velocities (in m/s) at 200 μs ASOI…….95
Table 3.11. Reductions in σ (in m/s) stemming from switching injection pressure to higher values at constant backpressure……96
Table 3.12. The standard deviations of diesel plumes' velocities (in m/s) if calculated via the alternative statistical approach……...98
Table 3.13. The variations in σ (in m/s) due to switching injection pressure to higher values……..99
Table 3.14. Averages calculated from the DOI averages (in μs)……..99
Table 3.15. Averaged standard deviations of DOI (in μs)……..100

CHAPTER 4

Table 4.1. Properties of fuels compounding the blends tested here……119
Table 4.2. The ranges of MF30 and MF50 viscosities obtained according to the commonly employed methodologies……121
Table 4.3. Standard deviations of the averaged plumes' velocities detected at 40 μs of ASOI time (MF30)……124
Table 4.4. Standard deviations of the averaged plumes' velocities detected at 40 μs of ASOI time (MF50)……124
Table 4.5. Reductions in σ stemming from switching injection pressure to higher values at a constant backpressure (MF30)……127

Table 4.6. Reductions in σ stemming from switching injection pressure to higher values at a constant backpressure (MF50)……127
Table 4.7. Averaged standard deviations of plumes' velocities at 40 μs of ASOI over five consecutive MF30 shots……...128
Table 4.8. Averaged standard deviations of plumes' velocities at 40 μs of ASOI over five consecutive MF50 shots……...129
Table 4.9. Reductions in σ stemming from switching injection pressure to higher values at a constant backpressure (MF30)……130
Table 4.10. Reductions in σ stemming from switching injection pressure to higher values at a constant backpressure (MF50)……131
Table 4.11. Delays of MF30 injections in μs detected at various injection pressures and a backpressure of 20 bar……131
Table 4.12. Delays of MF30 injections in μs detected at various injection pressures and a backpressure of 40 bar……131
Table 4.13. Delays of MF30 injections in μs detected at various injection pressures and a backpressure of 60 bar……132
Table 4.14. Delays of MF30 injections in μs detected at various injection pressures and a backpressure of 80 bar……132
Table 4.15. Delays of MF50 injections in μs detected at various injection pressures and a backpressure of 20 bar……132
Table 4.16. Delays of MF50 injections in μs detected at various injection pressures and a backpressure of 40 bar……132
Table 4.17. Delays of MF50 injections in μs detected at various injection pressures and a backpressure of 60 bar……132
Table 4.18. Delays of MF50 injections in μs detected at various injection pressures and a backpressure of 80 bar……133
Table 4.19. Delays of MF30 injections averaged over five injections……...133
Table 4.20. Delays of MF50 injections averaged over five injections……..…..133
Table 4.21. Fuel properties of fuel tested in this study and Zhang's research activity (T = 25° C)……..141

CHAPTER 5

Table 5.1. The properties of the fuels constituting the blends……156
Table 5.2. Diesel pressure drops (in bar) arising after the start of injection……...…161
Table 5.3. MF30 rail pressure drops (in bar) arising after the start of injection……...……..162
Table 5.4. MF50 rail pressure drops (in bar) arising after the start of injection……...……..163
Table 5.5. Time required (in ms) by diesel rail pressure to return to set rail pressure……...166
Table 5.6. Time required (in ms) by MF30 rail pressure to return to set rail pressure……...167
Table 5.7. Time required (in ms) by MF50 rail pressure to return to set rail pressure……...168
Table 5.8. Rail pressure drops (in bar) induced by diesel injection at various injection scenarios……...172
Table 5.9. Rail pressure drops (in bar) induced by MF30 injection at various injection scenarios……..……172

Table 5.10. Rail pressure drops (in bar) induced by MF50 injection at various injection scenarios……...172
Table 5.11. Time intervals (in ms) required by rail pressure to retrieve the value preceding the diesel injection…….174
Table 5.12. Time intervals (in ms) required by rail pressure to retrieve the value preceding the MF30 injection…….174
Table 5.13. Time intervals (in ms) required by rail pressure to retrieve the value preceding the MF50 injection…….174
Table 5.14. Amplitudes of rail pressure fluctuations (in bar) arisen as a result of diesel injection……175
Table 5.15. Amplitudes of rail pressure fluctuations (in bar) arisen as a result of MF30 injection……175
Table 5.16. Amplitudes of rail pressure fluctuations (in bar) arisen as a result of MF50 injection……176
Table 5.17. Duration of the time interval (in ms) between two consecutive pressure peaks (diesel injection)……...176
Table 5.18. Duration of the time interval (in ms) between two consecutive pressure peaks (MF30 injection)……..176
Table 5.19. Duration of the time interval (in ms) between two consecutive pressure peaks (MF50 injection)……..177
Table 5.20. Diesel's surface tension as a function of temperature…….180

LIST OF EQUATIONS

CHAPTER 1

Equation 1.1……..36
Equation 1.2……..37

CHAPTER 2

Equation 2.1……..67
Equation 2.2……..71

CHAPTER 3

Equation 3.1……..75
Equation 3.2. ……82
Equation 3.3. ……82
Equation 3.4. ……85
Equation 3.5. ……..101
Equation 3.6. ……..104

CHAPTER 4

Equation 4.1. ……..120
Equation 4.2. ……..120
Equation 4.3. ……..120
Equation 4.4. ……..121
Equation 4.5. ……..121
Equation 4.6. ……..121
Equation 4.7. ……..121
Equation 4.8. ……..137
Equation 4.9. ……..138

CHAPTER 5

Equation 5.1. ……..156
Equation 5.2. ……..164
Equation 5.3. ……..178
Equation 5.4. ……..180
Equation 5.5. ……..181

LIST OF ABBREVIATIONS

ACO	Automobile Club de l'Ouest
ASOI	after start of injection
CAD	crank angle degrees
CFD	computational fluid dynamics
CI	compression ignition
CO	carbon monoxide
CR	common rail
DOI	delay of injection
DME	di-methyl ether
ECU	electronic control unit
EPA	Environmental Protection Agency
EPSRC	Engineering and Physical Sciences Research Council
FAEE	fatty acid ethyl ester
FAME	fatty acid methyl ester
FF	fossil fuel
GDI	gasoline direct injection
HC	hydrocarbon
HPV	high-pressure vessel
IC	internal combustion
ICE	internal combustion engine
IMEP	indicated mean effective pressure
LMP	Le Mans prototype
MF	methyl furan
NSFC	National Natural Science Foundation of China
PDI	petrol direct injection
PID	proportional–integral–derivative
PL	plume length
PM	particulate matter
RME	rapeseed methyl ester
RPM	revolutions per minute
SI	spark ignition
TD	turbodiesel
TDI	turbocharged direct injection
UHC	unburnt hydrocarbons
VCO	valve-covered orifice

NOMENCLATURE

A	abfluss
A_i	coefficient
A_{CPT}	area of the control piston top
A_{NP}	area of the needle protrusion
A/F	air-fuel ratio
a_N	acceleration of the needle
BP	backpressure
BP*	contribution of backpressure on the needle protrusion
c	speed of sound
D	hole diameter
d	clearance of the annular gap
d_i	parameter describing the flow section variation
e	eccentric distance between the needle centre and the injector axis
F_{CPT}	force acting on the control piston top
F_E	elastic force acting to the injector's closing direction
F_{NP}	force acting on the needle protrusion
F_V	opposing force arisen within the fluid in response to a perturbation
h	axial displacement covered by the needle
K	bulk modulus
L	unit of length of the fluid particle
M	momentum of pressurised fuel
m_N	mass of the needle
m_{CP}	mass of the control piston
N	number of injector holes
p_{INJ}	injection pressure
p*	varying pressure within the control chamber
Δp	fluid reaction contrasting the deformation caused by wave perturbation
q_C	volumetric flow when the gap between the needle and internal nozzle walls is concentric
q_E	volumetric flow rate of a quasi-steady viscous through an eccentric annular gap
R	fluid particle radius
S	needle cylindrical surface in contact with fuel flow
T	fuel temperature
t	time
U	fuel velocity
u_i	velocity of a single plume
$\bar{u}$	velocity averaged over the seven fuel plumes
V	relative velocity between liquid and surrounding gas
ΔV	relative velocity between the needle and fuel flow
y	coordinate orthogonal to needle surface

Greek symbols

υ	fuel kinematic viscosity
μ	fuel dynamic viscosity
ρ	fuel density
χ	weight fraction
ε	ratio of d with e
δ	thickness of boundary layer
τ	shear stress
σ	standard deviation of jets' velocities
Θ	fuel surface tension

CHAPTER 1

CURRENT IC MOBILITY AND FUTURE SCENARIOS

Introduction

Over the last few decades, the increasingly severe emission regulations and the depletion of fossil energy have determined radical changes within the global automotive scenario. This framework has urged the main carmakers to include the minimisation of the carbon footprint among the requirements of modern IC engines. Several research efforts have been thereby directed to explore novel solutions regarding innovative engine designs, as well as the development of alternative fuels, until the world-scale spread of electric vehicles becomes a viable pathway for green mobility.

1. The advent of electronically managed injection in IC engines

The need for combining the optimisation of performance with the progressively severe environmental mandates has led to the development of groundbreaking technologies, such as electronically managed injection. In this respect, gasoline direct injection (GDI) and the common rail (CR) system have been designed for engines fuelled with gasoline and diesel, respectively. The launch of these cutting-edge techniques has represented a milestone for the improvement of combustion quality, engine's thermal efficiency and power output.

1.1. The gasoline direct injection

Concerning the gasoline-fuelled engine, a key step towards the optimisation of its performance has been given by the introduction of the direct injection system. The first applications of direct injection were characterised by mechanisms actuating the injectors. The

need for a faster injector response has then urged engine manufacturers towards the development of electronic systems to manage the injection process.

1.1.1. Brief historical background

The development of this technique is rooted in World War II. In the light of experience gained via aircraft-purposed applications, the Mercedes-Benz research team designed the first automotive-purposed engine provided with a direct injection system. This technology, manufactured by Bosch Gmbh, was applied for the first time on a mass-production car, the so-called Mercedes "*Gullwing*" 300 SL.



Figure 1.1. The Mercedes "*Gullwing*" 300 SL, the first mass-production car provided with direct fuel injection (1954) **(1)**

A mechanical direct fuel injection system was installed on the M198-type engine, replacing the traditional triple two-barrel carburettors mounted on the Mercedes W194 model. Thereafter, direct injection was mounted on engines powering cars belonging to a small market segment, such as some models manufactured by Maserati, Ferrari and Aston Martin. In the light of the outstanding engine performance provided with the direct injection system, this technology has been extended to race applications, bringing to the fore specialized manufacturers such as Bosch, Lucas and SPICA. **(2, 3)**



Figure 1.2. F1 cars provided with direct injection (*from left to right*): Mercedes W196 (1954-1955) **(4)**; Maserati 250F (1954-1960) **(5)**; Ferrari 158 (1964) **(6)**

Therefore, prior to the launch of the electronically managed GDI, unveiled by Mitsubishi in 1996, this technology was not deployed for large-scale car production. The following years saw outstanding improvement of engine performances attributable to the electronically controlled GDI. This caused carburettors and the mechanically actuated injection system to be gradually superseded by GDI technology.

1.1.2. The GDI system

Also known as petrol direct injection (PDI), gasoline direct injection differs from manifold systems, where fuel is injected into the intake manifold. In fact, the high-pressure fuel is injected into the combustion chamber (Figure 1.3).



Figure 1.3. Sectional view of the traditional configuration of the modern GDI system **(7)**

In order to prevent excessive wear on the injectors, injection pressure is commonly limited to approximately 200 bar. This limit of the injection pressure is owed also to the lower lubrication provided by gasoline in comparison with diesel.

However, the GDI system has presented drawbacks such as:

- greater system complexity, given the high injection pressures to boost atomisation;
- higher production costs;
- possible failures due to the carbonaceous deposits arising in the orifices **(8-13)**;
- worse lubrication of the components, owing to the low fuel viscosity;
- difficulty in injector positioning, given the spark plug;
- fuel impingement on the cylinder walls, especially in cold starting conditions, to the detriment of fuel evaporation.

1.2. The introduction of common rail injection

With regard to diesel engines, a decisive contribution towards the improvement of their efficiency has been determined by the advent of the common rail (CR) system.

1.2.1. Brief historical background

A forerunner of the CR system was direct injection unveiled by Fiat Croma TD in 1986. Invented by the Italian physicist Mario Ricco, the CR system has been developed by the fruitful joint efforts of Bari-based Centro Ricerche FIAT with Magneti Marelli and Elasis. Afterwards, the project was sold to Bosch Gmbh, who managed the following stages of the industrialisation process. The large-scale production of CR-powered engines began in 1997 with the launch of the Alfa Romeo 156 1.9 and 2.4 JTD (UniJet Turbo Diesel).



Figure 1.4. Alfa Romeo 156 JTD was the first car powered by an engine provided with CR injection **(14)**

The injection is characterized by a pre-injection, aimed to raise the temperature within the combustion chamber, followed by a main injection. This methodology has been found to smoothen the combustion process, minimising the noise typical of traditional diesel engines and reducing unburnt gas emissions and fuel consumption, combined with better vehicle manoeuvrability. The CR evolutions, developed by Bosch and other manufacturers (Siemens, Denso, Delphi), have increased the competitiveness of diesel engines, upgrading them to become a valid alternative to gasoline engines for passenger applications. Following on from the period when it was an exclusive only of main Italian carmakers (Fiat, Lancia and Alfa Romeo), the CR system has been deployed also by the main automotive groups. The second CR version was unveiled in 2008, with the so-called Multijet, characterised by an injection cycle split up into five shots, traditionally named as pilot, pre, main, after and post. The introduction of post-injections has been required by the implementation of the anti-pollution strategies. As such, the MultiJet is based on split injections, the timing and duration of which are set by the electrical control unit (ECU), according to the signals output by the sensors. It has been discovered that MultiJet can further optimise diesel engines' performance. The third generation of CR was debuted in 2013, with the JTDm2 engine powering the Alfa Romeo MiTo and Giulietta. Nowadays, a significant market share has been gained by the piezo-injectors, which assure faster injections, given the working principle differing from the

solenoid-actuated injector. This additional innovation enables the injector to perform up to eight injections per cycle.

1.2.2. The CR injection system

The CR technology differs from precedent diesel systems, since pressure formation is independent from the injection timing management, assuring great operating flexibility. **(15)** The CR system is basically compounded with (Figure 1.5):

- a high-pressure pump (1);
- a rail (2);
- electronically controlled injectors (3);
- the ECU (4).

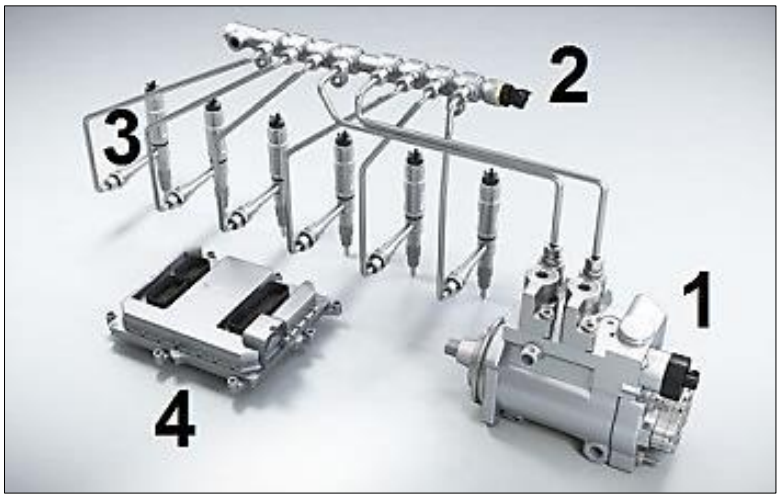


Figure 1.5. The typical configuration of a CR injection system **(16)**

1.2.2.1. The *Radialjet* high-pressure pump

In the CR injection system, fuel is delivered by the low-pressure pump to the high-pressure pump, commonly referred to as *Radialjet*, given three pumping pistons radially arranged with respect to the rotation axis of the pump shaft (Figure 1.6).

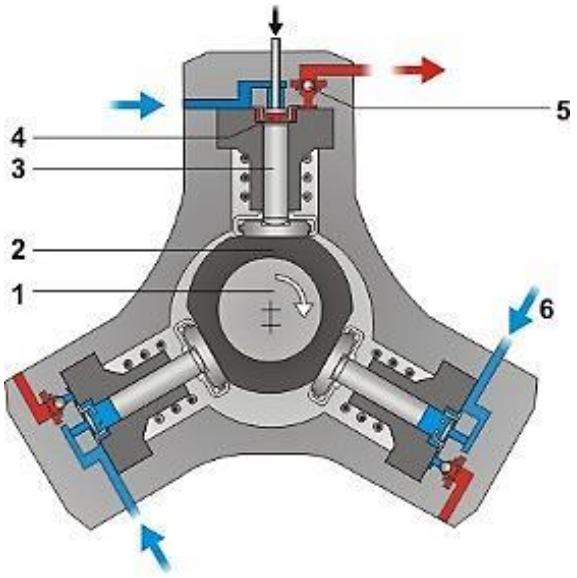


Figure 1.6. The sectional view of a CR high-pressure pump: 1 – pump shaft; 2 – eccentric cam; 3 – pumping piston; 4 – inlet valve; 5 – delivery ball valve; 6 – fuel inlet **(17)**

The angular distance between two pumping pistons is equal to 120°. The pump is driven by the engine by means of a transmission belt; whilst the piston axial displacement is determined by the rotation of an eccentric cam. A mechanical interface, placed between the eccentric cam and an end of the pumping piston, drives the movement of the three pistons. The contact between the eccentric cam and the tappet at the end of the pumping piston is secured by means of a spring. The rotation speed of the pump shaft is approximately half of that of the engine. Each pumping element is equipped with a suction plate valve and a delivery ball valve. The outputs of each pumping element are placed within the pump and they deliver the pressurised fuel to a common manifold.

1.2.2.2. The common rail

The rail is a cylinder-shaped accumulator for storing high-pressurised diesel (Figure 1.7).

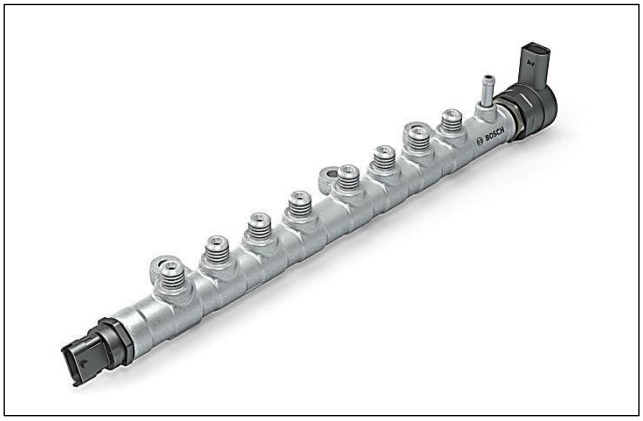


Figure 1.7. The common rail **(18)**

It is made of steel, so as to withstand the high pressures acting therein, and has threaded holes enabling the mounting of pipes connecting the injectors' inlet. Two threaded holes are drilled at the ends of the rail. One threaded hole enables the mounting of a fuel pressure sensor, whilst the other one is commonly devoted to the installation of a thermocouple. The internal volume of the rail (40 cm^3 for a 4-cylinder engine and 2 litres of displacement) is suitably designed to shorten the injection-induced pressure adjustment and the filling during the start-up stage, in which the rail must be filled as rapidly as possible. **(15)** Accordingly, a smaller volume would accentuate the impact of fuel pressure pulsations on the quality of the following shot; whilst a larger volume would prolong the filling process during the engine starting.

1.2.2.3. The CR injector

The high-pressure pump supplies pressurized fuel to the rail, which serves as high-pressure storage. Afterwards, the fuel reaches the injectors, the opening and closing stages of these are managed by the ECU according to the signals output by the sensors. More specifically, within the injector, pressurized fuel fills the control chamber through the *Z-hole* and the delivery chamber, located above and below the control piston-needle assembly, respectively (Figure 1.8).

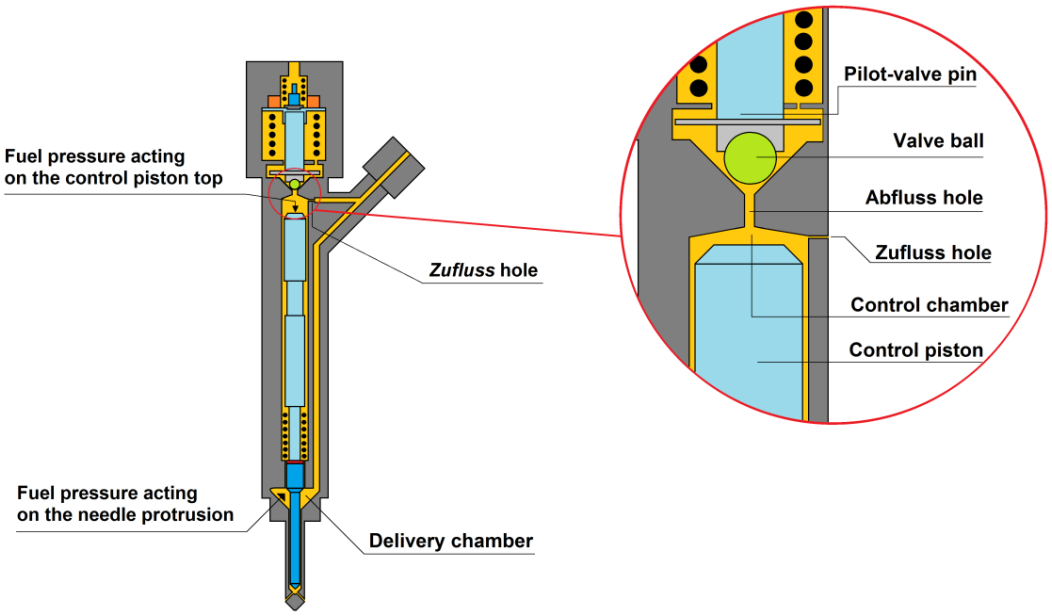


Figure 1.8. The sectional view of a typical solenoid-driven CR injector

This gives rise to two opposing forces. The needle is closed also thanks to a small spring. More specifically, three forces govern the motion of the control piston-needle assembly, namely:

- the elastic force F_E, contributing to the closing direction and determined by the spring on the control piston; this force assures the tightness of the nozzle, preventing fuel from dripping into the cylinder when the injector is in a stand-by configuration.
- The force F_{CPT}, acting on the top of the control piston.
- The force F_{NP}, acting on the needle protrusion.

The motion of the control piston-needle assembly is governed by the balance of these forces. When the injector solenoid is not energised, the closing forces outweigh the opening forces. Therefore, it results that:

$$F_{CPT} + F_E > F_{NP} \tag{1.1}$$

The control piston-needle assembly is thereby kept in the closed position.

Once the ECU delivers the electric pulse energising the solenoid, the ball valve is dragged up by the pilot-valve pin, opening the *A-hole*. The fuel flows through the *A-hole*, emptying the control chamber. The ensuing imbalance between forces can be schematized as follows:

$$F_{CPT} + F_E < F_{NP} \quad (1.2)$$

The pressurized fuel acting in the delivery chamber drives up the control piston-needle assembly, causing the injector to open and hence, fuel is injected into the combustion chamber.

Along with axial displacement, the needle is subjected to off-axis motion, given the circular gap between the needle and the internal walls of the nozzle. The impact of any wobbles on the internal fuel flow is significantly determined by the magnitude of the force acting on the needle protrusion. Moreover, the effect of needle wobbles on the fuel flow is greater at the needle tip, where the cantilever effect is more accentuated in comparison with the upper part. Therefore, this phenomenon is more observable at lower lifts.

Once the solenoid is deactivated, the pilot-valve pin moves downward and drives the ball valve onto the *A-hole*. The control chamber is filled with fuel flowing through the *Z-hole*, giving rise to an increase in pressure therein. The downward motion of the assembly ensues, causing the injector's closure.

1.2.2.3.1. The piezoelectric CR injector

Despite the advantages of the CR system favouring the minimisation of the environmental impact, increasingly greater emphasis on the concerns regarding diesel emissions have led to additional refinements of this technology. In this framework, alongside increasing rail pressure, other solutions have been designed, such as piezoelectric injectors. The advent of this technique has contributed to further improvement of the modern CR injection systems, thanks to precise injections' timing and metering.

1.2.2.3.1.1. The piezoelectric effect

The piezoelectric effect was discovered by Pierre and Jacques Curie in 1880, and is based on the capability of certain crystals to generate an electrical discharge in response to a mechanical stress. A polarization is generated, due to the arising positive and negative ions in the crystal, between the ends of which an electrical field takes place. Similarly, a sort of "*inverse piezoelectric effect*" is feasible when a voltage is applied to the ends of the crystal. As a consequence, the crystal is subjected to a voltage-induced dilation or a contraction.

1.2.2.3.1.2. The working of the piezoelectric CR injector

In the light of the ability to expand rapidly when involved with an electrical charge, piezoelectric crystals have been placed within the CR injector (Figure 1.9).

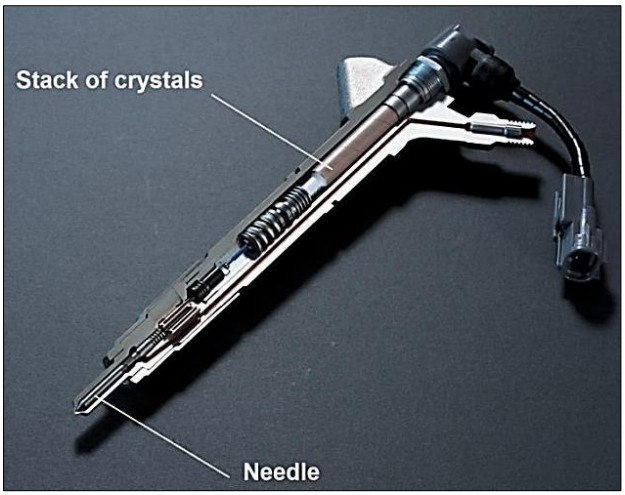


Figure 1.9. A typical piezoelectric CR injector **(19)**

More specifically, hundreds of piezo wafer-shaped crystals are stacked within the injector. Once the voltage is applied on the crystals, their structure experiences a slight dilation over less than thousandths of a second. In this regard, the extremely low dilation of the piezo element has raised issues about the magnitude of force sufficing to drive the needle. This drawback was circumvented by the injector manufacturers, setting a stack of no fewer than 400 crystals, on which a voltage impulse of a hundred volts is applied. This solution assures

an acceptable degree of stack linear movement, which is transmitted to the needle, determining the start of the injection. Therefore, piezo crystals serve as actuators operating in a frictionless motion. This peculiarity enables the CR injectors to act up to five times faster than a traditional injector, thereby resulting in multiple injections per combustion cycle.

1.2.3. Successful racing applications of diesel-powered cars

In 2003 the Automobile Club de l'Ouest (ACO) granted authorisation to diesel-powered prototypes to participate in the prestigious 24 Hours of Le Mans. This decision has laid the groundwork for the positive return of the diesel image, determining a steep increase in the sales volume of diesel-powered cars. In the wake of this unprecedented permission within motorsport, carmakers started the rush to develop the LMP (*Le Mans Prototypes*) cars. Peugeot developed the 908 HDi FAP; whilst Audi designed the R10 TDI, the first diesel-powered prototype winning the 24 Hours of Le Mans.

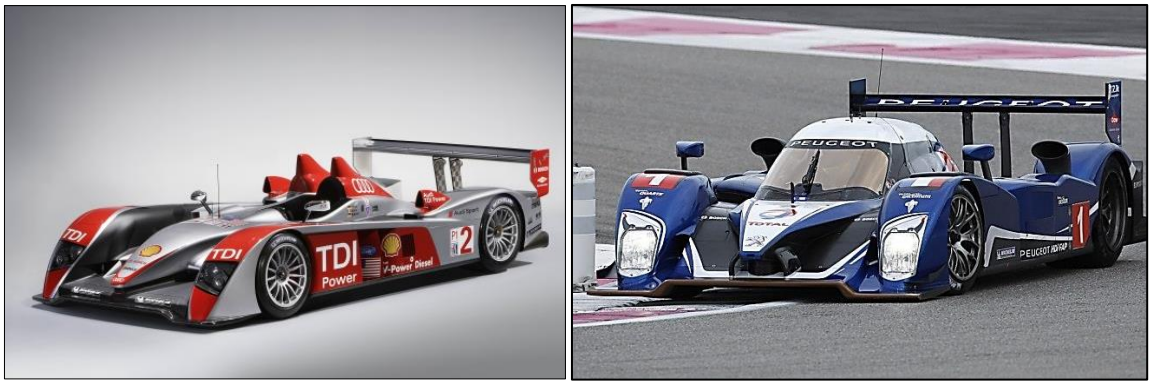


Figure 1.10. The first CR-powered prototypes winning the 24 Hours of Le Mans: Audi R10 TDI **(20)** and Peugeot 908 HDi FAP **(21)**

These successes have marked the predominant epoch of diesel prototypes over the gasoline-powered engines.

1.2.4. Dieselgate

If on one hand these successes in race competitions shed light on the promising margins of improvement of the CR system, on the other hand the emissions' scandal, commonly referred

to as Dieselgate and involving the Volkswagen group in 2015, has raised public awareness of the pollution levels emitted by diesel engines. From an investigation from the Environmental Protection Agency (EPA), it indeed emerged that the Volkswagen diesel engines emitted pollutant levels largely violating the US limitations. The EPA evidenced the key role of some software activating the controls only during lab testing. Whilst, once the engine ran in realistic scenarios, the NO_X levels were found to exceed up to 40 times the legal limits. Hence, the Volkswagen group had to set up an unprecedented worldwide recall of vehicles.

1.3. Future fossil-fuels-related scenarios

The decades following the end of WWII have seen the full expansion of mass motorisation. The consequential increase in demand for fossil fuels has then contributed to the fast depletion of fossil energy sources. This scenario has led the automotive industry to search for alternative solutions, enabling the global mobility to break away from fossil fuels. A solution might be given by the renewable fuels, which are thought to ensure a sustainable supply of energy sufficient for the growing global mobility. In this respect, significant research efforts have been directed to assess the applicability of biofuels and hydrogen within IC engines.

1.3.1. The advent of biofuels

Biofuels derive from biomass products, such as plants, crops and seaweeds. **(22, 23)** A vast array of literature has demonstrated that the use of biofuels mitigates appreciably the engines' environmental impact. This is attributable to their highly oxygenated nature, which benefits the combustion's thermal efficiency. As a result, a significant reduction in particulate matter (PM), carbon monoxide (CO) and unburnt hydrocarbons (UHC) ensues. By contrast, the larger content of oxygen gives rise to an albeit small increase in the NO_X emission. **(24)**

These characteristics have led to the hypothesis that biofuels might represent a long-term solution for IC mobility. **(25, 26)** However, the wide spread of biofuels might set the stage for a detrimental competition with food-purposed agriculture.

1.3.1.1. Categorisation of feedstocks for renewable fuels

In the light of the geopolitical scenarios determined by the nutrition-oriented agriculture, three categories of feedstock for biofuels' production were outlined. The first typology, which includes vegetable oils and grains, reflects the immediate efforts to break away from the fossil fuel dependence. By contrast, this option is believed to promote the risk of a baneful competition with nutrition-purposed farming. Such a drawback is enhanced by the large amount of water required for fuel production. **(27)** This has led to the introduction of the second category, namely the non-food biomass, including organic and food waste. **(28)** However, some biomasses require food-growing land, renewing the long-standing interaction with food-purposed agriculture.

As a consequence, a third category, including seaweeds, was singled out. Besides the resolution of the competition-related issue, the third generation presents advantages such as:

- higher energy density in comparison with the two previous categories;
- cost-effective maintenance;
- greater renewability.

By contrast, the production method of third-generation biofuels presents still wider margins of optimization. **(29)** To this end, Román-Leshkov proposed a cost-effective production methodology, which might be extended to a wider biofuels range. **(30)**

1.3.2. The wide spread of ethanol

Despite the wide range of alternative fuels, ethanol is the main automotive-purposed biofuel. **(31)** This wide spread is ascribable to its peculiarities benefiting the IC engine, such as its

high octane number and reduction in smoke. Besides these benefits, its great renewability highlights ethanol as a promising alternative to fossil fuels. **(32-37)**

By contrast, drawbacks such as:

- large volatility;
- low energy density;
- high energy consumption required by the production process;
- additional preheating, especially in climatic regions where cold conditions hinder the formation of an ignitable mixture **(37)**

jeopardize a world-scale spread, leading to the consideration of ethanol as a short-term solution.

1.3.3. The furan-based blends

This framework has driven the research community to turn their attention to furan-based fuels, production of which is feasible via the methodology developed by Dumesic and Román. **(30, 38)** An appealing biofuel, such as 2-methylfuran (MF), has been fiercely analyzed within SI and CI engines. In this respect, an accurate review is provided in this thesis, which is also purposed to fill the gap in knowledge of furan injection.

1.3.4. Hydrogen as a solution for the growing mobility demand

Its plentiful availability in nature, its renewability and favourable emissions of heat and water vapour make hydrogen an attractive candidate to supersede the traditional fossil counterparts. **(39, 40)** However, the worldwide usability of hydrogen is mainly jeopardised by safety concerns. **(41)** Therefore, the research community is required to raise automotive-purposed hydrogen technology to a satisfactory safety standard. This joint effort is justified also by the fact that hydrogen propulsion might be the bridging technology between the traditional fuelling methods, based on fossil fuel consumption, and the hydrogen fuel cell. (**42**)

1.4. The introduction of electric vehicles

The need for the minimisation of vehicles' carbon footprint has driven the automotive field to explore pathways alternative to IC mobility. In this respect, electric propulsion has gained the attention of the research community, giving rise to a heated debate about the *pros/cons* ratio related to use of electric vehicles. Indeed, if on the one hand electric propulsion does not produce tailpipe emissions and assures a closely surrounding green footprint, on the other, it is not yet deemed able to supersede entirely the IC engine, given drawbacks such as:

- insufficient widespread distribution of the charging infrastructures;
- long charging phase;
- low reliability for heavy-duty applications, such as trucks and escalators **(43)**;
- impact on the power generation serving the demand, including household purposes.

Besides these disadvantages, batteries present several concerns, **(44)** such as:

- environmental footprints stemming from the extraction and purification of raw materials compounding the battery;
- fast depletion of materials underlying the functioning of the batteries;
- impact of depleted/discarded batteries on long-term landfilling, with possible breakage and toxic infiltration into the soil;
- low cost-effectiveness of the reuse of automotive batteries. **(45)**

Despite these criticalities, electric mobility has been massively backed by governments. As a consequence, nowadays full-electric vehicles and engine hybrid cars are gaining progressively larger market shares. Nevertheless, electric mobility cannot be deemed ready to entirely supersede IC propulsion. Therefore, further investigations of renewable fuels would allow their potential to be assessed with a view of providing readily green mobility; as long as the world-scale spread of automotive-oriented electric technology becomes a viable pathway.

1.5. Objectives of the research activity

The above background prompted the author to undertake experimental activity addressed to clarify the impact of injection settings with the fuel properties on the characteristics of jet development. The analysis of the impact exerted by injection settings on the non-uniformity of jets' velocities at the early stages of the injection process was carried out.

The main goal was the investigation of injection settings which can favour the optimisation of the injection strategy. Indeed, although there is wide-ranging literature dealing with this topic, several aspects still represent a concern.

Besides the diesel, furan-based blends were also tested. This approach was motivated by the need to provide a wider overview of the potentiality of furan-based fuels for a wide applicability within the IC engine. In this respect, the paucity of data referring to the injection of furan-based blends prompted a part of this thesis' work.

In order to fill these knowledge gaps, a robust experimental campaign was thereby undertaken at the Department of Mechanical Engineering, in the School of Engineering at the University of Birmingham. The tests were performed on a CR test rig provided with:

- a diesel multi-hole injector;
- sensors;
- a high-pressure vessel reproducing the pressures typically operating in the cylinder;
- a high-speed camera for the acquisition of the fuel jets' images.

The research activity required the development of a novel transducer for the needle-lift detection and the assessment of rail pressure fluctuations. The reasoning behind this development came from the meaningful influence of injection pressure variations, arisen from the previous shots, on the jets' development. Therefore, both diesel and MF-based blends' rail pressure oscillations were rigorously investigated.

For consistency reasons, the injection settings reproducing the injection scenarios were the same for all the stages of this project. Alongside the design of a novel sensor, which revealed the non-negligible impact of backpressure on the time-history of needle displacement, the research activity presents novelties, since it differs from most of the studies dealing with these topics. In fact, these works deal with numerical simulations focusing on the non-uniformity of the injected mass flow rate.

1.5.1. Outline of the thesis

The thesis is structured on the basis of the injection process sequence schematised in Figure 1.11. The core part of the thesis was developed over four chapters, and aims at the progressive identification of the physical principles governing the non-uniformity of jets' velocities exiting a multi-hole injector.

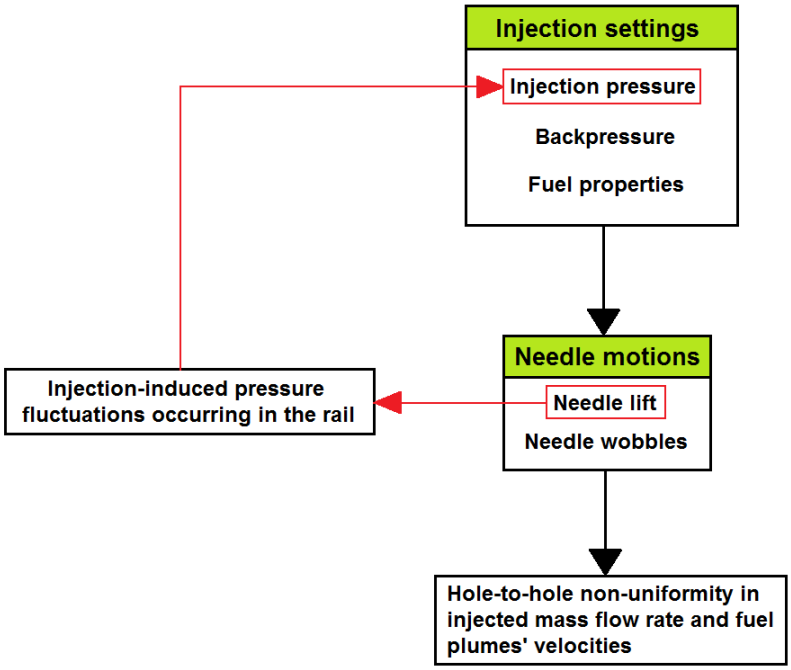


Figure 1.11. Schematisation of the injection event and topics investigated here

When applicable, a disclaimer is presented at the beginning of the chapter, if the work or part of it was published elsewhere by the author and reproduced with the co-authors' permission. Figure 1.12 schematises the path covered through the thesis; whilst the following sections

provide an overview of the chapters. The light blue rectangles refer to the main stages constituting this work, whilst the red rectangles present the scientific backgrounds motivating the developed topics through the thesis' project.

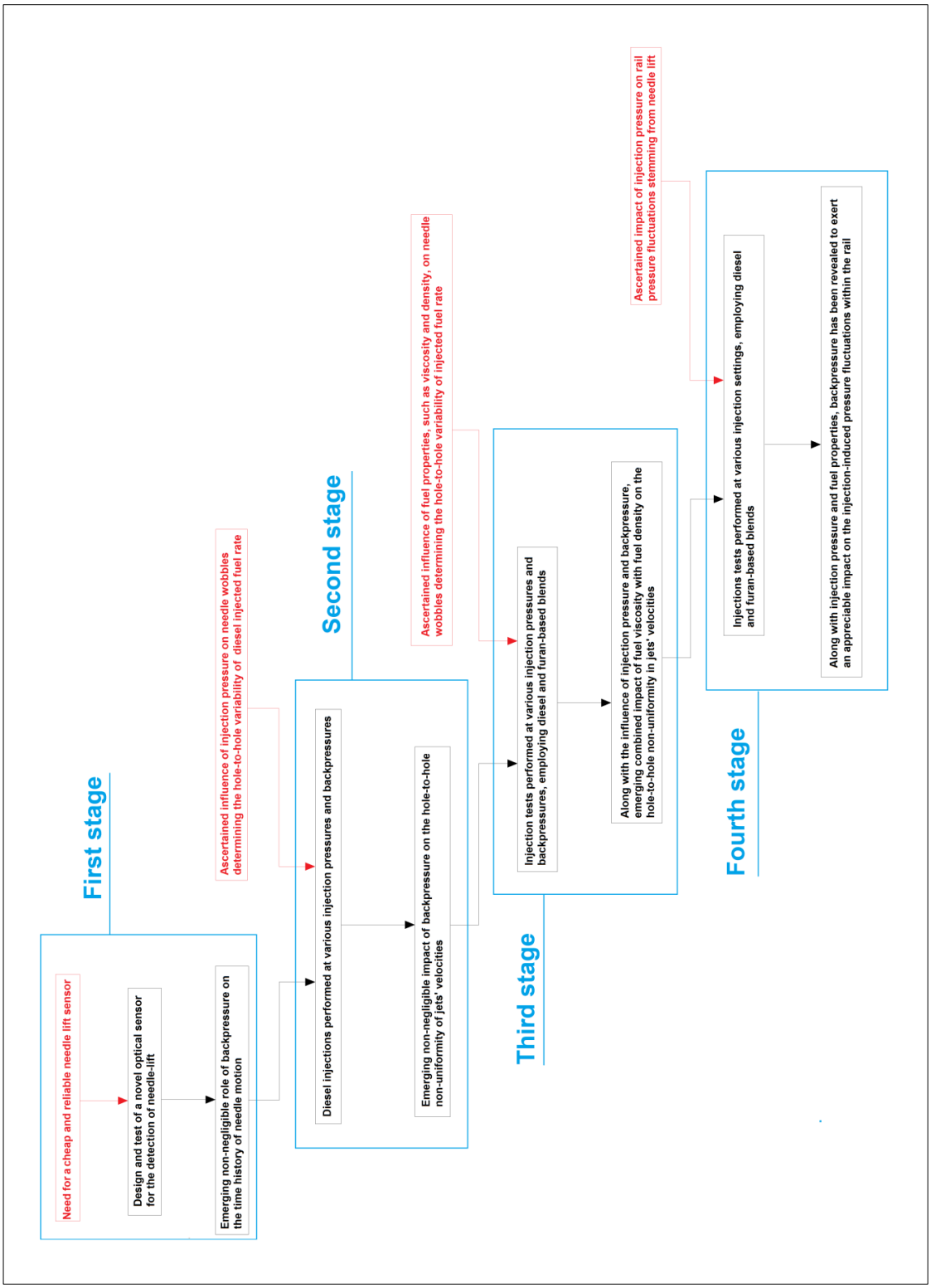


Figure 1.12. The schematised development of the thesis' work

Each chapter is structured so as to include an introduction comprising of the literature review pertinent to the objective under investigation. The methodology for the fulfilment of the objective is then given. Thereafter, results and findings are presented and discussed. This latter stage was crucial to highlight the novelties filling the related research gap. A conclusion is then given, providing the motivation underlying the subsequent chapter.

1.5.1.1. Chapter 2 - The sensor for needle motion detection

The chapter pertains to the design of a novel needle-lift transducer. Current techniques for this purpose and related drawbacks are reviewed, followed by the description of the proposed methodology and diesel injections' tests. Afterwards, the results are discussed, singling out the parameters determining needle displacement over the injection process. The findings emerging from this study underlie the objective of the next chapter.

1.5.1.2. Chapter 3 - Experimental assessment of the hole-to-hole non-uniformity of diesel jets' velocities

In the light of conclusions drawn from the previous findings, and bearing in mind the influence exerted by the needle on the imbalance of the injected fuel rate, this chapter focuses on the influence exerted by injection settings on the orifice-to-orifice variability of diesel jets' velocities at the early stages of the injection event. Firstly, the background is outlined, and then the tests are fully described, followed by the analysis of the results and the identification of the parameters determining the variability of the jets' velocities. Since the tests were conducted employing diesel, the findings prompted the author to undertake further tests employing different fuels, so as to assess the impact of the fuel properties on the above variability.

1.5.1.3. Chapter 4 - The hole-to-hole non-uniformity of the 2-MF-blend jets' velocities compared to diesel

Diesel tests served as a baseline for the objective of this chapter, namely the assessment of the hole-to-hole variability of the jets' velocities employing MF-based blends. The chapter is basically outlined as those previously. Along with orifice-to-orifice variability of the jets' velocities, also the delays of the injection were acquired and analysed as a function of the injection settings and the fuel properties. The scope was to provide a physical explanation of the combined impact of injection settings with the fuel properties on the above non-uniformity; this is thought to provide a further insight into the 2-MF applicability on the CI engine.

1.5.1.4. Chapter 5 - The injection-induced pressure fluctuations within the rail

This chapter is motivated by the key role of the injection settings and the fuel properties in the non-uniformity of the jets' velocities. In fact, it is well known that as the injection commences the needle lifts up, originating rail pressure fluctuations, which affect considerably the uniformity of the following jets' development. This was the reason behind the assessment of the combined influence of injection settings with the fuel properties on rail pressure fluctuations. Firstly, the literature pertinent to this topic is thoroughly reviewed, followed by an accurate description of the injection tests. The statistical analysis of the results is then provided, followed by the identification of the parameters affecting rail pressure fluctuations.

1.5.1.5. Chapter 6 - Summary and future recommendations

This chapter provides an overview of possible works to undertake on the basis of the key findings which emerged from this thesis.

CHAPTER 2

NOVEL SENSOR FOR DETECTION OF NEEDLE LIFT IN A COMMON RAIL INJECTOR

A considerable amount of this chapter has been presented at the 14th International Conference on Engines & Vehicles, held in Capri, Napoli (Italy) on 15th-19th September, 2019.

The results have been published in the following paper:

Coratella, C., Parry, L., Sahu, A., & Xu, H. (2019). 'Optical Sensor for the Needle Lift Detection in the Common Rail Injector' (No. 2019-24-0193). *SAE Technical Paper*.

The technique described in this chapter has been patented (Patent Application **GB1819731.9**) and is currently under PCT procedure (**International Patent Application No. PCT/EP2019/083475**).

https://www.birmingham.ac.uk/partners/enterprise/Fuel-injector.aspx

https://micragateway.org/our-services/ip-for-licence/fuel-injector-with-a-piston-motion-sensor/

Cummins Research team has shown interest in the invention and is looking to potentially acquire the following described technology.

Introduction

The advent of the electronically managed injection has represented a milestone for the development of the modern engine, in terms of performance abiding by the environmental mandates. The success of this technology is mainly due to the flexibility and faster response

of the injector actuation. This cutting-edge technology has appreciably improved the accuracy of the amount of injected fuel. Nonetheless, the increasingly stringent emission regulations have urged the engine manufacturers to optimise this technology. This has led to the generation of several models predicting the injector's behaviour; taking mass flow rate, **(46-50)** injection pressure, **(51-57)** and needle displacement into account. **(58-64)**

2.1. The key role of needle motion in the injection characterisation

Concerning the detection of needle displacement, a vast array of literature has highlighted its pivotal role in the injection process' characterisation, given its influence on in-nozzle phenomena, such as cavitation onset and imbalance of injected flow rate.

2.1.1. The influence of needle lift on the cavitation onset

It was widely proven that needle lift plays a crucial role in the cavitation onset; the location of which is determined by the mutual position of the holes and the needle. Several studies assessed this correlation both via experimental and numerical approaches.

Payri *et al.* found that needle motion affects cavitation inception where the lowest flow velocities arise through the closest orifice to the needle. **(58, 59)** More specifically, it was observed that along with pressure fluctuations upstream of the needle seat, the needle position exerts a significant impact on the liquid column inertia.

A further insight into the influence of needle lift on phenomena taking place within the orifice was provided by Arcoumanis *et al.* **(60)** They demonstrated that needle lift determines the cavitation onset and its length, using a transparent nozzle of a diesel injector provided with six holes. From this investigation, a correlation between needle position and the onset of cavitation was observable. Typically, for high needle lifts, it was found that cavitation takes places along the upper part of the orifice. The length of the vapour phase decreases as needle lift is reduced.

Likewise, Chaves and Kirmse found that at various needle lifts, cavitating flow development at the orifice inlet is subjected to non-uniformity, despite unvaried injection pressure. **(65-67)**

A further insight into the correlation between the needle position and cavitation inception was provided by Miranda *et al.*, who observed that cavitation magnitude tends to be weakened at low needle lifts. **(56)** In the wake of the above studies, Badock *et al.* carried out an experimental investigation replacing an one-hole nozzle with a transparent nozzle. **(69, 70)** Unlike Miranda *et al.*, Badock *et al.* analysed the cavitation development over the injector opening and closing stages, taking needle lift into account. While Som *et al.* demonstrated that along with injection setting and fuel properties, the needle position also significantly affects the appearance of cavitation. **(71)**

2.1.2. The impact of needle lift on the mass flow rate

Besides the cavitation onset, the mass flow rate is considerably affected by needle motion. Wang *et al.* investigated the correlation of injected mass flow rate with fuel temperature, highlighting the relevance of needle lift detection over the injection event **(46)**. Zhong *et al.* showed that needle lift exerts a significant influence on the cycle-to-cycle variations in rail pressure, which in turn determine the amount of fuel injected. **(56)** Similarly, Payri *et al.* found that needle motion plays a pivotal role for the inlet flow conditions where the lowest flow velocities arise through the closest hole to the needle. **(58, 59)** Whilst likewise, Arcoumanis *et al.* demonstrated that the stationary flow conditions are strongly affected by the needle position within a VCO injector. **(60)** Furthermore, Soriano *et al.* carried out a numerical investigation dealing with the mass flow values at various needle lifts against experimental data during the injector's opening. **(72)**

2.2. The current devices for needle motion detection

Besides the difficult accessibility to the nozzle's internal areas, the high pressures acting therein discourages the detection of needle lift. The installation of a sensor is further impeded by the decreased mechanical resistance of the nozzle stemming from the machining process. **(73-75)** Therefore, manufacturers have oriented their efforts to develop control piston motion-purposed sensors. This approach has been justified by the fact that the needle and control piston remain in contact over the injection process. Eddy current sensors are commonly employed to measure the control piston motion. Nevertheless, once the current pulse (≈ 20 A) is delivered by the ECU to the solenoid for the injector opening, an electromagnetic interference arises. **(73-75)** These electromagnetic fields are captured by the transducer as noise, hindering the acquisition of the control piston displacement (Figure 2.1).

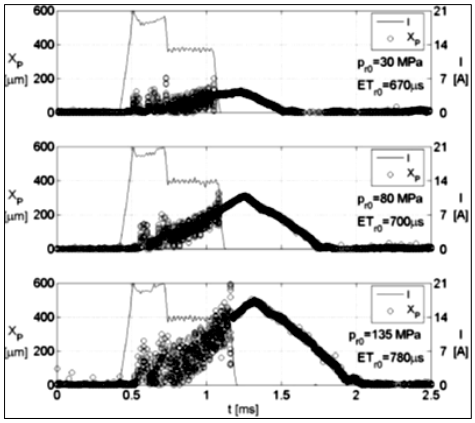


Figure 2.1. The electromagnetic fields, arisen from the current signal, are captured by the eddy currents transducer as noise, affecting negatively the detection of the control piston displacement **(75)**

An additional drawback is the mechanical weakness ensuing from the frusto-conical surface on the control piston **(73-75)** required for the sensor installation (Figure 2.2).

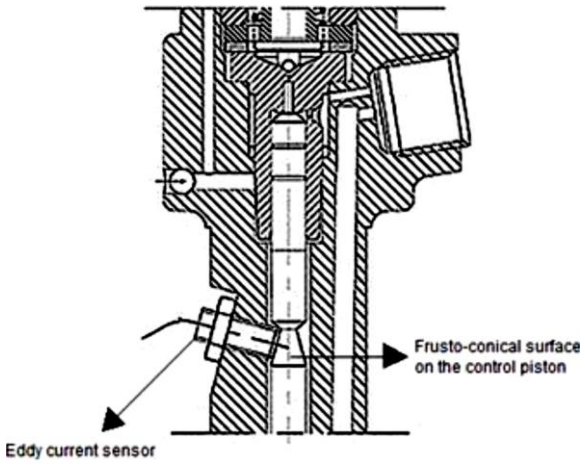


Figure 2.2. The frusto-conical surface, machined on the control piston for the installation of the eddy current sensor, gives rise to greater mechanical weakness **(73-75)**

As the control piston lifts up, the effects due to the geometric discontinuity are accentuated, enhancing the mechanical stress. Thus, a higher risk of mechanical fracture arises. Besides the high costs, these drawbacks discourage this technique, which is deployed only for lab applications. This framework has led to the design of alternative devices, such as optical solutions. These solutions were found to solve the above issues. Nevertheless, these techniques are characterised by layout complexity, caused by the large number of components. Indeed, once the injection commences, the abrupt upward motion of the control piston generates the formation of bubbles. This underlies the light scattering **(75)**; which hinders the acquisition of the control piston motion. It is noteworthy that scattering light dispersion is further boosted by fuel flowing along the control piston and entering the sensor area. **(73, 74)** These drawbacks require the employment of gaskets, a pressurised air supply and drainage pipes, so as to keep the fuel away from the measurement area. However, if on the one hand these solutions assure excellent cleanliness of the displacement signal, on the other the layout complexity is increased. In summary, criticalities such as:

- electromagnetic interference;
- minimised mechanical resistance of the control piston;
- onset of cavitation;

- backflow fuel along the control piston

discourage needle lift detection. Therefore, in the light of these issues, and as needle lift measurement is a key step for an accurate injection characterisation, the development of an innovative sensor still represents a challenging task.

2.3. The optical fibre-based sensor

In order to overcome the aforementioned limitations, an optical fibre-based sensor was designed and tested under various scenarios. The novel device is described in this chapter, which is outlined as follows. Section 2.3 describes the sensor's design, the electronics and the reasons prompting the creation of the proposed device. Section 2.4 pertains to the set-up, Section 2.5 deals with the injection tests. The results are fully discussed in section 2.6, followed by the conclusions.

2.3.1. The design of the optic fibre-based sensor

Figure 2.3 sketches the layout of the sensor, which is basically compounded by an emitter, a receiver and an optical fibre. The optical cable is positioned into the through holes machined on the injector body and the control piston. As the injection commences, the control piston drags the optical cable up along a vertical slot located within a tiny cylinder placed in the detector cavity. The slot width is equal to the optical cable's diameter.

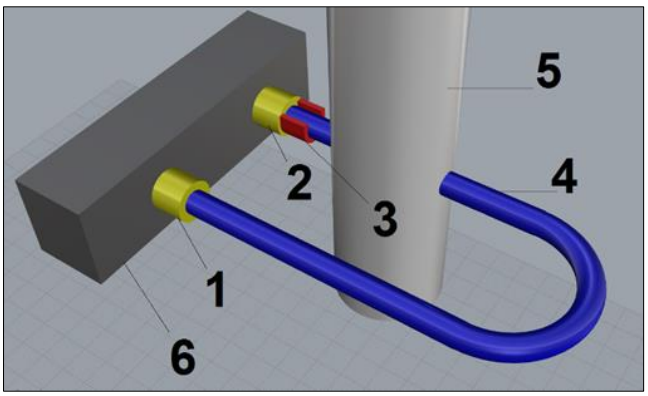


Figure 2.3. Schematic layout of the sensor: 1- Emitter, 2 - Receiver, 3 - Grooved cylinder placed within the detector, 4 - Optical fibre, 5 - Injector body, 6 - Electric circuit box

The operating principle is based on a light beam generated by the emitter. The light beam travels along an optical cable and is detected by a receiver. The output voltage from the receiver is determined by the light falling on the detector. As the injection starts, the fibre is dragged up by the control piston, causing an increasing overlap between the optical cable's end and the receiver's surface (Figure 2.4).

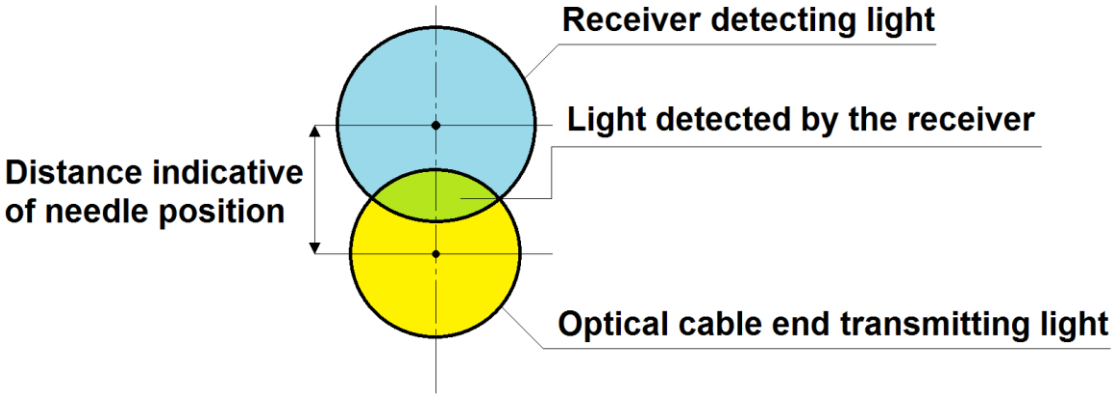


Figure 2.4. Mutual position between the circles; indicative of the optical cable's end and the receiver, determining the intersection area, meaningful of the control piston's position

The area of interest is determined by the overlapping area between the cable's end and the detector. In geometrical terms, the mutual position between the end of the optical fibre and the detector generates an intersection region, which is meaningful of the control piston's position. The sensor provides a voltage output, which is displayed and logged via an oscilloscope. Particular attention was paid to the positioning of the optical cable's end at the lower edge of the detector. Figure 2.5 shows a circular hole on the injector body (a), and the mutual position of the through holes at stand-by configuration of the injector (b).



(a) (b)

Figure 2.5. The geometry of the holes on the injector body (a), (b) and on the control piston. The mutual position of the through holes at stand-by configuration of injector (b).

The diameter of the circular holes machined on the injector and on the control piston is equal to that of the optical cable (≈ 0.48 mm). The other hole on the injector body is slotted, so as to enable the optical cable to be dragged up by the control piston. The height of the slotted hole is 1 mm, while its width is equal to the diameter of the optical fibre (Figure 2.6).



Figure 2.6. The slotted hole on the injector body

Bearing in mind that the maximum lift of the control piston is approximately 0.5 mm, **(73-75)** a similar height for the holes has been set so as to ensure the accurate detection of the control piston motion over the injection process. It is worth noting that the machining required for this technique implies a noticeably minimised notched section, since the through hole on the control piston minimises the surrounding stress state.

Furthermore, the optical cable through the hole is devoid of the outer jacket, so as require a smaller drilled hole-size. This solution alleviates the stress state surrounding the hole on the control piston. This peculiarity is further highlighted if compared with other solutions, which are characterised by an accentuated notched section. It is worth noting that the hole on the injector body causes a small leakage of the backflow fuel. In this regard, the estimation of this loss was discouraged by the difficult physical accessibility to the narrow measurement area. Therefore, the installation of dedicated measuring instruments is impeded. Moreover, this option is believed to increase the complexity of the sensor layout. However, bearing in mind

that the backflow fuel along the control piston is at atmospheric pressure, **(73, 74)** further designs will be developed in the future in order to avoid these leakages.

2.3.2. The sensor's electric circuit

The electric circuit and related diagram are shown in Figures 2.7 and 2.8, respectively. The circuit is connected to an oscilloscope, which enables the output voltage from the detector to be visualised and recorded.

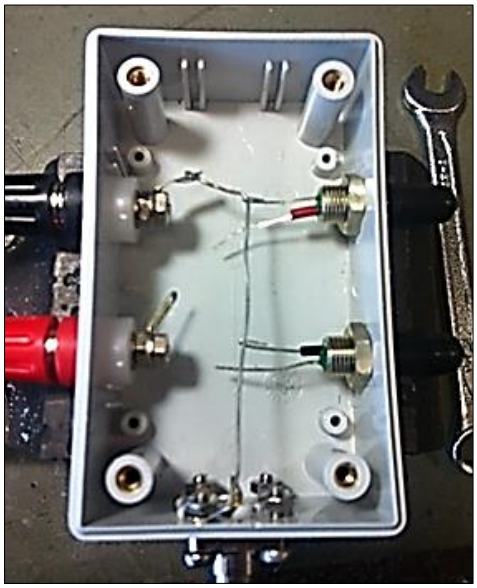


Figure 2.7. The electric circuit feeding the optical sensor

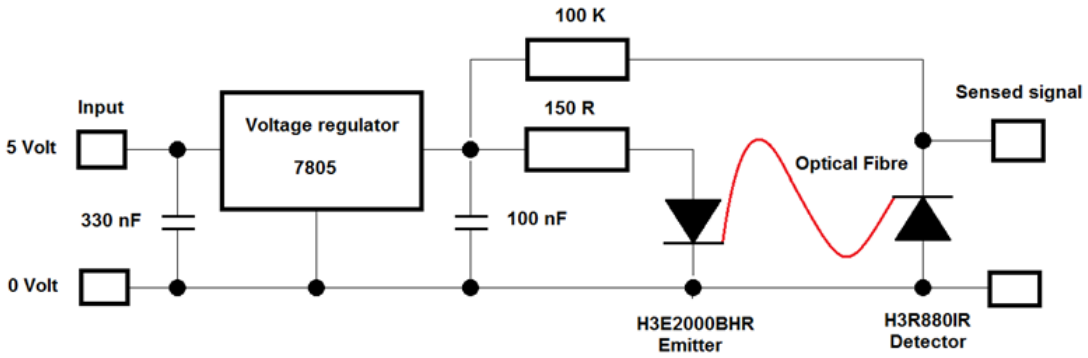


Figure 2.8. Schematic diagram of the sensor's circuit

The light is emitted by an H3E2000BHR transmitter manufactured by OMC and suitable for optical fibre-based applications. The H3E2000BHR is provided with an LED emitter, which is able to emit light with a wavelength of 660 nm. It is characterised by good levels of power

into other multimode fibre types and a fast response time which makes it suitable for this application. The detector is a H3R880IR type which is easily integrated with the H3E2000BHR. The H3E2000BHR emitter is biased for 20 mA current consumption. The reverse-biased H3R880IR receiver conducts less 50 μA and operates in a quasi-linear region. The optical fibre is a multi-mode A65A152A0 type, made of hard-clad silica and provided with 9 mm connectors compatible with the transmitter and receiver. The 200/230 μm glass fibre leads are manufactured from the tight jacket cable, with FSMA connectors.

2.3.3. Reasons motivating the optical fibre-based technique

Optic-fibre-based sensors have drawn considerable interest from the research community over the last few decades. **(76-79)** This has implied the outstanding growth of the optical fibres as sensing elements, given peculiarities such as:

- insensitivity to electromagnetic disturbance;
- high benchmark of signal cleanliness;
- resistance to hostile environments;
- low weight;
- downsized layout;
- cost effectiveness.

These benefits make optical fibres attractive candidates to cover a wide range of sensing applications, superseding the conventional counterparts. This scenario led the author to design the present transducer, so as to overcome the limitations typically related to the needle lift sensors.

2.4. The experimental set-up

In order to assess the suitability of the proposed sensor, the test rig is a *STPiW2* type, manufactured by *Autoelektronika* (Figure 2.9).



Figure 2.9. The CR test bench, a STPiW2 type manufactured by Autoelektronika

The test rig includes a high-pressure pump, which is driven by a 2.2 kW 1-phase AC motor by means of a transmission belt and is able to supply injection pressures up to 1500 bar. Injection pressure and rotational speed of the electric motor are managed by means of a control unit and a single-phase inverter, respectively. Figure 2.10 provides an overview of the set-up including additional devices to the CR rig.

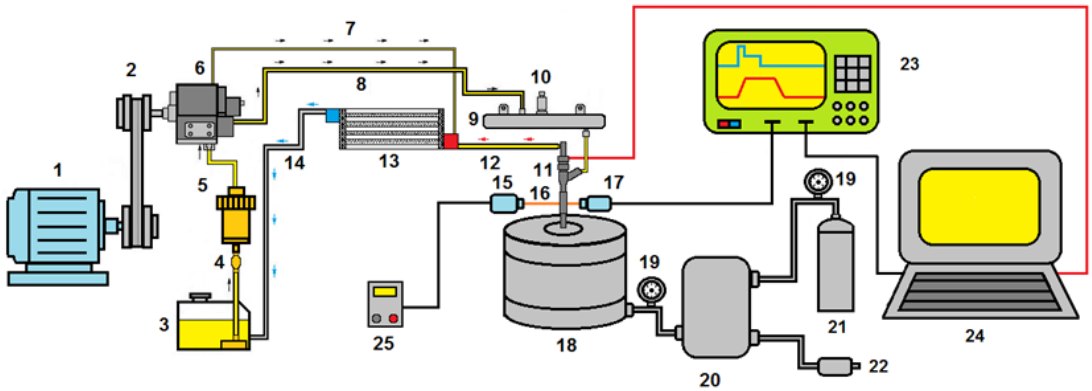


Figure 2.10. Test rig: 1 – Electric Motor; 2 - Transmission belt; 3 – Tank; 4 – Filter; 5 – Low-pressure pump; 6 – High-pressure Pump; 7 – Backflow fuel by the high-pressure pump to heat exchanger; 8 – Highly pressurised fuel line; 9 – Common rail; 10 – Pressure regulating valve; 11 – Injector; 12 – Backflow fuel line; 13 – Heat exchanger; 14 – Return cooled fuel line; 15 – Emitter; 16 – Optical fibre; 17 – Receiver; 18 – High-pressure vessel; 19 – Pressure gauges; 20 – Pressurised air chamber; 21 – Pressurised air tank; 22 – Relief valve; 23 – Oscilloscope; 24 – Computer; 25 – Voltage supplier

The rail is provided with a fuel pressure sensor, manufactured by Bosch and identifiable by the code 0 281 002 498 (Figure 2.11).

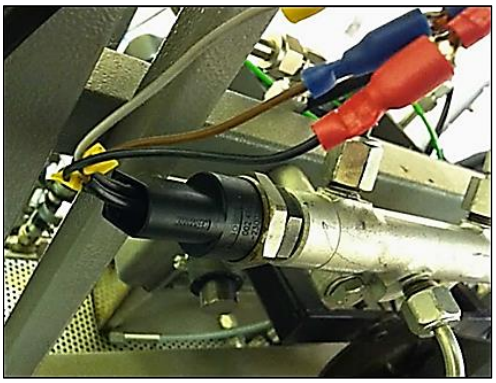


Figure 2.11. The fuel pressure sensor mounted onto the common rail

The backflow fuel is cooled by means of a heat exchanger before flowing back towards the tank. The heat exchanger's efficiency is monitored via a microcontroller. The injection timing and duration were set via a dedicated program implemented in ECKA environment. The CR injector is a solenoid-driven type, manufactured by Denso and provided with seven holes of 0.15-mm diameter. The injector is fitted to a high-pressure vessel (HPV), which is able to store backpressures up to 110 bar (Figure 2.12).

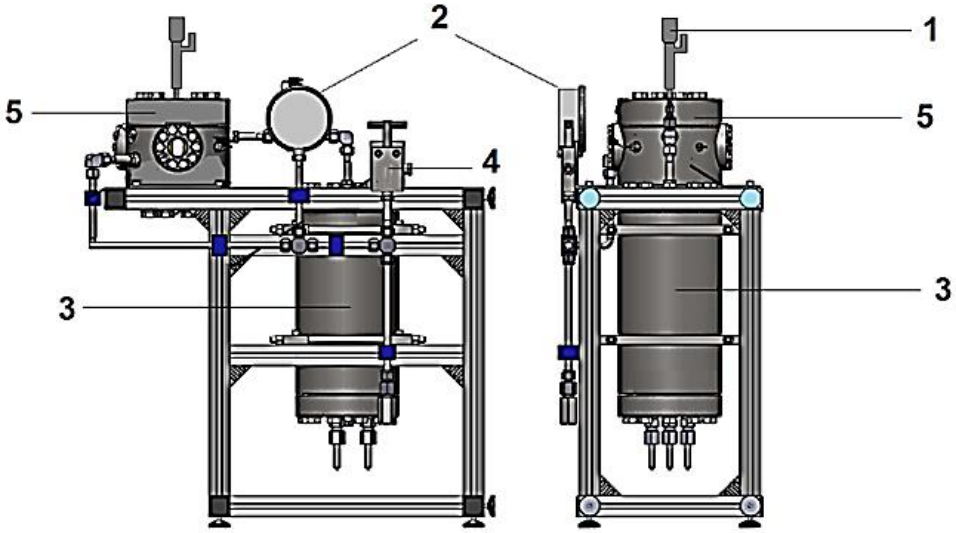


Figure 2.12. Front and side views of layout of the highly pressurised system: 1 – CR injector; 2 – Pressure gauge; 3 – High-pressure vessel; 4 – Relief valve; 5 – Pressurised air chamber

The HPV enables the reproduction of various operating scenarios and was revealed to be crucial for the characterisation of the injection process. In this regard, a detailed explanation of the findings is provided in section 2.6. The following figure shows the sensor installed on the injector, which is mounted on the highly pressurised chamber.

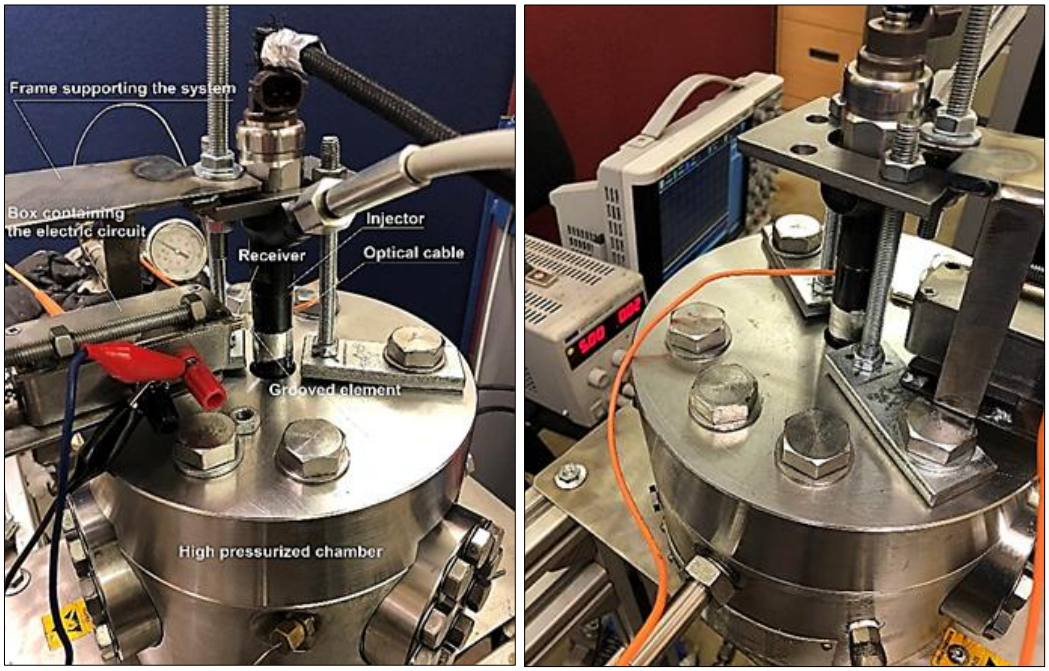


Figure 2.13. Overall layout of the experimental set-up including the highly pressurised chamber, oscilloscope, frame supporting the circuit box and voltage supplier feeding the circuit

In order to align the optical cable's end to the detector, a frame was manufactured. This solution allowed adjustment of the mutual position between the sensor and injector by means of a screw. The injection timing and duration were set via an ECKA program.

2.5. The diesel injection tests

In order to assess the reliability and accuracy of the proposed sensor, a robust experimental campaign was undertaken. The injection pressure was set at 400, 700, 1000 and 1400 bar; and the backpressure was set at 20, 40, 60 and 80 bar for each injection pressure. The energising time was set to 2000 μs. Once the output voltage was acquired, it was processed via the moving average. As a result, the fluctuations were smoothened, thus highlighting the trend of

the voltage signal and meaningful of the control piston displacement. Figures 2.14-2.17 depict the time-history of the control piston displacement as well as the current profile, characterised by the peak and hold times.

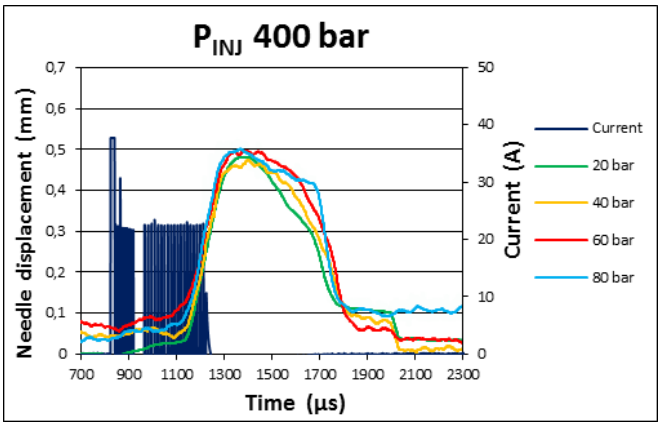


Figure 2.14. Needle motion detected at an injection pressure of 400 bar and various backpressures

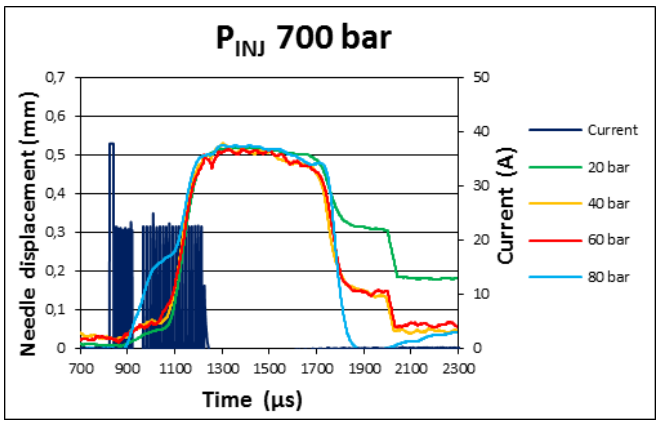


Figure 2.15. Needle motion detected at an injection pressure of 700 bar and various backpressures

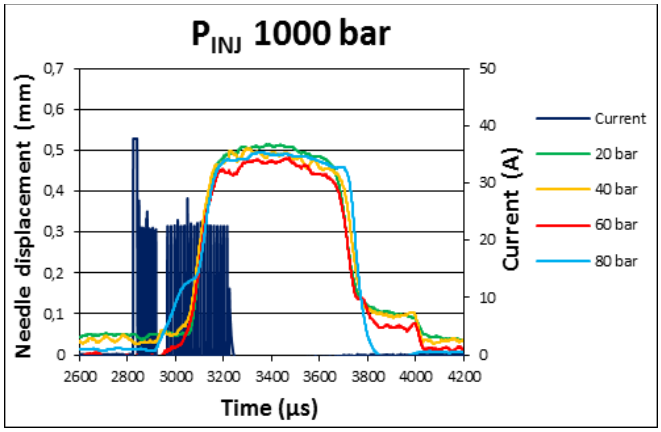


Figure 2.16. Needle motion detected at an injection pressure of 1000 bar and various backpressures

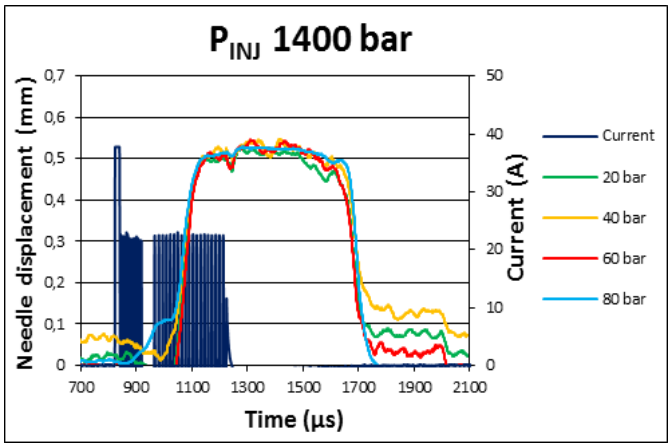


Figure 2.17. Needle motion detected at an injection pressure of 1400 bar and various backpressures

In the light of Figures 2.14-2.17, the sensor is revealed to follow the needle's motion over a wide range of injection scenarios. The curve of the plotting needle motion is devoid of any interference signal, given the optical nature of the sensor. Knowing that the maximum control piston lift is approximately half a millimetre, and bearing in mind the fairly linear relationship of the receiver's output voltage with the detected light intensity indicative of the displacement, it is possible to correlate the output voltage with the control piston position. In this regard, King *et al.* found that the light intensity detected by the receiver is linearly proportional to the output voltage. **(80)** Additionally, Dongiovanni *et al.* found that the light intensity detected by the receiver is linearly proportional to the passage area of the light beam. **(75)** They also demonstrated that the output voltage is linearly proportional to the control piston displacement. In light of these findings, the coefficient of proportionality between the output voltage and the control piston displacement is calculated taking the maximum variation of voltage output, which corresponds to the flat part indicating the highest lift, into account. For main injections, the maximum variation of output voltage indicative of the highest control piston lift, was found to be around 0.0112 ± 0.005 V. At unvaried injection pressure and backpressure, the coefficient is then employed to estimate the needle lift for the pilot injection. It emerges also that greater injection pressure and backpressure result in faster upward motion of the control piston. The reasons underlying this phenomenon are explained

in the next section. Moreover, at the end of the injector's closing stage, in some cases the needle displacement signal does not return to zero. This might be ascribed to movement restriction of the optical cable from the grooved cylinder. Nonetheless, it is possible to identify the injector's closure by observing a plateau of voltage after a significant signal falling edge. Furthermore, it also emerges that there is a discrepancy between the set energising time and the current duration delivered to the injectors. This might be due to the on-board capacitors on the injection control unit. These capacitors are charged with current over a set time before discharging for a shorter period. Pilot injections were performed to assess the device's ability to detect even small lifts (Figures 2.18-2.20).

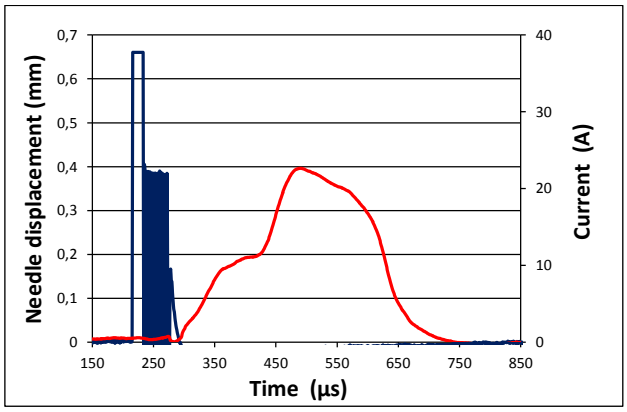


Figure 2.18. Needle motion referring to the pilot performed at 1400 bar and 60 bar. The energising time was set at 300 µs.

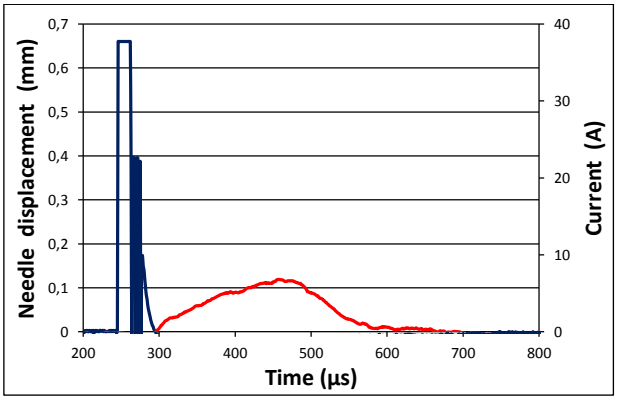


Figure 2.19. Needle motion referring to the pilot performed at 1400 bar and 80 bar. The energising time was set at 150 µs.

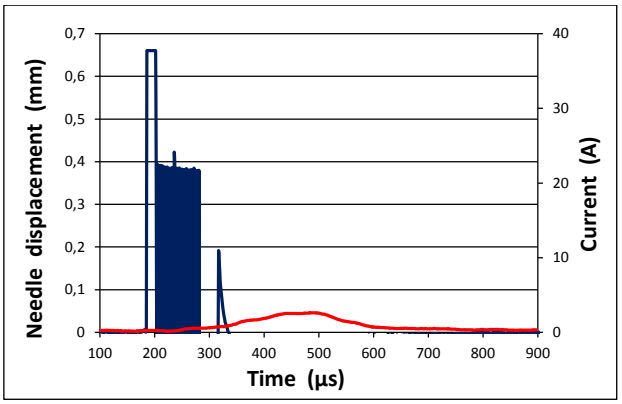


Figure 2.20. Needle motion referring to the pilot performed at 400 bar and 20 bar. The energising time was set at 650 µs.

It can be seen that the sensor is able to follow even small displacements, typical of pilot injections. Figure 2.20 refers to the injections performed at a low injection pressure and low backpressure, so as to minimise the effect of fuel momentum supplied to the needle. As a result, a small and slower ascending motion of the needle ensues. In this regard, the combined impact of injection pressure with backpressure on the fuel momentum determining the needle motion is reviewed in-depth in the following section. In conclusion, the tests demonstrated that the transducer is able to detect needle displacement with sufficient temporal resolution over a wide range of injection conditions.

2.6. The assessment of the time history of the needle motion

For a main injection, the time-history of the needle motion can be discriminated into three stages, referring to the lift, the plateau stage, and the downward motion. The following subsections provide an accurate description of the parameters governing these three stages of needle displacement.

2.6.1. The assessment of needle lift

The *rise time* is given by the time required by the needle to reach the highest position during the main injection. The rise times for different injection configurations are listed in Table 2.1.

Table 2.1. The rise time of the needle at various injection and backpressures

	20 bar	**40 bar**	**60 bar**	**80 bar**
P_{INJ} 400 bar	450 µs	400 µs	400 µs	400 µs
P_{INJ} 700 bar	350 µs	350 µs	350 µs	280 µs
P_{INJ} 1000 bar	300 µs	280 µs	280 µs	250 µs
P_{INJ} 1400 bar	280 µs	250 µs	250 µs	250 µs

Figure 2.21 plots the data in Table 2.1, so as to represent the observations in a coherent manner.

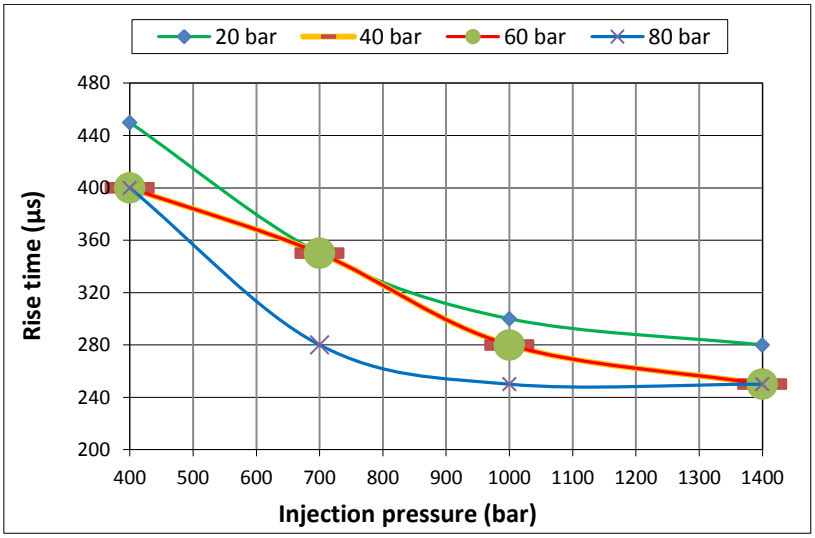


Figure 2.21. The variation in rise time of needle motion at various injection pressures and backpressures

Needle lift is observed to be more immediate at greater injection pressures. This trend is observed at all backpressures. Besides, it is worth noting that high backpressure leads to more rapid needle lift. This may be attributed to the barrier effect exerted by the greater backpressure on fuel flow towards the orifices. As a consequence, the fuel momentum is promoted towards the needle rather than towards the orifice, causing a greater needle acceleration. By contrast, lower backpressures are supposed to promote the fuel momentum towards the orifice inlet, alleviating the momentum towards to the needle protrusion. In physical terms, a larger fraction of the momentum which is potentially transferrable to the needle is lost towards the orifice. As a result, the needle is subjected to a weaker acceleration, which prolongs the rise time at low backpressures, in comparison with the case of unvaried

injection pressure and greater backpressure. In light of these observations, it can be argued that fuel momentum can be divided into two components. Figure 2.22 sketches the physical interpretation, which serves as a baseline for the discussion of the results in the next chapter.

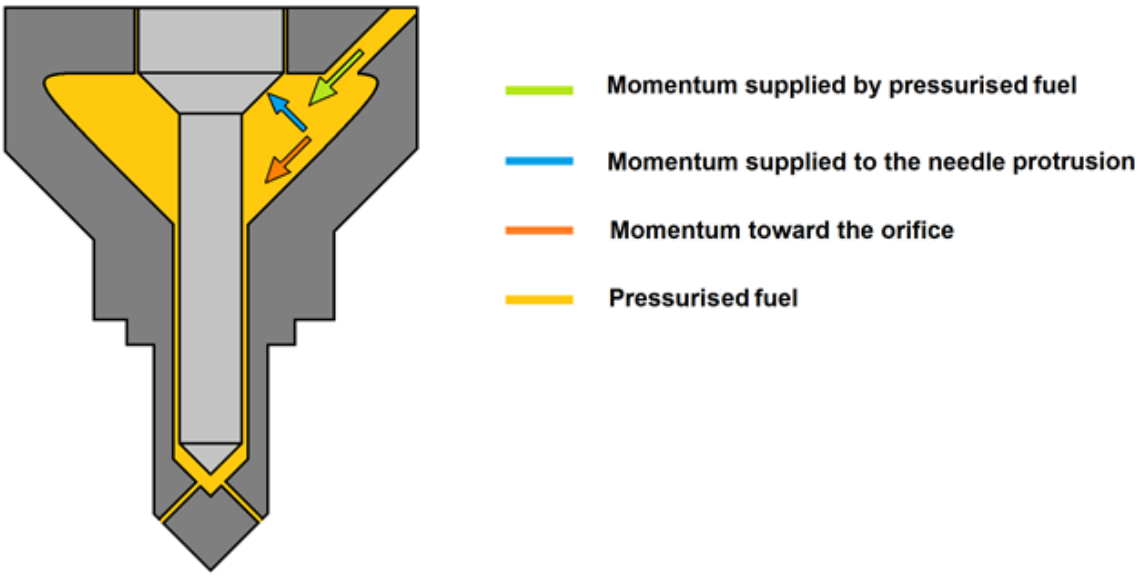


Figure 2.22. Pressurised fuel momentum can be discriminated into two components

This assumption explains the shortening rise time, indicative of a faster lift, observable at increasing injection pressure and unvaried backpressure. These considerations lead to the concept that the upward motion of the needle-control piston assembly can be approximately described by the following equation:

$$p_{INJ} \cdot A_{NP} + BP^* \cdot A_{NP} - (\Delta V \cdot S \cdot \mu)/\delta - p^* \cdot A_{CPT} = (m_N + m_{CP}) \cdot a_N \qquad (2.1)$$

where p_{INJ}, A_{NP}, BP^*, ΔV, S, μ, δ , p^*, A_{CPT}, m and a stand for: injection pressure; the area of needle protrusion; the contribution of backpressure on the needle protrusion; the relative velocity between the needle and fuel flow; the needle's cylindrical surface in contact with the fuel flow; fuel dynamic viscosity; the boundary layer thickness; the varying pressure within the control chamber; the area of the control piston top; mass, and the acceleration of the needle-control piston assembly, respectively. However, this conjecture is worthy of further investigations. Moreover, it can be seen that at a backpressure of 60 bar and 80 bar, needle lift

is discriminated into two stages (Figures 2.14-2.17). This may be attributed to the high injection pressure and backpressure promoting the fuel momentum potentially transferable onto the needle, which experiences a faster lift. Greater acceleration engenders a stronger dragging action on the optical cable. As a consequence, a difference between the velocities of the optical fibre and the control piston arises at the early stages of the control piston lift. In this regard, from Table 2.2 it emerges that increasing the injection pressure at a backpressure of 80 bar results in a larger difference between these velocities. Additionally, Table 2.2 shows the so-called recovery time, namely the time interval needed for the optical cable to retrieve the control piston velocity.

Table 2.2. The impact of the dragging action of the control piston on the optical fibre at various injection settings

	700 – 80 bar	**1000 – 80 bar**	**1400 – 80 bar**	**1400 – 60 bar**
Control piston velocity (m/s)	3	4	6	5
Optical fibre velocity (m/s)	2	2	2,5	2,8
Recovery time (μs)	200	160	130	125

It can be seen that increasing injection pressure shortens the recovery time. This may be attributed to the more abrupt needle lift following the increase in injection pressure. Thus, the fibre recovers velocity because of the stronger dragging action of the control piston. It is noteworthy that this disagreement occurs at an increasing injection pressure and a backpressure of 80 bar. It can be then argued that the increase in injection pressure at a higher backpressure promotes the needle lift. This finding may be based on the boosting impact of higher injection pressure with greater backpressure on the needle lift. Hence, a stronger impact of the dragging action of the control piston on the optical cable arises, determining a larger difference between the above velocities as well as a shorter recovery time. On the other hand, at a slower needle lift, this discrepancy is not observed. Nonetheless, said two-step behaviour is not observed in Figure 2.17, in spite of the high values of injection pressure and backpressure. This may be ascribable to the very short duration of the current pulse supplied

to the solenoid. A weaker force, originating from solenoid energisation, is not sufficient to engender a lift of the ball valve (Figure 1.8); hence, the needle experiences a slower lift. It follows that the needle starts the descending motion, preventing the lift from being discriminated into two stages even at higher injection pressure and backpressure.

2.6.2. The assessment of the needle hold time

Once the needle reaches the maximum position, it keeps this position for a time period, here referred to as the *hold time*, depending on injection pressure and backpressure. The *hold time* is indeed given by the duration of the needle's highest position observable at main injections. Table 2.3 shows that increasing injection pressures prolong the hold time.

Table 2.3. The duration of the needle maximum position at various injection and backpressures

	20 bar	**40 bar**	**60 bar**	**80 bar**
P_{INJ} 400 bar	Non-estimable	200 µs	200 µs	500 µs
P_{INJ} 700 bar	450 µs	450 µs	450 µs	500 µs
P_{INJ} 1000 bar	500 µs	550 µs	550 µs	550 µs
P_{INJ} 1400 bar	500 µs	550 µs	550 µs	550 µs

As with the rise time, greater backpressure is observed to prolong the hold time (Figure 2.23).

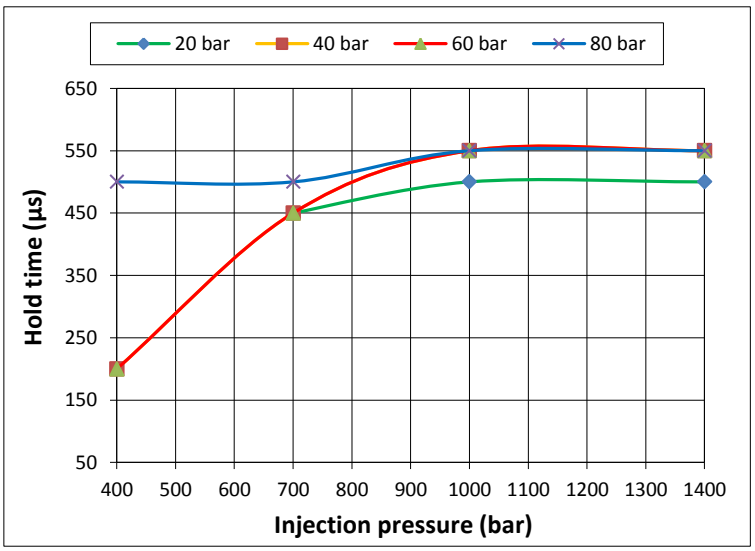


Figure 2.23. The hold time varies with injection pressure and backpressure

Equation 2.1 leads to the consideration that the lowest injection pressure and backpressure do not favour a faster lift, delaying the appearance of the plateau stage.

2.6.3. The assessment of the needle's downward motion

Bearing in mind Figure 1.8, it can be argued that once the control piston-needle assembly commences the downward motion, fuel pressure acts both on the control piston top and on the needle. Table 2.4 lists the duration of the injector's closure at set injection configurations.

Table 2.4. The duration of the injector's closing stage at various injection and backpressures

	20 bar	**40 bar**	**60 bar**	**80 bar**
P_{INJ} 400 bar	440 µs	390 µs	330 µs	160 µs
P_{INJ} 700 bar	190 µs	150 µs	150 µs	140 µs
P_{INJ} 1000 bar	200 µs	150 µs	200 µs	130 µs
P_{INJ} 1400 bar	140 µs	140 µs	140 µs	120 µs

In this regard, Figure 2.24 depicts the relationship between injection pressure, backpressure and duration of the injector's closing.

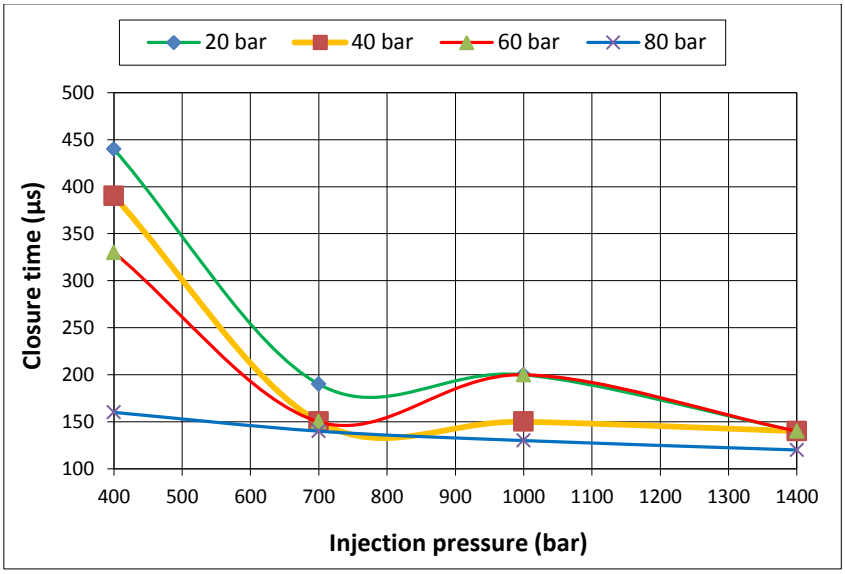


Figure 2.24. The injector's closing stage is a function of the injection pressure and backpressure

It emerges that at unvaried backpressure, an increase in injection pressure shortens the injector's closure duration. Similarly, at a constant injection pressure, an increase in backpressure shortens the closure time. Moreover, the largest reduction in closure time can be seen at an increasing injection pressure and at the lowest backpressure. By contrast, the shortest durations and the smallest reductions are observed at the highest backpressure. These findings might be attributable to the boosting impact exerted by greater backpressure on the control piston-needle assembly during the injector's closure stage. Indeed, higher backpressure serves as a stronger barrier, against the fuel flow towards the orifices. On the other hand, this barrier effect is believed to promote fuel flow towards the control chamber through the *Z-hole*, resulting in faster increasing in the pressure acting therein. As a result, this gives rise to a more rapid process of filling the control chamber, determining a faster downward motion of the control piston-needle assembly, and a shorter injector closure. The injector's closure can be expressed as a function of the injection pressure and backpressure. This stage can be approximately described by the following equation:

$$F_{CP}(t) - F_{NP}(t) = (m_{CP} + m_N) \cdot a_N \qquad (2.2)$$

where F_{CP}, t, F_{NP}, m_N and a stand for: force exerted by pressurised fuel on the control piston's top; time; force exerted by pressurised fuel on the needle protrusion; needle mass; and needle acceleration, respectively.

As shown in Equation 2.2, the force on the top of the control piston varies with time, because of the process of filling the control chamber. Keeping in mind that lower backpressures promote the flow towards the orifice, the filling process of the control chamber is slowed down. Hence, the force pushing the control piston down increases more slowly, and the injector's closure is prolonged.

Besides the boosting action on the control piston-needle during the closure stage, greater backpressure also promotes the entrainment of air bubbles through the injector's orifices. This is thought to imply there is a dilution of the fuel within the delivery chamber during the injection process, weakening the resistance opposing the downward motion of the control piston-needle assembly. A more rapid injector closure ensues.

2.7. Summary

In order to overcome limitations typically characterising the needle lift sensors, such as:

- complex layout;
- electromagnetic interference hindering the signal acquisition;
- noticeable notched effect on the control piston;
- impact of backflow hindering the signal acquisition;
- realisation time and cost effectiveness,

an innovative optic fibre-based sensor was designed and fiercely tested, varying injection pressure, backpressure and energising time. Due to the working principle based on light beam transmission via an optical cable, the optical transducer showed its insensitivity to phenomena traditionally hindering the acquisition of needle displacement. The device is able to follow satisfactorily the control piston displacement both for single injections and for multiple events. From the experimental tests, it also emerged that:

1. backpressure exerts a non-negligible impact on the time history of the needle displacement during the injection event;
2. at a constant injection pressure and energising time, higher backpressures boost needle lift and prolong the hold time;
3. at unvaried injection pressure, an increase in backpressure results in a faster injector closure.

Along with the demonstration of the combined impact exerted by injection pressure with backpressure on the time-history of the needle's motion during the injection event, these findings further testify the reliability of the proposed technique. Therefore, the novel sensor is an ideal mass producible tool, which might supersede the currently available devices. However, since the scope of the experimental work primarily involved laboratory investigation, the issues related to the installation on the injector and the subsequent enlargement of the injection system equipment were not taken into consideration. In this respect, the final goal may be the on-board real-time control of a diesel injector. Explorations of the feasibility of this measurement are worthy of further analysis, which is the forthcoming target of this research activity.

CHAPTER 3

EXPERIMENTAL INVESTIGATION OF THE HOLE-TO-HOLE NON-UNIFORMITY OF JET VELOCITIES IN A DIESEL INJECTOR

Results from Chapter 3 have been published in Fuel, an Elsevier journal:

Coratella, C., Sahu, A., Parry, L., Xu, H., and Ma, X. (2020), 'Experimental investigation of the orifice-to-orifice variability in jet velocities in a diesel injector', *Fuel*, 280, (118353).

This work has here been amended and reproduced with the permission of all co-authors.

Introduction

A wide range of scientific literature has proved that engine efficiency is adversely affected by the orifice-to-orifice variability in fuel jets' velocities. Despite several studies dealing with hole-to-hole variability in jet velocities, the reasons behind this phenomenon are still far from being fully understood. This knowledge gap has motivated the study described in this chapter, which provides evidence of the impact exerted by injection settings on needle wobbles, responsible for the orifice-to-orifice variability in jet velocities. From the experimental investigation, it emerged that an increase in backpressure, along with greater injection pressure, minimises the non-uniformity of the jets' development. The chapter describes the research activity and emphasises the key role of backpressure, combined with injection pressure, in the uniformity of jets' development. The study includes also an assessment of injection delay, referring to each of the fuel plumes exiting the multi-hole injector.

3.1 Literature review

Nowadays, the CR system is characterised by the *MultiJet* technology, consisting of split injections, timing and duration, which are set by the ECU according to the sensors' output. The wide-ranging application of this technology is mainly due to the flexibility and fast response of the injection system components. The faster injector actuations enable the injection cycle to be split up into eight separate shots, improving appreciably the accuracy of the injected fuel amount, to the benefit of combustion efficiency. On the other hand, the fast dynamics of CR hydraulic components engender sensible pressure perturbations, which determine the non-uniformity of the jets' development. Orifice-to-orifice non-uniformity in jets' velocities results in the imbalance of the injected fuel rate, underlying uneven A/F ratio spatial distribution, which in turn affects adversely the combustion efficiency. A vast amount of literature has singled out needle wobbles, cavitation onset and injector ageing as the main factors responsible for the orifice-to-orifice non-uniformity of jets' velocity.

3.1.1 The impact of needle wobbles on the imbalance of injected fuel rate

Needle off-axis motion is characterised by a high degree of randomness, **(64, 81-87)** unlike the axial motion, detection of which shows high repeatability. **(73-74)** This underlies the unbalanced injected flow rate, which is estimable according to the principles of fluid dynamics. **(87, 88)** Volumetric flow rate q_E of a quasi-steady viscous flow through the eccentric annular gap is indeed achievable as follows:

$$q_E = q_C \cdot \left(1 + \varepsilon^2\right) \tag{3.1}$$

where q_C is the volumetric flow rate when the annular gap between the needle and internal nozzle walls is concentric; ε stands for the ratio of *e*, referring to eccentric distance between the needle centre and the injector axis; with *d*, namely the clearance of the annular gap (Figure 3.1).

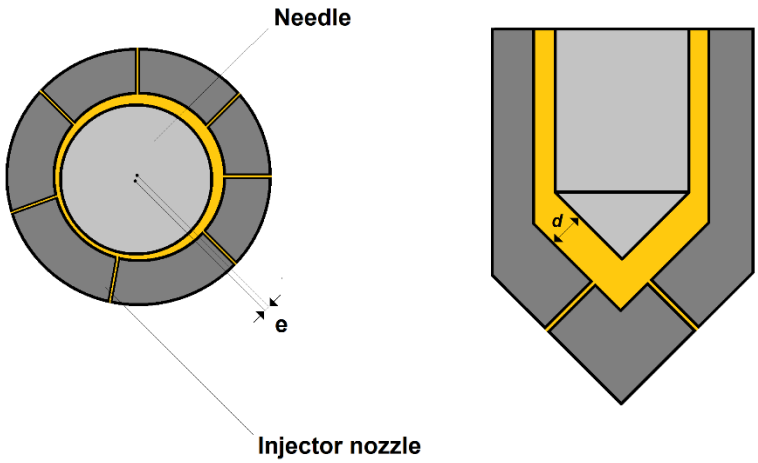


Figure 3.1. The flow rate q_E through the eccentric annular gap differs from the flow rate q_C when the gap is concentric

In this regard, a wide range of literature has proved that, at commencing the injection, radial motion was estimated at less than two hundredths of a millimetre. More specifically, Zhang *et al.* found that, for an injection pressure of 1000 bar, wobbles are estimable at around 14 μm for needle lifts lower than 200 μm. **(86)** Tests revealed that the needle reached this lift at approximately 250 μs ASOI time; whilst, needle wobbles were found to be estimable at around 8 μm for higher lifts.

A breakthrough in the comprehension of the orifice-to-orifice variation was provided by Mitroglou *et al.* **(89)** via a high-speed imaging technique. They found that the needle's eccentric motion governs the orifice-to-orifice variation, which is also affected by the onset of cavitation initiating at the orifice exit.

Torelli *et al.* achieved a reconstruction of the 3D needle motion profiles over a temporal series of sequential injection events by means of X-ray tomography. This approach revealed the relationship between hole-to-hole variability and needle motion. **(90)** Furthermore, Torelli *et al.* performed a CFD simulation demonstrating large orifice-to-orifice variability over the initial stages of the injection event, due to the needle's radial motion. **(91, 92)** They found also that during the initial phase of the injection, jet-shaped structures arise where the gap between the seat and the needle is larger.

Chiavola *et al.* performed a numerical investigation, highlighting the influence of needle vibration on the flow velocity field and cavitation inception. **(64, 82)** It was found that the lowest flow velocities take place through the hole positioned in the closest vicinity to the needle.

Chiatti *et al.* investigated the impact of needle off-axis motion on the outer spray in a multi-hole VCO injector. **(83, 84)** The main finding was the similarity of discharge coefficients among the holes.

While Palmieri *et al.* demonstrated the high sensitivity of the flow pattern to off-axis needle displacement, causing non-uniform jet development and imbalances of flow rate. **(85)** More specifically, the mutual position of nozzle holes with the needle axis significantly influenced both the flow rate distribution among the orifices and the onset of cavitation.

Huang *et al.* proved that both injection pressure and the number of injector holes considerably affect the amplitude of the eccentric needle motion. **(87)** Similar findings were achieved by Magnotti *et al.* **(93)** By means of X-ray tomography exposing a groove along the length of the injector hole and an eccentric nozzle outlet profile, they identified irregularities of the internal nozzle geometry as a further potential factor contributing to the non-uniformity of spray.

In addition, Powell *et al.* conducted a numerical investigation employing 3D grids representing the nozzle geometry of a single-hole injector at various needle lifts. **(94)** It was observed that needle off-axis motion determines significantly the flow pattern in the sac.

Moreover, Najafi *et al.* carried out a numerical investigation on the crucial role of the injector on the spray characteristics, which determine the combustion stability. **(95)** The main finding was the demonstration of the strong correlation between unbalanced distribution of fuel jets' velocity and uneven spray development.

Duke *et al.* provided a further insight into the impact exerted by transients in the needle motion and small-scale features of the injector's internal geometry on the variations in the mass flow rate. **(96)** Via techniques ranging from X-ray to visible-light diagnostics, they found that mass flow rate variations affect the large-scale asymmetries in the spray structure. Likewise, Battistoni *et al.* carried out numerical investigations of the inner nozzle flow in a five-hole mini-SAC diesel injector in fully 3D turbulent transient conditions. **(81)** As mentioned above, injector ageing also exerts a substantial impact on the spray development uniformity. In this respect, Pos et *al*. demonstrated via a high-speed imaging technique that used injectors are prone to wear and deposit formation; which worsens the uniformity of the spray's development and the resulting combustible mixture preparation as well. **(97)**

The reviewed literature agrees in deeming the needle off-axis motion, cavitation onset and carbonaceous deposits within the holes as the main factors governing the unbalanced spray development. Nonetheless, the reasons underlying this phenomenon are still far from being fully understood. This chapter thereby aims to provide a new insight into the physical principles governing the hole-to-hole variability in jets' velocities.

3.2. The proposed approach

In order to provide an experimental framework to assess the variability of jets' velocities at early stages of the injection event, a comprehensive investigation was conducted under various injection scenarios. More specifically, following the acquisition of images referring to jet plumes via a high-speed camera, injection pressure and backpressure were singled out as the key factors determining the needle oscillations. Afterwards, a statistical analysis of the jet plumes' velocities at the early stages of the injection event was carried out. The study includes also an assessment of the delay of injection (DOI) related to each of the fuel plumes exiting the multi-hole injector. The assessment of this parameter, which is linked to the

appearance of the fuel plumes' tips, is indeed deemed indicative of the simultaneity of jets exiting the multi-hole injector.

The outline of this chapter is as follows. Sections 3.3 and 3.4 describe the experimental system and methodology, respectively. The experimental campaign and analysis of the results are fully discussed in sections 3.5 and 3.6. Section 3.7 provides a physical interpretation of the results. Conclusions are summarised in section 3.8.

3.3. Experimental set-up

Figure 3.2 sketches the experimental set-up employed for this stage of the project.

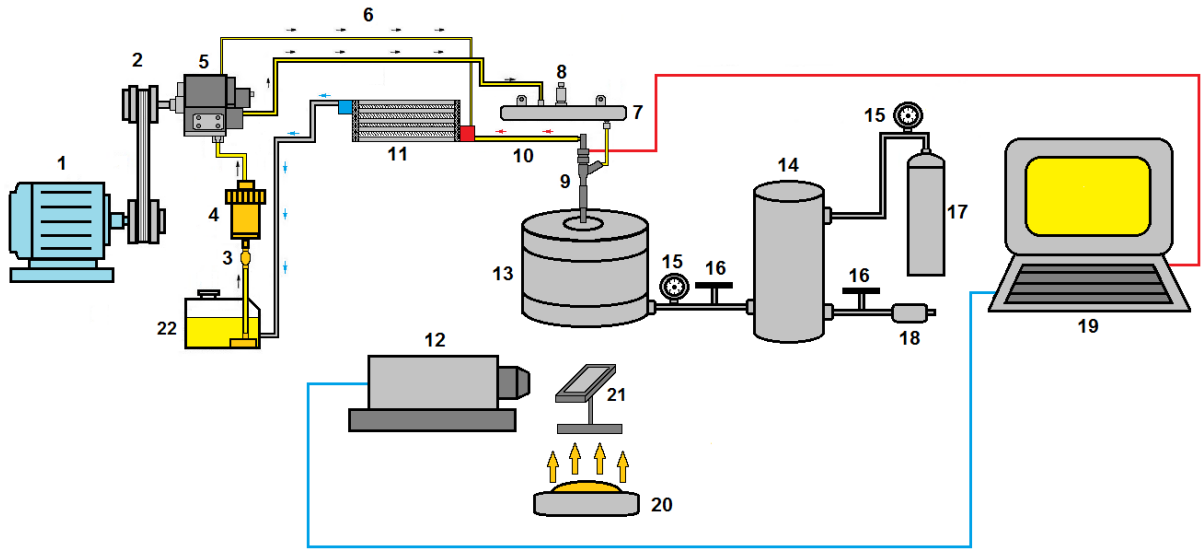


Figure 3.2. Test rig: 1 - Electric engine; 2 - Transmission belt; 3 - Fuel filter; 4 - Low-pressure pump; 5 - High-pressure pump; 6 - High-pressure line; 7 - Rail; 8 - Pressure regulating valve; 9 - Injector; 10 - Backflow fuel line; 11 - Heat exchanger; 12 - High-speed camera; 13 - High-pressure vessel; 14 - Pressurised nitrogen chamber; 15 - Manometers; 16 - Pressure regulator valves; 17 - Pressurised nitrogen bottle; 18 - Relief valve; 19 - Computer; 20 - Halogen bulb; 21 - Mirror; 22 - Fuel tank

Apart from the high-speed camera for the acquisition of the fuel jet plumes, the set-up does not differ from the one for the assessment of the needle lift sensor.

3.3.1. High-pressure vessel (HPV)

Diesel is injected into a quiescent nitrogen ambiance within a high-pressure vessel (HPV). Three quartz windows of 58-mm diameters, enable the fuel plumes' visualisation. The HPV is

provided with a gas inlet and outlet, which are controlled via manual ball valves. The chamber has a regulating valve, which allows the nitrogen to be stored at a maximum pressure of 110 bar.

3.3.2. The imaging set-up

An ultra-high-speed camera *SpeedSense 9000,* manufactured by *DantecDynamics,* was used to record the fuel plumes' development. The camera speed and aperture time was set at 25000 fps at a resolution of 512 x 512 pixels and 19 μs, respectively. Thus, the images were acquired every 40 μs, enabling an accurate acquisition of the temporal development of the jets' plumes. Particular attention was paid to coordinate the injection trigger with the camera timing. This stage is essential to capture the fuel plumes' development. In order to illuminate the fuel plumes, a backlight was used. A halogen bulb, supplied with DC power, was positioned below the HPV, to illuminate the plumes from the bottom. A mirror enabled the visualisation of the plumes from underneath.

More specifically, the mirror was positioned above the halogen lamp. However, the visualisation of the plumes was not hindered, given the small size of the mirror and its mutual position with the HPV and the halogen bulb.

3.3.3. The image processing

Figure 3.3 shows the sequence of the image processing technique employed in this study.

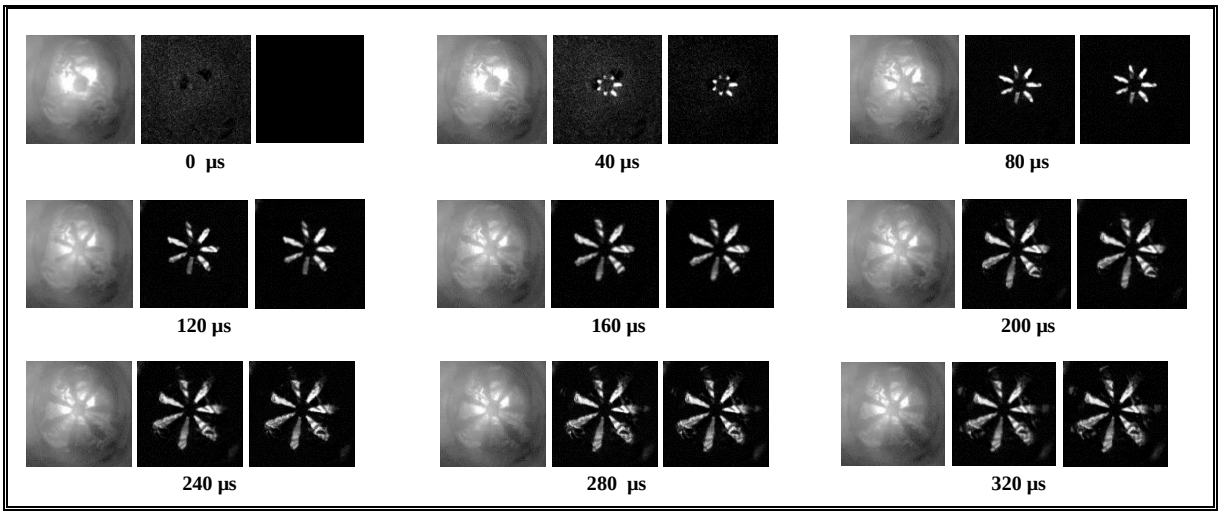


Figure 3.3. The fuel plumes' image processing via an in-house developed MATLAB script and time-stamps (p_{INJ} = 1400 bar, BP = 20 bar)

Once the fuel plumes' development was captured by the high-speed camera, an in-house developed MATLAB code enabled the image processing. **(43, 98, 99)** The background was then removed, and a filter subtracted the remaining white noise speckles, so as to enhance the contrast. Finally, the image presented a satisfactory clearness. Figure 3.4 shows the overall processing, the last stage of which consists of binarizing the fuel plumes' image.

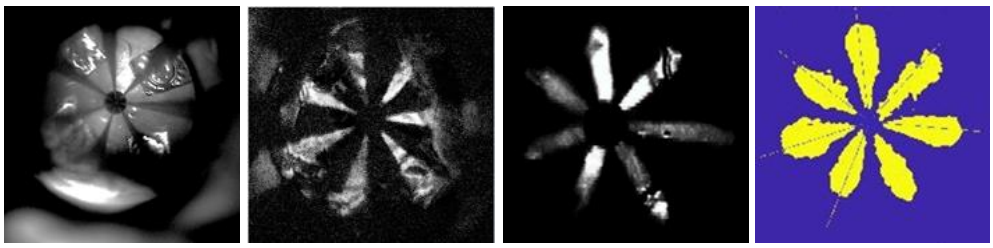


Figure 3.4. The fuel plumes' image processing via an in-house developed MATLAB script (ASOI = 480 µs, p_{INJ} = 1400 bar, BP = 20 bar)

Then, the plumes' lengths were calculated through the number of pixels between the hole outlet and the maximum radial distance covered by the plumes' tips. As well as the jets' plumes, the fuel jet angle may also be acquired. Therefore, it would be worthy of interest to assess the combined impact of injection settings with the fuel properties on the jet angle at the orifice outlet. However, for the sake of brevity, an investigation of the fuel jet angle is not included among the objectives of this research activity.

3.4. Methodology for the analysis of the hole-to-hole non-uniformity of diesel jets' velocities

This section provides a detailed study of the non-uniformity of the fuel plumes' velocity under various injection conditions. The instantaneous velocity of fuel plumes' tips is calculated from the plumes' length using the following equation:

$$U \approx \frac{\Delta PL}{\Delta t} \tag{3.2}$$

where U, PL and Δt represent the velocity of the fuel jets' plumes, the plume length and the time interval, respectively. The time interval was set to equal 40 μs, namely the frame rate. Since this study focuses on the early stages of injection, the velocities of the jets' plumes are calculated at 40 μs after the start of injection. The standard deviation of the plumes' velocities is then calculated to indicate the degree of uniformity during the initial stage. At each injection scenario, the standard deviation was calculated as follows:

$$\sigma = \sqrt{\frac{1}{N} \cdot \sum_{i=1}^{7} (u_i - \bar{u})^2} \tag{3.3}$$

with σ, u_i, $\bar{u}$ and N being the standard deviation, fuel plume's velocity exiting the *i-th* hole, fuel mean velocity and number of fuel jets' plumes, respectively. Accordingly, a low standard deviation indicates that the velocities tend to be spread out over a small range; whilst a higher standard deviation stands for a wider variation of jet plumes' velocities. In this way, an estimate of the uniformity of fuel plumes' velocity is provided. This study focuses on the early stages of injection, when jets' velocities are spanned out over a greater range in comparison with the rest of the injection process. Indeed, the velocities and their variations tend to reduce over the injection event, given the prevailing action of backpressure on the fuel jet. As a consequence, fuel kinetic energy decays.

3.5. Experimental tests

In the wake of the findings emerging from sensor testing, and because of the imbalance of the injected flow affected by needle lift, an experimental campaign was undertaken to assess the non-uniformity of the jets' velocities. Indeed, the observations reviewed in Chapter 1 serve as a baseline for the tests described here and the related discussion.

3.5.1. Tests conditions

The tests were performed at injection scenarios listed in Table 3.1. The energising time was set at 2000 μs.

Table 3.1. Injection pressures and backpressures determining the tests conditions

Injection pressure (bar)	400	700	1000	1400
Backpressure (bar)	20	40	60	80

The injection configurations were set to keep consistency with the experimental tests for the assessment of the needle lift sensor. Moreover, injection pressure and backpressure were set also on the basis of the studies investigating the imbalance of the internal fuel flow determined by needle off-axis motion. **(43, 64, 81-87, 90-94, 98)** The following table lists the injection scenarios set by the authors of papers pertaining to the assessment of needle off-axis motion (Table 3.2).

Table 3.2. Injection settings set by authors of papers pertaining to the assessment of needle radial motion

Reference	*Injection pressure (bar)*	*Backpressure (bar)*
1	780	20
2	1100	Not specified
3	1000	7
4	1400	1
4 (*)	1500	60
5	1000, 2000	30
6	1000	40
7	1350, 1600, 2000	1
8	300, 1000	1
14	1000, 1500, 2000	100
15	1000	100
16	1000, 1500, 2000	100
18	1000	20
22	350, 750	1, 40
23	400, 600, 750, 900, 1050, 1200	1, 10, 15, 30
25	400, 700, 1000, 1400	20, 40, 60, 80

Moreover, the backpressure set here is justified by the observations when referring to charts plotting the in-cylinder pressure in a diesel engine. **(100)** Table 3.3 lists the highest in-cylinder pressure therein at various rotational speeds.

Table 3.3. The highest in-cylinder pressure detected in a diesel engine at various rotational speeds

Maximum in-cylinder pressure (bar)	84.0	84.0	≈80	≈80	≈80	≈77	72.82
Rotational speed (RPM)	1000	1500	2000	2500	3000	3500	4000

3.5.2. Diesel properties

Table 3.4 describes the physical properties of the diesel employed for the tests. **(101-104)**

Table 3.4. Properties of the employed diesel

Ambient temperature (°C)	20
Fuel temperature (°C)	45
Fuel density (kg/m^3)	814
Kinematic viscosity (mm^2/s)	1.5033
Vapour pressure (kPa)	81
Surface tension (N/m)	$27.76 \cdot 10^{-3}$

As shown by Table 3.4, the fuel properties refer to the reported temperature, which was kept at around 45 ˚C. For the calculation of viscosity, the equation reported in the reference was employed. **(101)** Also, the density was estimated according to the equation correlating the diesel density with temperature. In this regard, the author based the calculations on the findings emerging from the research activity carried out by Armas *et al.* **(102)** The diesel temperature set here falls within the range 298-350 K. Keeping in mind this range, the formula:

$$\rho_{DIESEL} = 1061.5 - 0.7171 \cdot T\,(K) \tag{3.4}$$

enables the estimation of diesel density. With regard to the estimation of the vapour pressure and the surface tension, it was based on the findings from the references **(103)** and **(104)**, respectively.

3.5.3. The time development of the diesel plumes' length

Figure 3.5 depicts the time-history of the PLs referring to each hole and averaged over five consecutive shots.

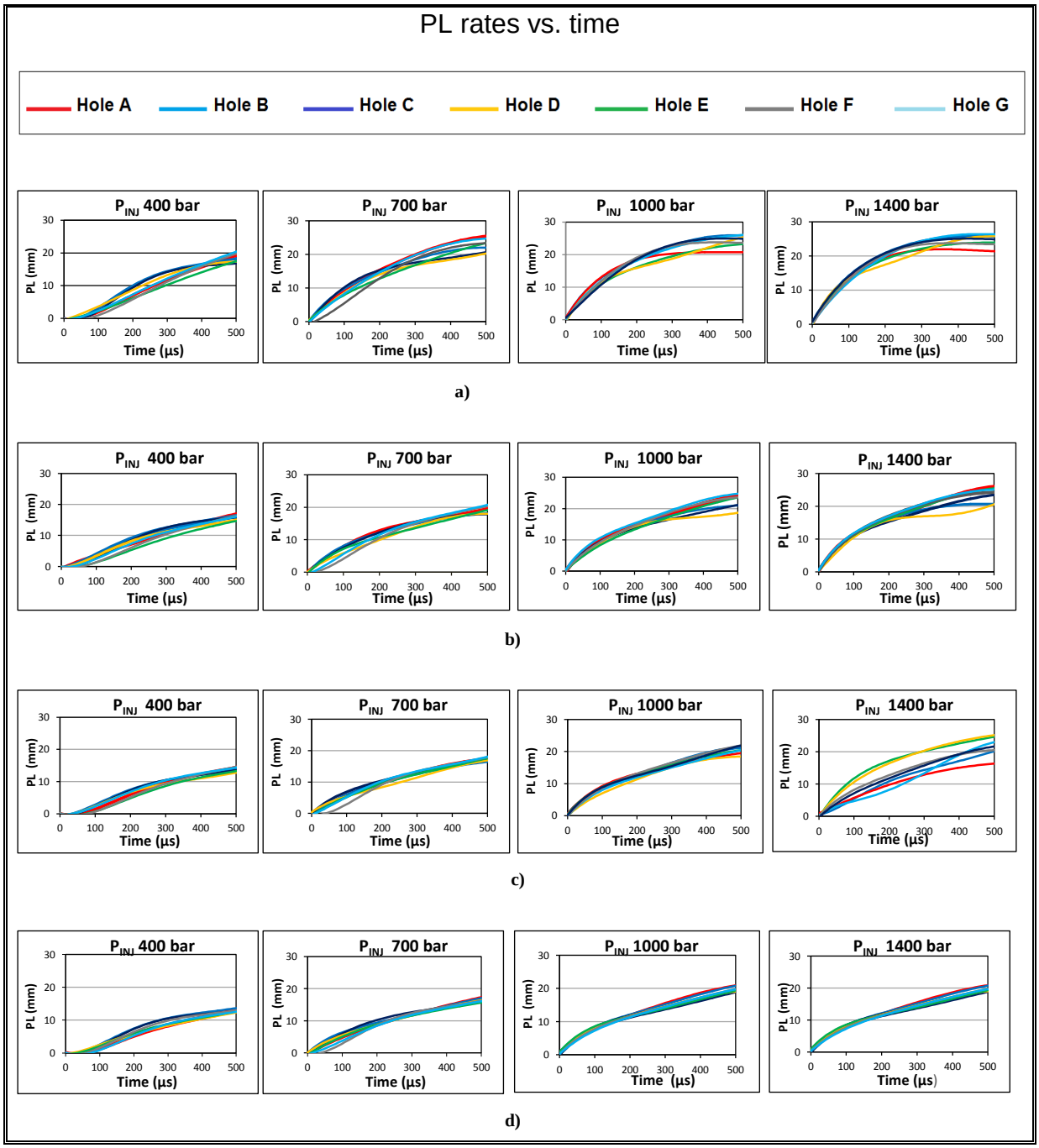


Figure 3.5. The temporal PL developments related to each of seven holes and averaged over five injection shots, acquired at various injection pressures and backpressure of 20 bar (a), 40 bar (b), 60 bar (c) and 80 bar (d)

As expected, shots at higher injection pressure and lower backpressure exhibit steeper slopes of curves, indicating faster plumes. It should also be noted that, at constant backpressure, the spread among the curves is considerable at low injection pressures with respect to high injection pressure cases. By contrast, at constant injection pressures, increasing backpressure

results in a higher degree of superimposition of curves, indicating an improved uniformity of the jets' development.

3.5.3.1. Overlapping of PL curves at a backpressure of 20 bar

For the injection performed at a backpressure of 20 bar, a consistent trend to superimposition is not observed at an injection pressure of 400 bar. At an injection pressure of 700 bar, except for hole F, a significant overlapping is observable till 80 μs. At injection pressure of 1000 bar, curves reveal a significant superimposition until 110 μs after the start of injection. As injection pressure is set at 1400 bar, a considerable superimposition is observable till 140 μs.

3.5.3.2. Overlapping of PL curves at a backpressure of 40 bar

At a backpressure of 40 bar, a more remarkable overlapping emerges. At an injection pressure of 400 bar, curves exhibit a greater superimposition, unlike injection performed at the same injection pressure and backpressure of 20 bar. At an injection pressure of 700 bar, curves reveal an appreciable trend to superimposition till 130 μs, except for holes D, F and G. However, curves referring to the said holes do not reveal a significant distance from other curves. Afterwards, curves resume to be fairly superimposed till 450 μs of ASOI time. At an injection pressure of 1000 bar, there is a more observable trend of superimposition till 300 μs curves are observed. At an injection pressure of 1400 bar, any difference from the previous injection is not seen in terms of a mutual distance among the curves.

3.5.3.3. Overlapping of PL curves at a backpressure of 60 bar

With regard to injections performed at 60 bar of backpressure, overlapping curves are observed at each injection pressure; particularly, once injection pressure is set at 1000 bar, the overlapping is observable till 450 μs. Afterwards, jets exiting holes A and D tend to diverge. At an injection pressure of 1400 bar, curves tend to diverge at 50 μs. However, the jets exiting holes D and E exhibit higher PL in comparison with the injections managed at 1000 bar of injection pressure.

3.5.3.3.1. The inconsistency referring to the 1400-60 bar case

From the chart referring to injection performed at 1400 bar-60 bar, it emerges that this injection setting does not output a much higher degree of overlapping between curves. As the low overlapping between curves is indicative of a lower orifice-to-orifice variability, this might appear an inconsistency ascribable to the employed statistic approach. Nevertheless, the scarce overlapping can be seen on the following charts plotting the jet penetration lengths exiting the injector holes and referring to the single main injection shots, prior to be statistically analysed (Figure 3.6).

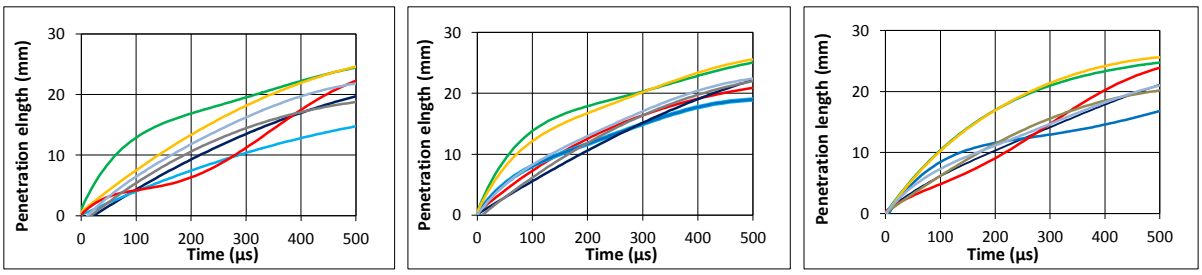


Figure 3.6. The time-histories of PL exiting the holes. The charts refer to three single main injections before the statistical analysis

Accordingly, the inconsistency might be due to the low overlapping emerging from the single main injection performed at an injection pressure and backpressure of 1400 bar and 60 bar, respectively.

However, further injections were performed at this injection setting. As shown in Figure 3.7, the time-histories of jet penetration lengths exhibit a good degree of overlapping.

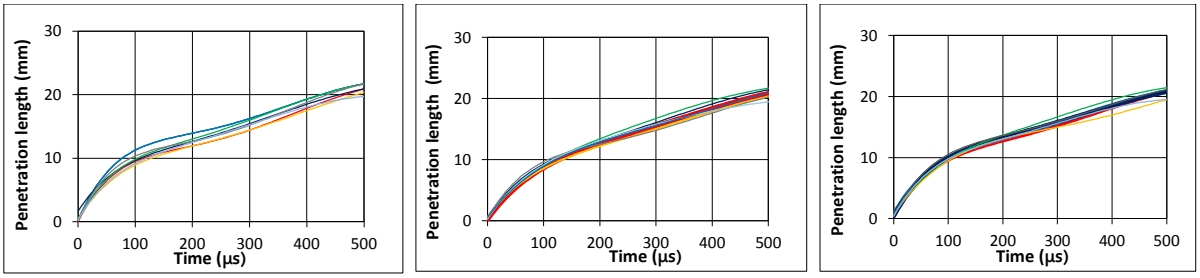


Figure 3.7. The PL time-histories referring to single injections performed at p_{INJ} = 1400 bar and BP = 60 bar, and not included in the statistical analysis

This represents a discrepancy with the main injections performed at the same injection setting. A further reason underlying the scarce overlapping might be that the injections were performed consecutively. Indeed, consecutive shots are prone to engender considerable injection-induced pressure fluctuations within the rail. These dynamics effects, attributable to needle lift, consist of pressure waves travelling between the rail and injector nozzle. As a result, appreciable variations of rail pressure ensue. In this regard, Chapter 5 provides an insight into rail pressure fluctuations, which were found to vary with:

- injection pressure;
- backpressure;
- fuel properties.

Indeed, it emerged that this phenomenon is accentuated in the case of fuel provided with a lower bulk modulus, such as diesel, if compared to biofuels. This implies that at commencing injection, rail pressure is likely to be lower than the set pressure, worsening the uniformity of the jets' velocities. Therefore, consecutive injections might lead to unexpected time developments with the fuel jets.

3.5.3.4. Overlapping of PL curves at a backpressure of 80 bar

Tests also revealed that, at an unvaried injection pressure, 80 bar is the backpressure value showing the largest fuel jet uniformity. Mutual closeness among curves is more significant in comparison with injections performed at the previous backpressures. The graphs may suggest that decreasing both injection pressure and backpressure accentuate the unevenness of the plumes' length. Furthermore, an increase in backpressure is found to determine a longer injection delay. This phenomenon is significantly greater at low injection pressures, namely 400 bar and 700 bar.

3.5.4. The injection delays of the diesel plumes

The investigation of the orifice-to-orifice variability of jet plumes' velocities included the assessment of the DOI, referring to each of the fuel plumes exiting the injector orifices. This parameter is strongly linked with the timing of the plumes' tips detection, providing a deeper insight into the simultaneity of the jets. The following tables show the DOI characterising the shots exiting each orifice at the set injection scenarios. The last two rows refer to the averages and standard deviations calculated over the DOI related to each hole (Tables 3.5-3.8).

Table 3.5. DOI (in μs) detected at various injection pressures and a backpressure of 20 bar

		400 bar – 20 bar					700 bar – 20 bar					1000 bar – 20 bar					1400 bar – 20 bar				
A hole	120	80	80	120	120	80	0	0	0	0	0	0	0	0	0	0	0	0	0	0	0
B hole	80	80	80	120	120	40	0	0	40	0	0	0	0	0	40	0	0	0	0	0	0
C hole	80	80	80	120	160	40	0	0	40	0	0	0	0	0	0	0	0	0	0	0	0
D hole	80	40	40	80	80	0	0	0	0	0	0	0	0	0	0	0	0	0	0	0	0
E hole	80	80	80	80	80	40	40	0	0	40	0	0	0	0	0	0	0	0	0	0	0
F hole	120	120	120	40	120	80	40	40	0	40	0	0	0	0	0	0	0	0	0	0	0
G hole	120	80	80	80	80	40	40	0	0	40	0	0	0	0	0	0	0	0	0	0	0
Average	97.1	80	80	91.4	108.6	45.7	17.1	5.7	11.4	17.1	0	0	0	0	5.71	0	0	0	0	0	0
St. Dev.	21.4	23.1	23.1	30.2	30.2	27.6	21.4	15.1	19.5	21.4	0	0	0	0	15.1	0	0	0	0	0	0
Error	20	40	40	40	40	40	20	20	20	20	0	0	0	0	20	0	0	0	0	0	0

Table 3.6. DOI (in μs) detected at various injection pressures and a backpressure of 40 bar

	400 bar – 40 bar					700 bar – 40 bar					1000 bar – 40 bar					1400 bar – 40 bar				
A hole	80	40	80	80	80	40	40	40	40	40	40	0	0	0	0	0	0	0	0	0
B hole	80	80	80	80	80	40	80	40	120	80	40	0	0	0	0	0	0	0	0	0
C hole	80	80	80	120	80	40	80	0	40	40	40	0	0	0	0	0	0	0	0	0
D hole	80	80	120	80	80	40	40	0	40	40	40	0	0	0	0	0	0	0	0	0
E hole	120	120	120	80	40	40	80	0	40	40	40	0	0	0	0	0	0	0	0	0
F hole	120	120	80	40	120	80	40	0	40	40	40	0	0	0	0	0	0	0	0	0
G hole	80	80	80	120	80	0	40	0	40	40	40	0	0	0	0	0	0	0	0	0
Average	91.4	85.7	91.4	85.7	80	40	57.1	11.4	51.4	45.7	40	0	0	0	0	0	0	0	0	0
St. Dev.	19.5	27.6	19.5	27.6	23.1	23.1	21.4	19.5	30.2	15.1	0	0	0	0	0	0	0	0	0	0
Error	20	40	20	40	40	40	20	20	40	20	0	0	0	0	0	0	0	0	0	0

Table 3.7. DOI (in μs) detected at various injection pressures and a backpressure of 60 bar

	400 bar – 60 bar					700 bar – 60 bar					1000 bar – 60 bar					1400 bar – 60 bar				
A hole	120	80	120	80	120	40	40	40	40	80	0	0	0	40	0	40	0	0	0	0
B hole	80	120	80	120	120	40	40	40	80	80	0	0	0	40	0	0	0	0	0	0
C hole	80	120	80	120	120	0	0	0	40	40	0	0	0	40	0	0	0	0	0	0
D hole	80	120	80	80	120	0	0	0	40	40	40	0	0	0	0	80	0	0	0	0
E hole	120	120	120	120	80	40	40	40	40	160	40	0	0	0	0	0	0	0	0	0
F hole	160	80	120	160	120	80	80	80	40	80	40	0	0	40	0	80	40	0	0	0
G hole	120	80	80	80	80	40	40	40	80	80	40	0	0	40	0	40	0	0	0	0
Average	108.6	102.9	97.1	108.6	108.6	34.3	34.3	34.3	51.4	80	22.9	0	0	28.6	0	34.3	5.7	0	0	0
St. Dev.	30.2	21.4	21.4	30.2	19.5	27.6	27.6	27.6	19.5	40	21.4	0	0	19.5	0	35.9	15.1	0	0	0
Error	40	20	20	40	20	40	40	40	20	60	20	0	0	20	0	40	20	0	0	0

Table 3.8. DOI (in μs) detected at various injection pressures and a backpressure of 80 bar

	400 bar – 80 bar					700 bar – 80 bar					1000 bar – 80 bar					1400 bar – 80 bar				
A hole	120	120	80	120	40	40	40	40	80	80	0	0	0	0	0	0	0	0	0	0
B hole	80	80	80	120	120	40	0	0	40	40	0	0	0	0	0	0	0	0	0	40
C hole	120	120	80	80	120	40	40	40	40	40	40	0	0	40	40	0	0	0	0	0
D hole	80	80	80	160	120	40	0	0	80	40	0	0	0	0	0	0	0	0	0	0
E hole	80	80	80	80	200	40	40	40	40	40	0	0	0	0	0	0	0	0	0	0
F hole	240	120	80	80	80	80	80	80	40	40	0	0	0	0	0	0	0	0	0	40
G hole	200	160	120	80	40	80	80	40	80	40	40	0	0	40	40	0	0	0	0	0
Average	131.4	108.6	85.7	102.9	102.9	51.4	40	34.3	57.1	45.7	11.4	0	0	11.4	11.4	0	0	0	0	11.4
St. Dev.	64.1	30.2	15.1	31.5	55.9	19.5	32.7	27.6	21.4	15.1	19.5	0	0	19.5	19.5	0	0	0	0	19.5
Error	80	40	20	40	80	20	40	40	20	20	20	0	0	20	20	0	0	0	0	20

The following section provides a detailed explanation of the results.

3.6. Discussion of the results

A comprehensive discussion of the results is provided in this section, which includes an accurate statistical analysis, followed by an explanation of the physical principles underlying the hole-to-hole non-uniformity of diesel jets' velocities and the injection delays.

3.6.1. The assessment of the orifice-to-orifice variability in jet velocities

As previously mentioned, in order to assess the orifice-to-orifice variability in fuel plumes' velocities the standard deviation was calculated, since such a statistic index provides an

estimate of the dispersion of a data set. The standard deviation refers to the variation in the data set given by seven fuel velocities detected at 40 μs of ASOI time, when a relatively larger non-uniformity in the jets' velocity distribution occurs. More specifically, for each of 16 injection settings, five consecutive main injections were performed. The following subsections review the statistical approach employed for the assessment the variability of the jets' velocities.

3.6.1.1. Analysis of the standard deviations

For each of the seven holes the plumes' lengths were averaged over five shots. As a result, for each of the 16-injection configurations, seven time-histories of the averaged PL referring to each orifice were output. Table 3.9 shows the standard deviations calculated at the injection and ambient pressures listed in Table 3.1.

Table 3.9. Standard deviation of fuel plumes' velocities (in m/s)

	400 bar	**700 bar**	**1000 bar**	**1400 bar**
20 bar	47.05	41.55	27.72	22.25
40 bar	42.50	35.29	26.29	16.23
60 bar	52.07	43.67	27.32	18.59
80 bar	47.20	31.18	22.81	9.03

Figure 3.8 shows the surface achieved by interpolating the standard deviations as function of injection pressure and backpressure.

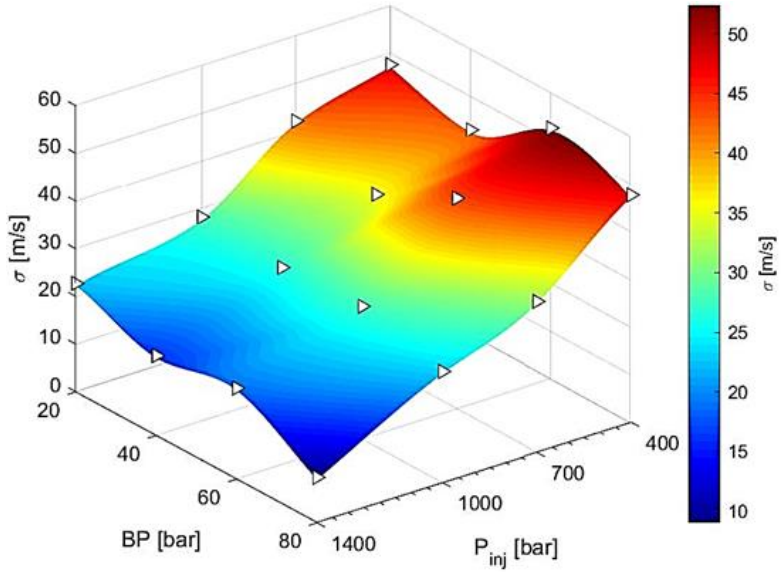


Figure 3.8. The surface plotting the standard deviation of the jets' velocities calculated at the orifice outlet during the early stages of injection

It emerges that increasing injection and ambient pressure result in a decreasing standard deviation, which thus represents improved spray uniformity. At equal backpressure, greater injection pressure implies a reduction in the standard deviation. Particularly, the most abrupt reductions occur at a backpressure of 60 bar and 80 bar. Conversely, the smoothest variations in σ take place at backpressures of 20 bar and 40 bar. At equal injection pressure, the largest standard deviations take place at lower injection pressure, namely 400 bar. At injection pressures of 700 bar and 1000 bar, lower standard deviations are seen. Furthermore, at increasing backpressure, setting an injection pressure of 1400 bar leads to a more considerable reduction in the standard deviation of the jets' velocities. The following bar chart provides a further description of the achieved findings (Figure 3.9).

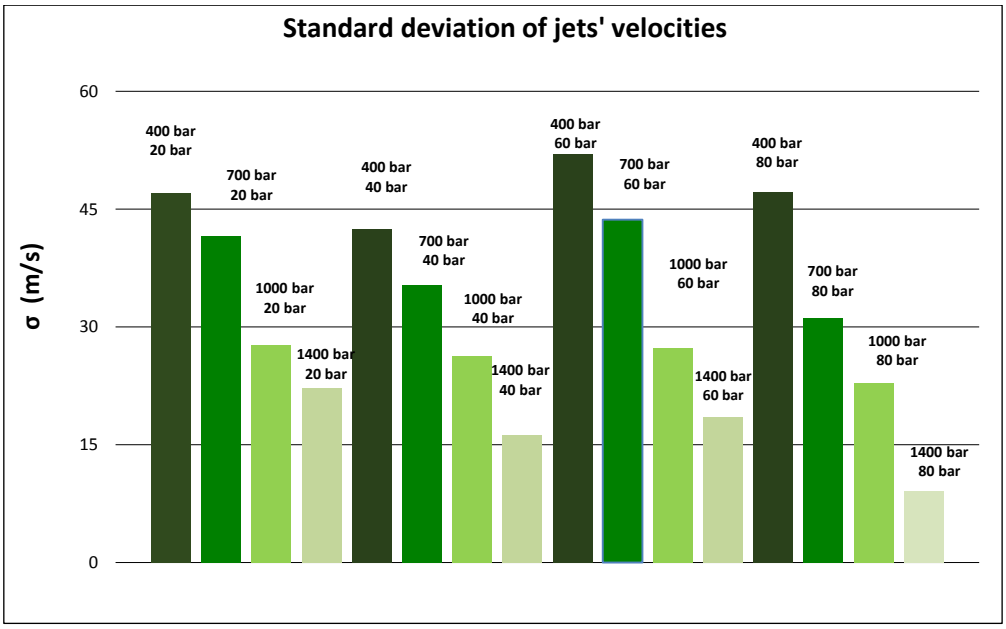


Figure 3.9. The standard deviation of the jets' velocities measured at the outlet of the orifices

Additionally, with an equal constant backpressure, increasing injection pressure is revealed to engender a decreasing trend of the standard deviation. This is meaningful for improving sprays' uniformity and for the smaller range over which the jets' velocities are spread out. It is worth noting that the variability decreases more steeply at a higher backpressure, relative to lower pressures. At a backpressure of 80 bar, injections are characterised by a steep reduction in standard deviation from 47.20 m/s to 9.03 m/s, for injection pressures of 400 bar and 1400 bar, respectively. Such a drop in σ is higher than that characterising injections performed at 20, and 40 bar, where it reduces by 24.8 m/s and 26.3 m/s, respectively for the range of injection pressures. It can be seen that once backpressure is switched from 40 bar to 60 bar and injection pressure is set at 400 bar, fuel velocities are spread out over a slightly wider range. This is meaningful of a slightly worse spray uniformity. Thereafter, once backpressure is set at 80 bar, the standard deviation of the jets' velocities is subjected to an appreciable reduction. A similar trend is seen at the rest of the injection pressures. In particular, an increase in backpressure from 60 bar to 80 bar leads to a steeper drop in the standard deviation of the jets' velocities at injection pressures of 700 bar, 1000 bar and 1400 bar. Moreover, it is worth noting that at backpressures of 60 and 80 bar, an injection pressure of

400 bar outputs a standard deviation larger than those at ambient pressures of 20 bar and 40 bar. This may be attributed to the greater backpressure, which is believed to promote the fuel momentum transfer onto the needle protrusion. Thus, it may be inferred that setting higher injection and ambient pressures is a potential solution to improve the uniformity of the jets' velocities. Table 3.10 lists the standard deviations detected at 200 μs of ASOI.

Table 3.10. Standard deviation of diesel plumes' velocities (in m/s) at 200 μs ASOI

	400 bar	**700 bar**	**1000 bar**	**1400 bar**
20 bar	6.2	21.79	18.09	26.04
40 bar	10.58	12.10	5.58	9.72
60 bar	6.47	11.87	2.52	19.80
80 bar	8.73	5. 90	5.73	9.13

Figure 3.10 illustrates the surface plotting the standard deviation calculated at 200 μs.

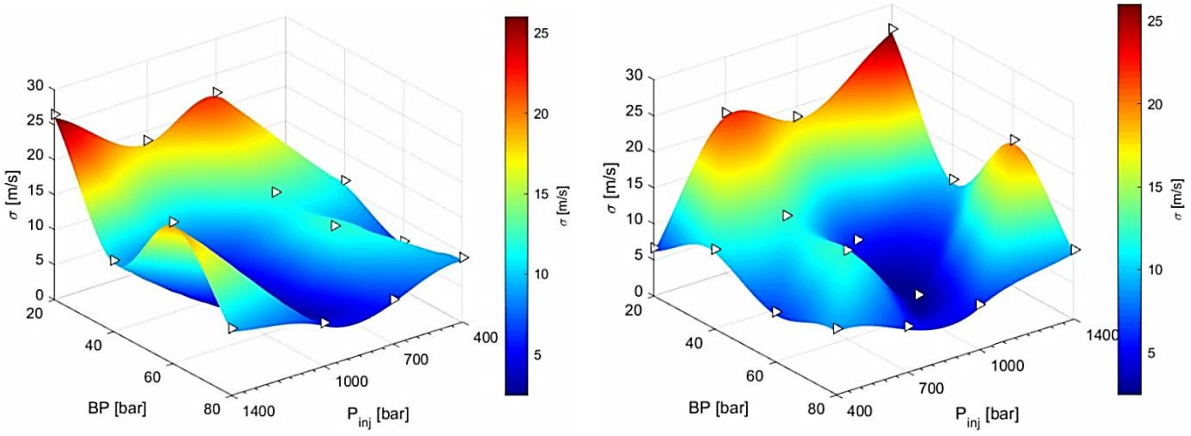


Figure 3.10. Surface plotting standard deviations of velocities at 200 μs after injection start and shown at reverse axis arrangements

Injections at a backpressure of 20 bar and at various injection pressures experience the highest values of standard deviation and the largest variation as well. At a backpressure of 80 bar, increasing injection pressure does not result in a noticeable variability in standard deviation, unlike the rest of the backpressures. However, both standard deviation and its variation are appreciably lower than those observed during the early stages of injection. The reasons underlying this observation are thoroughly discussed in section 3.7. Figure 3.11 illustrates the

temporal variation of the standard deviation of the jets' velocities over the injection event, at above injection and ambient pressures.

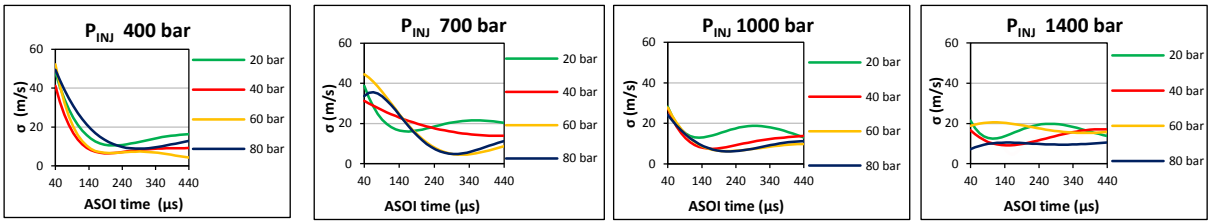


Figure 3.11. The time histories of standard deviations at various injection settings

It emerges that higher injection pressures tend to minimise the standard deviation as well as its variability. Furthermore, the most abrupt variations in standard deviation values lie within the early stages of injection (≈ 120 μs) at any injection pressure. It follows that the orifice-to-orifice variability tends to decrease more gradually, meaning a larger standard deviation with respect to the whole injection event. Afterwards, standard deviations tend to decrease, given the decaying fuel kinetic energy and prevailing action of backpressure, which contrasts the jets and narrows down the velocities' range. This justifies the focus on the early stages of injection (≈ 40 μs of ASOI). Moreover, Table 3.11 shows that the effects benefiting the uniformity of the plumes' velocities are owed to the increase in injection pressure and are indicated by lower standard deviations, which are more observable at greater backpressures. Indeed, the fifth column exhibits an increasing trend of averaged reduction in standard deviation.

Table 3.11. Reductions in σ (in m/s) stemming from switching injection pressure to higher values at constant backpressure

	400 – 700 (bar)	**700 – 1000 (bar)**	**1000 – 1400 (bar)**	**Average of reduction in σ**
20 bar	5.50	13.83	5.47	8.27
40 bar	7.22	8.99	10.06	8.76
60 bar	8.40	16.35	8.72	11.16
80 bar	16.03	8.36	13.79	12.72

At a backpressure of 20 bar, switching injection pressure from 400 bar to 700 bar results in a reduction in standard deviation by approximately 5.50 m/s. Thereafter, switching injection

pressure from 700 bar to 1000 bar and from 1000 bar to 1400 bar leads to approximate reductions in the standard deviation of 13.83 m/s and 5.47 m/s, respectively.

The most dramatic change in standard deviation of the plumes' velocities is observed at a backpressure of 80 bar. It can be seen that at a backpressure of 80 bar, switching the injection pressure to greater values determines an averaged reduction in standard deviation by ~ 12.72 m/s; whilst, switching the injection pressure at a backpressure of 20 bar results in an average reduction by 8.27 m/s.

Therefore, it could be stated that the jets' velocities are prone to a greater uniformity if injections are performed at a higher backpressure. By contrast, lower backpressure minimises the benefiting impact of an increase in injection pressure on the plumes' uniformity, generating smaller reductions in standard deviation. Figure 3.12 depicts the trend of the average reduction in standard deviation, namely ($\sigma_i - \sigma_j$), where *i* and *j* refers to configurations set at various injection pressures and a constant backpressure. The averaged reduction is plotted as a function of backpressure and variation in injection pressure.

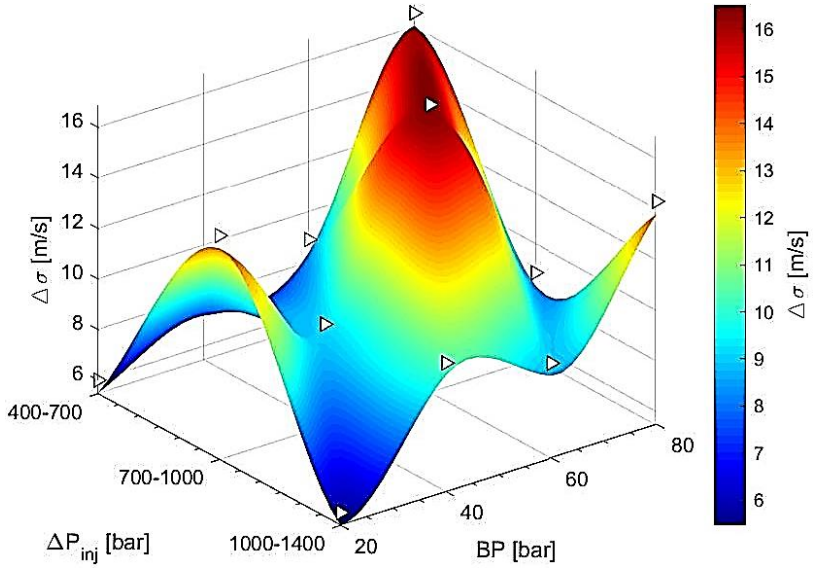


Figure 3.12. Trend of averaged reduction in standard deviation referring to injections performed at constant ambient pressure and different injection pressures

Greater backpressures are seen to determine a higher reduction in standard deviation. By contrast, lower reductions in standard deviation are observed at 20 bar, particularly when injection pressure varies from 400 bar to 700 bar and from 1000 bar to 1400 bar.

3.6.1.2. Analysis according to alternative statistical approach

Similar conclusions were drawn employing a different statistical approach, based on the calculation of standard deviation averaged over five consecutive main injections. Namely, once the injection was performed, the standard deviation over the seven plumes' velocities was calculated. This was applied also for the following four main injections. Thereafter, the average of the standard deviation was calculated over the five injections. Table 3.12 lists the averaged standard deviations related to each of 16 injection scenarios.

Table 3.12. The standard deviations of diesel plumes' velocities (in m/s) if calculated via the alternative statistical approach

	400 bar	**700 bar**	**1000 bar**	**1400 bar**
20 bar	52.03	48.69	32.78	29.83
40 bar	58.73	54.37	13.67	17.28
60 bar	52.14	40.59	35.70	22.82
80 bar	53.27	50.08	25.32	12.92

Figure 3.13 illustrates the bar charts showing the trend of the averaged standard deviations.

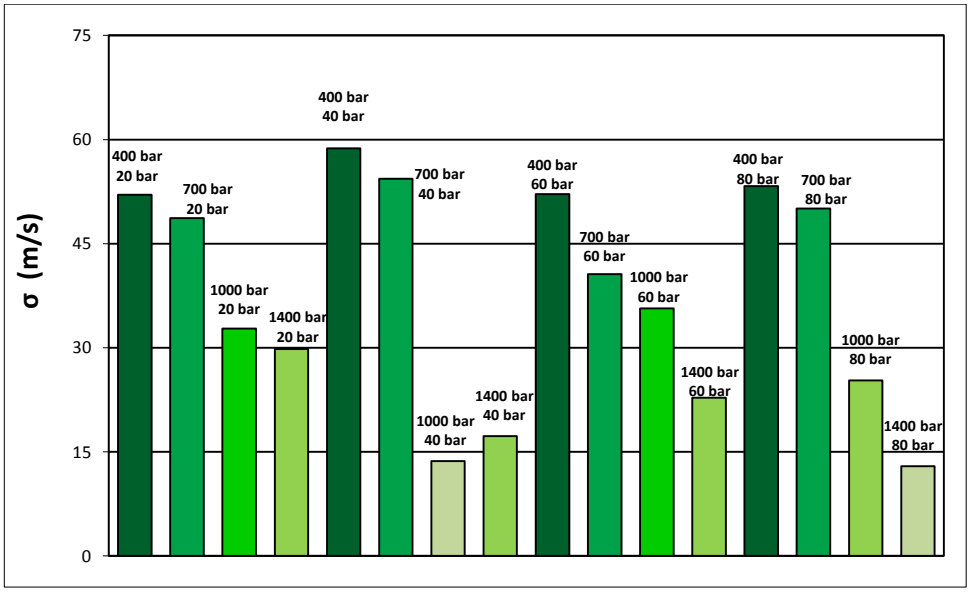


Figure 3.13. The trend of the average of the standard deviations of jets' velocities if calculated via the alternative approach

These results enable the calculation of the variations in the standard deviation stemming from switching injection pressure to higher values at a constant backpressure (Table 3.13).

Table 3.13. The variations in σ (in m/s) due to switching injection pressure to higher values

	400 - 700 (bar)	**700 - 1000 (bar)**	**1000 - 1400 bar**	**Average of reduction in σ**
20 bar	3.33	15.91	2.95	7.40
40 bar	4.37	40.70	-3.61	13.82
60 bar	11.55	4.90	12.87	9.77
80 bar	3.19	24.76	12.40	13.45

Tables 3.11 and 3.13 lead us to conclude that jets are prone to a better uniformity of plumes' velocities when the injections are performed at a greater backpressure. The following section provides a detailed explanation of findings, remarking on the non-negligible role of backpressure.

3.6.2. The assessment of averaged DOI

Table 3.14 shows the averages of the values reported in the 8th rows of the Tables 3.5-3.8.

Table 3.14. Averages calculated from the DOI averages (in μs)

	400 bar	**700 bar**	**1000 bar**	**1400 bar**
20 bar	91.4	19.4	1.1	0
40 bar	86.9	41.1	8	0
60 bar	105.1	46.9	10.3	8
80 bar	106.3	45.7	6.9	2.3

As expected, at unvaried backpressure, an increase in injection pressure shortens the DOI, given the greater kinetic energy of the fuel. It can be seen also that at unvaried injection pressure, greater backpressure prolongs the averaged DOI, because of the greater resistance on fuel flow. More specifically, at injection pressures of 400 bar and 700 bar, higher backpressures increase appreciably the averaged DOI. A weaker increasing trend of averaged DOI, due to greater backpressure, is observable at higher injection pressures, namely 1000 bar and 1400 bar. At an injection pressure of 1000 bar, a backpressure of 20 bar results in an averaged DOI of 1.1 μs. Afterwards, backpressures of 40 bar and 60 bar exhibit an averaged DOI of 8 μs and 10.3 μs. Once backpressure is set at 80 bar, the averaged DOI decreases by 3.4 μs. A similar trend is exhibited also when injection pressure is set at 1400 bar, where

switching backpressure from 60 bar to 80 bar shortens the averaged DOI by 5.7 μs. These inconsistencies, observed when switching the backpressure from 60 bar to 80 bar, might be attributable to the boosting action of the increasing backpressure on the needle. In fact, if on the one hand higher backpressure determines stronger resistance contrasting the flow, on the other it is presumed to promote needle lift. Accordingly, a faster needle lift enables fuel to flow more rapidly towards the orifices.

An additional explanation might be stronger frictions arisen as a response of higher injection pressure and backpressure. Indeed, greater injection and backpressure determine the friction, giving rise to significant thermal effects, which reduce the viscosity and surface tension of some local regions of the fluid. This results in a more accentuated velocity gradient of the fluid, causing an advanced appearance of fuel plumes' tips. This hypothesis is supported by the fact that this phenomenon is more observable at higher injection pressures, which promote the arising thermal effects. However, this aspect is worthy of further investigations.

3.6.2.1. The assessment of DOIs' standard deviation

Table 3.15 reports the averaged standard deviations of the DOI, calculated from the values listed in the 9th rows of the tables 3.5-3.8.

Table 3.15. Averaged standard deviations of DOI (in μs)

	400 bar	**700 bar**	**1000 bar**	**1400 bar**
20 bar	25.6	21.0	3.0	0
40 bar	23.5	21.9	0	0
60 bar	24.6	28.5	8.2	10.2
80 bar	39.4	23.3	11.7	3.9

At unvaried backpressure, an increase in injection pressure determines a steep reduction in the averaged standard deviation. This is due to the greater kinetic energy of the fuel, originating from the higher injection pressure. As a consequence, the DOI is spread out over a narrow range. Namely, once the injector is triggered, the jets' plumes are prone to a greater simultaneity in exiting the orifices. However, the trend observable at a backpressure of 60 bar

exhibits a more uneven trend in comparison with the rest of the counter-pressures. At an unvaried injection pressure, an increase in backpressure results in an increasing trend. Similar to the averaged DOI, some inconsistencies are seen. Indeed, at an injection pressure of 400 bar and 1000 bar, switching backpressure from 20 bar to 40 bar implies a reduction in averaged standard deviation from 25.6 m/s to 23.5 m/s and from 3.0 m/s to 0 m/s, respectively. Analogous observations emerge from the cases referring to injection pressures of 700 bar and 1400 bar; where varying counter-pressure from 60 bar to 80 bar causes a reduction from 28.5 m/s to 23.3 m/s and 10.2 m/s to 0 m/s, respectively.

To summarise, it can be argued that higher injection pressures lead to a smaller range over which the DOI is spread out. Namely, at increasing injection pressure, the jets tend to exhibit a greater simultaneity in exiting the orifices. However, a small standard deviation of DOI is not sufficiently meaningful of a better uniformity. In fact, if on the one hand the jets are prone to exit simultaneously the injector orifices, on the other jets' velocities might reveal larger mutual differences. Therefore, despite the narrow range over which the DOIs are spread out, standard deviation of plumes' velocities is more likely to be indicated for a proper statistical analysis of the jets' uniformity.

3.7. The physical principles governing the orifice-to-orifice variability

In the light of the findings discussed in the previous chapter, the physical interpretation of these results can be based on the combined influence of injection pressure with backpressure on needle lift. In physical terms, it is assumed that the momentum $M_{PRESSURISED\ FUEL}$ is subdivided as follows:

$$M_{PRESSURISED\ FUEL} = M_{NEEDLE\ PROTRUSION} + M_{ORIFICE\ INLET} \tag{3.5}$$

with $M_{NEEDLE\ PROTRUSION}$ and $M_{ORIFICE\ INLET}$ being the fuel momentum contributing to needle lift and promoting fuel flow towards the orifices, respectively. The magnitude of these factors

varies mainly with injection pressure and backpressure. The following considerations are based on this assumption.

3.7.1. Hypothesis about the impact of injection settings on needle wobbles

In the light of the Equation 3.5, it can be argued that low backpressure speeds up the flow towards the orifices, at the expense of the momentum potentially transferrable onto the needle. A slower needle lift ensues, **(105)** enhancing the cantilever effect, which gives rise to a larger difference among the effective cross-sectional areas through which the fuel flows. As a consequence, larger orifice-to-orifice variability in the plumes' velocities arises. **(64, 81-87)** Likewise, under constant backpressure, a decrease in injection pressure slows down needle lift, causing wider oscillations. Thereafter, as the needle approaches the highest positions, variability of the fuel plumes decays, since the cantilever-type vibration is weaker at a greater distance from the needle seat. **(64, 81-87)** The faster lift mitigates the effects of needle wobbles, minimising the difference among the areas through which the fuel flows. This is in agreement with the results showing that greater injection pressures minimise the standard deviation.

3.7.2. The impact of injection settings on off-axis motions with respect to needle lift

Given the mechanical constraints and the typical design of the needle, the axial component of the force acting on its protrusion always outweighs the radial force. However, here the presented findings lead to conjecture that the predominance of the needle's axial displacement over the radial force is more meaningful at higher injection pressures. Similarly, axial motion predominates over the radial motion more significantly at higher backpressures, further mitigating the cantilever effect. This may be attributed to the stronger opposing effect on fuel flow towards the orifice exerted by higher backpressure. As mentioned above, the fuel

momentum transferrable onto the needle protrusion is indeed enhanced, causing a faster lift and a more uniform development of the jets' velocities.

Nonetheless, if on the one hand fuel momentum towards the protrusion boosts axial motion, on the other the needle is radially perturbed. In this regard, the magnitude of force determining the needle's radial displacement depends upon the needle geometry (Figure 3.14).

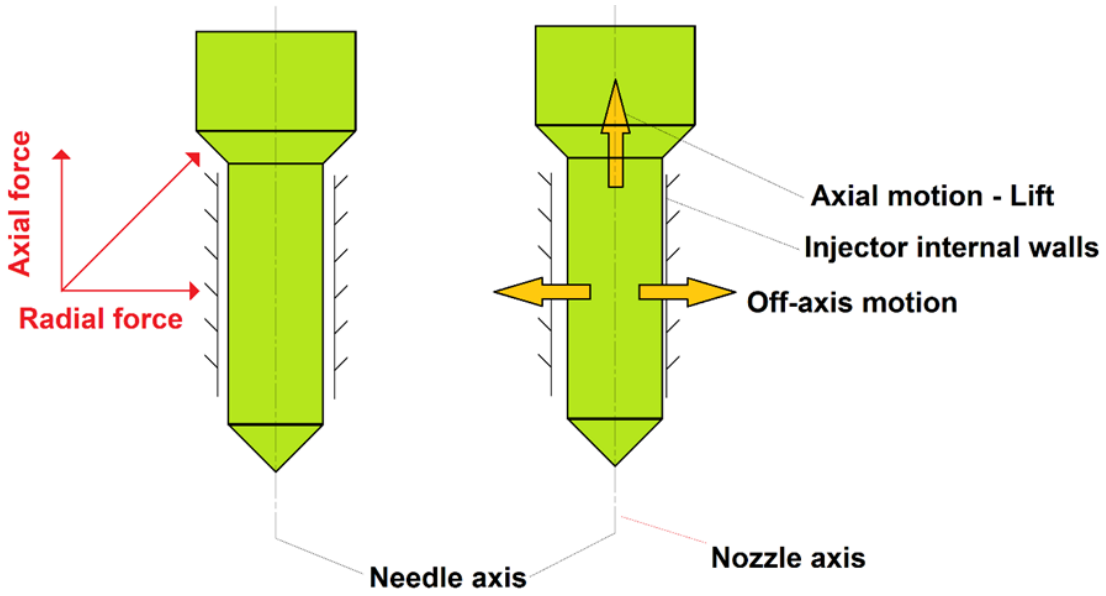


Figure 3.14. The components compounding the force acting on the needle determine the axial and radial motions

These observations may lead to further investigations about the combined impact of the injection settings with the needle geometry on the wobbles underlying the unbalanced internal flow.

3.7.2.1. Needle lift correlated with eccentricity determining the unbalanced diesel flow

The combined impact of higher injection pressure with greater backpressure benefits the needle lift in most of the cases. These considerations can be drawn also in the light of Equation 3.1 and Figure 3.1. Indeed, bearing in mind the Figure 3.1, "*d*" varies over the

needle lift; particularly as the higher needle position is more shortly achievable via setting greater injection pressures and backpressures. Needle lift causes an increase in "*d*", which in turn implies the reduction in ε. This leads to the minimised imbalance of internal fuel flow. It is inferred that eccentricity ε is not constant over the ascending stage of needle motion. It is smaller at the highest needle position.

Figure 3.15 schematises a simplified nozzle of a VCO injector. It can be seen that as the injection starts, fuel flow experiences a changing section, given the ascending motion of the needle.

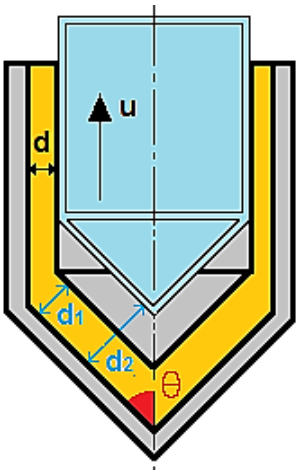


Figure 3.15. Sketch simplifying the typical VCO injector nozzle. The light blue needle refers to the highest position, whilst the grey one stands for the stand-by configuration.

The parameter describing the flow section varies from d to d_1, whilst the gap is given by d_1. Once the needle reaches the maximum lift, the section is described by values of d approaching d_2. Moreover, the following formula:

$$d_i = h_{NEEDLE}\,(t) \cdot sen\theta \tag{3.6}$$

is presumed to synthesise the correlation of the gap between the needle and nozzle internal walls with needle lift. As the needle approaches the maximum position, the gap tends to be larger. This results in increasing d_2, where the higher d_2 indeed minimises the effects of the

varying depth. In the case of the nozzle, the ascending displacement of the needle enables the fluid to flow towards the larger sections, characterised by greater d_i values, from d_1 to d_2. In the light of findings emerging from reference **(88)** d_i tending to d_2 implies a smaller difference between the volumetric flow through an annular gap and the one through an eccentric section. Namely, the increase in d_i, stemming from needle lift, results in a volumetric flow differing slightly more from the case of the needle on-axis position.

3.7.2.2. The impact of injection settings on radial motion

At an injection pressure of 400 bar, varying backpressure from 40 bar to 60 bar is observed to slightly increase the standard deviation. Namely, fuel velocities are spread out over a slightly wider range, worsening the uniformity of the plumes' velocities. This may be ascribable to the action of the higher backpressure. As mentioned above, it exerts a stronger barrier to the flow, promoting the momentum onto the needle. On the other hand, enhancing momentum onto the needle is presumed to contribute moderately to needle misalignment.

Thereafter, once backpressure is set at 80 bar, the standard deviation of the jets' velocities is slightly decreased. Bearing in mind that the momentum's axial component always outweighs the radial component, it is believed to prevail more if compared to the case of backpressure at 60 bar. Therefore, backpressure of 60 bar was found to be a critical value, representing a slight inconsistency. A similar trend is seen at an injection pressure of 700 bar; and in particular at 700 bar, the reduction in the standard deviation of the jets' velocities is more appreciable when switching the backpressure from 60 bar to 80 bar.

For the same reason, the slight inconsistency is observable from the standard deviations calculated at an injection pressure of 400 bar and a backpressure of 60 and 80 bar. These standard deviations are expected to be smaller than those estimated at ambient pressures of 20 bar and 40 bar. However, at backpressures of 60 bar and 80 bar, the standard deviation is

estimated at around 52.07 m/s and 47.20 m/s respectively, relatively higher than the 20-bar and 40-bar cases. This may be still attributable to the impact exerted by the higher backpressure on the needle. Indeed, it might be conceivable that stronger momentum, stemming from higher backpressure, engenders a faster lift as well as a greater radial component of the force on the needle.

3.7.2.3. Discussion of the impact exerted by injection settings on radial motion according to the alternative statistical approach

Analogous observations emerge from the findings' output from the alternative statistical approach. Indeed, at an injection pressure of 400 bar, varying backpressure from 20 bar to 40 bar is observed, increasing the standard deviation from 52.03 m/s to 58.03 m/s. Likewise, increasing the backpressure from 60 bar to 80 bar determines a slight increase in standard deviation from 52.14 m/s to 53.27 m/s. For injections performed at an injection pressure of 700 bar, switching the backpressure from 20 bar to 40 bar determines an increase in averaged standard deviation from 48.69 m/s to 54.37 m/s. Similarly, when the backpressure varies from 60 bar to 80 bar, the standard deviation changes from 40.59 m/s to 50.08 m/s. At an injection pressure of 1000 bar, the only inconsistency is observed when the backpressure is switched from 40 bar to 60 bar, increasing the averaged standard deviation from 13.67 m/s to 35.70 m/s. An injection pressure of 1400 bar exhibits only a discrepancy when the backpressure changes from 40 bar to 60 bar. Indeed, the averaged standard deviation increases from 17.28 m/s to 22.82 m/s. In the light of these observations, regardless of the statistical methodology, switching the backpressure from 40 bar to 60 bar represents an inconsistency, in which the combined impact of the injection pressure with a greater backpressure enhances not only needle lift, but also needle wobbles; affecting adversely the uniformity of the diesel plumes' velocities. This may explain the higher standard deviation of the jets' velocities, indicative of non-uniformity of the fuel plumes.

Nonetheless, Tables 3.13 and 3.15 lead us to conclude that the combined increase in injection pressure with the greater backpressure boosts needle displacement, weakening the adverse effects of needle wobbles on jet uniformity. Hence, diesel plumes' velocities are spread out over a narrower range.

3.8. Summary

This chapter provides a detailed insight into the combined influence of backpressure with injection pressure on the orifice-to-orifice non-uniformity of diesel jets' velocities. In the light of findings emerging from the experimental campaign undertaken to this end, it can be concluded that:

1. at a constant backpressure, an increase in injection pressure minimises the standard deviation of the DOI. As such, the DOI is spread out over a narrow range.
2. However, in spite of the narrow range over which the DOI is spread, the fuel jets' velocities might exhibit a greater mutual difference, indicating a non-uniform jet development.
3. At constant backpressure and increasing injection pressure, the standard deviation of the diesel plumes' velocities is characterised by a decreasing trend, which is indicative of improved jet uniformity.
4. The combined increase in injection pressure with greater backpressure boosts the fuel momentum transferrable onto the needle, giving rise to a faster lift, which alleviates the detrimental impact of needle wobbles on the jet uniformity.
5. If on the one hand higher backpressure is thought to enhance needle lift, on the other it enhances the radial component of the force on the needle.
6. Needle lift always predominates over the off-axis motion more significantly at higher injection pressures and greater backpressures.

7. The beneficial impact of higher injection pressure on the uniformity of the jets' velocities is more considerable if the injections are performed at greater backpressures.

It is worth noting that these findings lie within the pathway followed over the last few decades by engine manufacturers, who have employed economical resources and manpower in order to increase rail pressure. **(39)** However, such a solution increases the energy consumption required by the injection system, so as to prevent leakages and adjust dynamically the maximum pressure according to the engine demands. This framework urges interested industries to discover a trade-off between these two demands. Furthermore, it is well known that modern CR technology enables the injection cycle to be split up into eight injections. Accordingly, each split injection is performed at different backpressures, which vary with crank angle degrees (CAD). This might lead the engine manufacturers to take backpressure into account to optimise the injection strategy.

CHAPTER 4

EXPERIMENTAL INVESTIGATION OF THE METHYLFURAN-DIESEL BLENDS' JET DEVELOPMENTS COMPARED TO DIESEL

A meaningful amount of this chapter has been published in the Elsevier journal, *Fuel*.

Coratella, C., Sahu, A., Parry, L., Xu, H., & Ma, X. (2020). 'Experimental investigation of the orifice-to-orifice variability in jet velocities in a diesel injector'. *Fuel*, 280, 118353.

This work has here been amended and reproduced with the permission of all co-authors.

Following the publication of the paper in the *Fuel* journal, the results have been further analysed. The additional findings have been described in the manuscript "Experimental investigation of the non-uniformity of the diesel jets' velocity distribution compared to 2-methylfuran-based blend" (AUIN-D-19-000106), which has been submitted to the journal, *Automotive Innovation*. Following a minor review by the journal, the manuscript has been revised and is currently at the final stage of the reviewing process.

Introduction

Recent years have seen radical changes in the global automotive scenario, caused by increasing demand for vehicular mobility. This issue has boosted the depletion of fossil energy sources, as well as causing a massive increase in pollutants' emissions. This framework has led the authorities to progressively lower the criteria for the pollutants' emissions' regulations. The automotive field has thereby endeavoured to explore innovative technologies aimed to limit the environmental impact of IC engines, pursuing three main goals:

- minimisation of pollutants' emissions;
- decrease in fuel consumption;
- slowdown of depletion of fossil energy sources.

With regard to the first two issues, a milestone for the minimisation of the carbon footprint of IC engines has been the introduction of the common rail system. The advent of this groundbreaking technology has indeed unlocked the potentialities of modern diesel engines in terms of higher engine efficiency and optimised fuel consumption, meeting the environmental mandates. Nevertheless, despite the progressively higher standards of diesel engine performances, several aspects, related to the optimisation of the injection strategy, still remain unclear. In fact, if on one hand these issues can be analysed by a thorough investigation, on the other hand further refinements of the CR system might be discouraged by the longstanding difficulties related to the achievement of zeroed emissions. In regards to the remaining goal, namely the need for a slowdown of the depletion of fossil energy sources, the automotive field has been urged to turn their attention to the development of biofuels. Several research efforts have been directed towards the assessment of the potentialities of a wide range of biofuels; which have proven to provide an attractive trade-off between engine efficiency and compliance with tailpipe emissions' legislation.

4.1 Literature review and proposed study

This section reviews the literature pertaining to furan-based biofuels, prompting the present research activity. It is followed by a brief description of the proposed study.

4.1.1 State of the art of methylfuran-based fuel blends

Nowadays, one of the most challenging issues for global mobility comes from the need to have a sustainable supply to meet the energy demand. Despite the outstanding improvements in electrical vehicles' performance, most of the transportation sector is still empowered by

fossil fuels; and a strong reliance on IC engines is still foreseen for the coming decades. This framework leads us to state that petroleum-free mobility is feasible only via the massive substitution of fossil fuels with biofuels. Therefore, as long as vehicular mobility cannot have total independence from IC engines, sustainable mobility is feasible only via superseding fossil fuels with biofuels. This scenario has shed light on ethanol as a promising blending agent. However, as mentioned in Chapter 1, a world-scale spread of ethanol is discouraged by several drawbacks, which have urged the research community to the turn their attention to processes converting biomass into biofuels.

4.1.1.1. The production technique of furan-based biofuels

In the light of the above scenario, the research community have shifted their attention to the production of biomass-derived fuels; prompting the adoption of interdisciplinary approaches to suppress the risk of detrimental competition in feedstock usage between the food chain and biofuel production. For this purpose, the outstanding progress has lifted the production techniques to a satisfactory efficiency. In this respect, a groundbreaking methodology, based on the reaction sequence to produce 2,5-dimethylfuran from fructose and glucose via dehydration and subsequent hydrogenolysis/hydrogenation**, (30, 37-38)** was developed by Dumesic and Román-Leshkov (Figure 4.1).

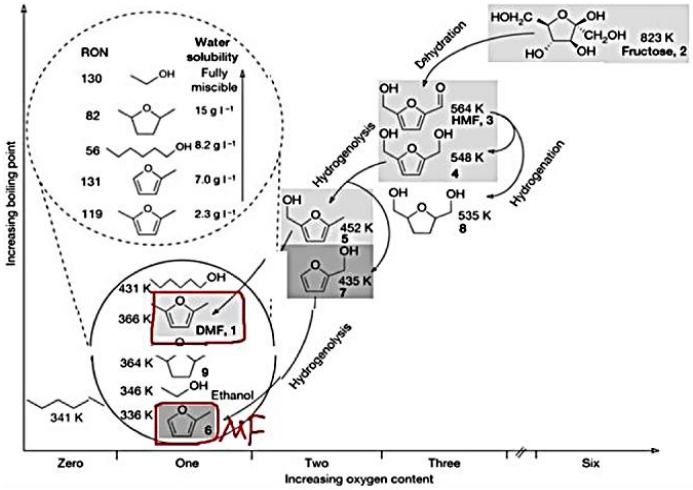


Figure 4.1. Schematisation of the process converting carbohydrates to MF **(30, 38, 106)**

The method essentially consists of selective oxygen removal, which is achievable in two stages. The removal of three oxygen atoms is firstly realised through dehydration to produce 5-hydroxymethylfurfural, followed by removing two oxygen atoms via hydrogenolysis to produce methylfuran. Additional refinement has been developed by Zhao *et al.*, whose approach significantly minimised the production costs. **(106, 107)** The reaction sequence however, required a large source of hydrogen. This issue led the fuel researchers to develop a novel reactions' sequence, starting with fructose and yielding 5-hydroxymethylfurfural via acid catalysed dehydration. Subsequently, the palladium-catalysed dehydroxylation, consisting of a two-phase reaction followed by decarbonylation, yields 2-methylfuran; its molecules were found to be more compact in comparison with 2,5-dimethylfuran (also known as DMF). **(37)** Within the framework of the chemical structure of furan-based biofuels, the chemical structure of MF (C_5H_6O) is fairly similar to DMF (C_6H_8O). The only difference consists of one less methyl on its cyclobenzene ring within the MF chemical structure. **(106)**

4.1.1.2. Literature review of MF-based fuels

Alongside the development and optimisation of the production techniques, several studies have proven the suitability of 2-methylfuran for IC engines, highlighting advantages such as higher knock resistance, better combustion process and lower emissions in comparison with traditional fuels.

Concerning the MF, a first step towards the assessment of MF-based biofuels was provided by Thewes *et al.* **(37)** From the experimental investigation, it emerged that MF-based biofuel is robust to cold engine starts, due to higher rates of vaporisation and higher combustion stabilities. Moreover, MF was revealed to be more prone to knock suppression in comparison with gasoline. This aspect might be crucial for the assessment of MF-based biofuels' suitability within SI engines, especially in the case of the need for higher compression ratios

or greater efficiencies attainable via engine '*downsizing*'. Additionally, the boiling temperature was found to be low, to the advantage of the mixture formation. With regard to emissions, it was observed that HC emissions from MF were appreciably lower than from gasoline. In contrast, the NO_X emissions still represent a concern, given the high MF flame temperature.

A key step towards a deeper knowledge of MF biofuels was made at the University of Birmingham, where furan-based blends were rigorously investigated. In fact, the University of Birmingham had the first research group who considered DMF as a potential fuel. **(108, 109)** Within this research activity, it was found that the properties of MF were similar to DMF. **(106)** In the wake of these findings, MF combustion performance and emissions were analysed in a single-cylinder SI engine. From the tests, it emerged that despite the similar chemical structure, MF combustion presented a notable difference from DMF. Indeed, the faster MF burning rate shortens the combustion duration and generates higher in-cylinder peak pressure. On the other hand, the similar chemical structure and molecular composition show DMF and MF have a better ability for knock suppression than gasoline. The faster burning rate, due to the tighter compactness of the MF molecules, greatly benefits an engine's thermal efficiency. With regard to emissions, MF was noted to produce 73% and 40% fewer HC emissions than gasoline and DMF respectively, thanks to the high combustion temperature and high oxygen content in its molecules. By contrast, the high in-cylinder temperature produces higher NO_X emissions. The formaldehyde emission from MF was the lowest, whilst the acetaldehyde was comparable to DMF and lower than gasoline and ethanol.

A significant contribution was also made by a research group at Aachen University. A robust experimental investigation was indeed performed, focusing on the comparison of furan-based fuels with gasoline and ethanol. An MF-fuelled engine was revealed to provide a comparable

or even better performance than gasoline and ethanol. **(37, 110)** The MF particularly revealed a better propensity towards knock suppression than gasoline, allowing greater compression ratios. Additionally, the burning rate was found to be significantly faster than gasoline. As a result, an improved combustion stability arose. Besides these findings, a favourable volumetric fuel consumption, thanks to the relatively high energy density, thermal efficiency and mass density were observed. More specifically, it was observed that the fuel consumption is similar to gasoline and considerably better than ethanol.

A further insight into the potentialities of methylfuran was given by Wang *et al*., who investigated the impacts of a low-level MF content in gasoline (volumetric 10% MF in blend) on a DISI engine's combustion and emissions. The tests revealed that adding 10% volumetric MF into gasoline determines negligible changes in combustion characteristics and combustion initiation delay. In contrast, combustion stability was meaningfully improved. With regard to the emissions, it emerged that the HC from MF10 was better than gasoline, whilst any significant difference emerged in the assessment of the NO_X emissions. However, MF10 revealed higher CO emissions. **(111)**

Similar conclusions were drawn by Hoppe *et al.,* who found that adding MF benefits the combustion stability, thanks to the higher vaporisation rate. **(112)** As result, it is presumable that this peculiarity of methylfuran might favour the engine's thermal efficiency.

A significant contribution to the assessment of MF's suitability for an IC engine was given by Wei *et al.* **(113)** An experimental investigation into combustion cyclic variation of neat MF, 10% and 20% volumetric of MF, was performed under various compression ratios and EGR rates. Along with shorter combustion duration, MF and MF-based blends exhibited also a lower cycle-to-cycle variation in combustion than for gasoline. It was seen also that the adding of MF benefits combustion stability, even in the case of a high EGR rate and retarded

spark timing. It was found that in the case of MF and MF-based blends, an increase in compression ratios does not imply an appreciable reduction in IMEP variability, unlike gasoline-like fuels. This might be ascribed to the faster MF burning rate. Overall, the experiments revealed the characteristics of MF favour the minimisation of the cyclic variation of engine combustion, especially when a high EGR rate and retarded spark timing have to be used.

Ma *et al*. performed an experimental investigation comparing the combustion characteristics of 2-methylfuran (MF) with MF–isooctane blended fuels via the high-speed Schlieren technique. **(114)** The tests were conducted employing MF20 and MF50 at high temperatures (333 K, 363 K and 393 K) under 1 bar of pressure in a constant volume vessel. The flame speeds of MF20 and MF50 were found to be between those of MF and isooctane. It was noted also that the blended fuel presented a less stable flame than for isooctane, whilst being more stable than the MF's flame. The difference between the flames of MF20 and MF50 is not significant.

With regard to the suitability of furan-based fuels for diesel engines, a thorough investigation has been carried out on CI engines, as reported by Zhang *et al.* **(115)** Conventional diesel was used as a base fuel for three tested blends. The DMF-diesel blends, referred to as D20 and D40 respectively, were characterised by a 20% and 40% of DMF volume fraction. The diesel-gasoline blend, referred to as G40, had a 40% by volume fraction of gasoline. The combustion and emissions of a single-cylinder CI engine fuelled with the above blends were compared. The diesel-DMF blends were found to have a longer DOI and faster burning if compared to G40. When the DMF fraction is up to 40%, it was demonstrated that soot emissions were close to zero; thus fulfilling the task to find a trade-off relationship between soot and NO_X. The DMF or gasoline additions were proven to slightly affect the CO emissions. Along with

the difference in the ignition delay and the oxygen content in the DMF molecules, the differences in the combustion and emissions' characteristics were greatly notable, especially for soot emissions.

Together with the high degree of renewability of fructose and the optimised production technique, the above literature review leads us to consider methylfuran-based blends as an appealing candidate to supersede conventional fuels, presenting a viable pathway for sustainable mobility. However, it can be noted that MF-based fuels have been investigated focusing on the combustion characteristics and emissions. Accordingly, the paucity of data concerning the MF-based fuels' injection has ensued, prompting this part of the thesis.

With regard to the orifice-to-orifice variability of the injected flow rate, an in-depth review of the literature is provided in the previous chapter.

4.1.2. The proposed study

In the wake of the results described in Chapter 3, this part of thesis aims to provide a further insight into the combined impact of fuel properties with injection settings on the orifice-to-orifice non-uniformity of jets' velocities. The present chapter indeed deals with the comparison between diesel and two MF-diesel blends (here referred to as MF30 and MF50, given the volumetric content of 30% and 50% methylfuran in the blend, respectively); focusing on the impact exerted by fuel viscosity and density both on the non-uniformity of the jets' velocities and on injection delay. As previously mentioned, this study was motivated also by the paucity of literature concerning the injection of furan-based fuels. Indeed, to the best of the author's knowledge, the furan-based fuels were assessed mainly focusing on the combustion process and emissions, thus revealing a knowledge gap about the injection characteristics. A robust experimental campaign was undertaken. Following on from the acquisition of the fuel plumes' images via a high-speed camera, an analysis of the combined

influence of injection settings with fuel properties on the injection process was carried out, focusing on the standard deviation of the jets' velocities and injection delay. In this respect, this chapter is intended as a follow-on stage of Chapter 3, which served as a baseline for this study. Sections 4.2 and 4.3 describe the experimental set-up and the methodology, respectively. Section 4.4 pertains to the experimental campaign, followed by a discussion of the results in section 4.5, which describes the physical principles underlying the findings. Conclusions are summarised in section 4.6.

4.2. Experimental set-up

Since the object of interest is the assessment of the combined impact of the injection settings with the fuel properties on hole-to-hole non-uniformity of jets' velocities and injection delay, the experimental set-up did not require any change. As such, the experimental system and the methodology did not differ from those described in Chapter 3. However, for the sake of completeness and consistency with Chapter 3, it was deemed necessary to provide the images of the processing for MF30 and MF50 plumes. The images refer to fuel plumes detected at an injection pressure and backpressure set at 1400 bar and 20 bar, respectively (Figures 4.2-4.3).

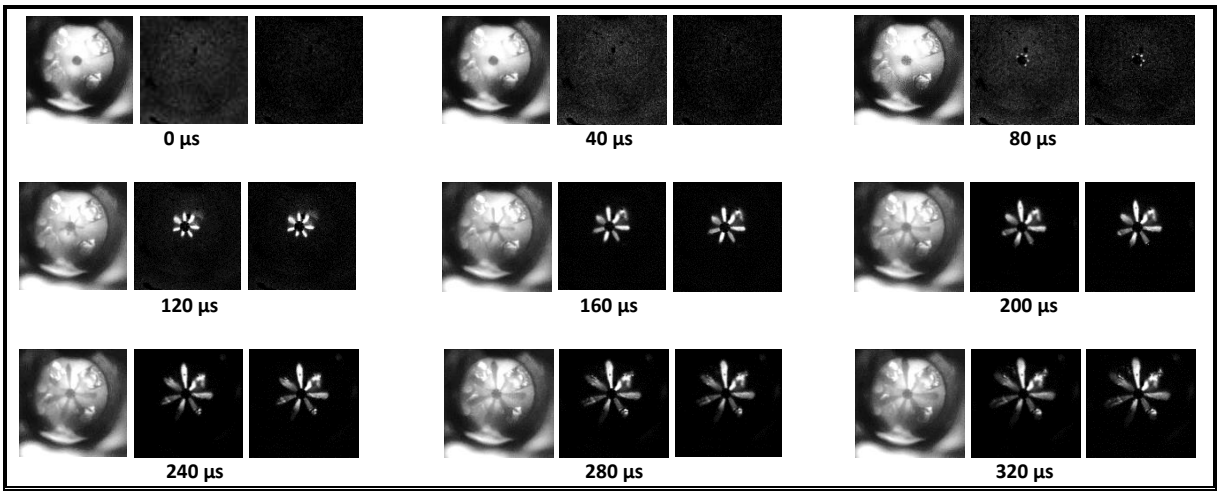


Figure 4.2. The sequence of MF30 plumes' images' processing, via the in-house developed MATLAB code and related time-stamps

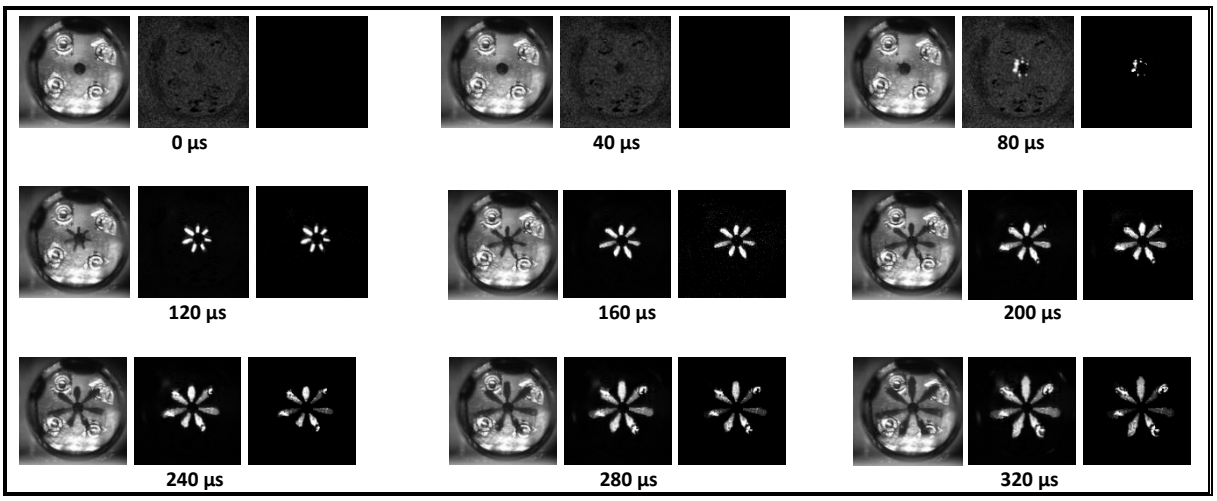


Figure 4.3. The sequence of the MF50 plumes' images' processing, via the in-house developed MATLAB code and related time-stamps

It is worth remarking that the short vessel might imply fuel jet impingement onto the windows. However, the quality of the images of the plumes was not adversely affected. In this regard, the impact of a refractive index on the quantitative statistics was not analysed.

4.3. Methodology

As mentioned above, the fulfilment of the aim required firstly the detection of the fuel plumes' images, which were captured by means of a high-speed camera. Thereafter, the analysis of the combined influence of the injection settings with fuel properties on the injection process was carried out, focusing on the standard deviation of the jets' velocities and injection delay.

4.3.1. Methodology for analysis of hole-to-hole non-uniformity of jets' velocities

This part of the thesis was carried out employing the methodology described in section 3 of the previous chapter, which served as a baseline for this study. Accordingly, in order to assess the orifice-to-orifice variability in the jet plumes' velocities, the standard deviation of the seven jet velocities was calculated, so as to provide an assessment of the dispersion of the data set.

4.3.2. Calculation of fuel blend properties

It has been widely demonstrated that fuel jet characteristics are determined by fuel properties, such as viscosity, density and surface tension. **(43)** Fuel viscosity gives rise to the shear stress on the needle. Indeed, along with density, viscosity affects the fluid's motion through the injector orifices. Viscosity determines the boundary layer arising along the orifice walls, thus affecting the fuel flow. Additionally, as discussed in-depth in Chapter 5, fuel viscosity exerts a significant influence on injection pressure fluctuations. Surface tension is meaningful of the intermolecular reaction arising in response to stress deforming the fluid (such as shear stress originating from air resistance acting on the droplet), and plays a pivotal role in jet break-up. However, the analysis of jet break-up does not lie within the scope of the present study. Accordingly, only viscosity and density are taken into account in this study. Table 4.1 provides the kinematic viscosity and density of diesel and 2-methylfuran at temperatures ranging from 30 ºC to 55 ºC.

Table 4.1. Properties of fuels compounding the blends tested here

	Kinematic Viscosity (m^2/s)	**Density (kg/m^3)**
2-methylfuran	$4.31 \cdot 10^{-6}$	872.19 - 902.65
diesel	$8.71 \cdot 10^{-7}$ - $4.95 \cdot 10^{-6}$	807.30 - 830.76

Diesel viscosity and density have been obtained according to the correlation found by Wang *et al.* **(101)** and Esteban *et al.* **(116)** respectively. Concerning the 2-methylfuran, Jezak *et al.* demonstrated that density is significantly determined by the temperature. **(117)** Once the viscosity and the density of a single component of the fuel is known, the overall properties can be calculated. In this regard, an overview of the methods calculating the blends' viscosity and density is needed. However, since the object of interest is the influence of fuel properties on orifice-to-orifice variability in jets' velocity, the sole ranking of the blends properties is deemed sufficient for the purpose of this study.

4.3.2.1. Calculation of blend viscosity

Although there has been progress in lifting the estimation of the blends' overall viscosity to a satisfactory accuracy, there is not any universal theory providing the exact calculation. **(118)** The existing theories are limited to the ideal binary blends, in which the mixing operation does not produce any change in volume. Therefore, the viscosity calculation for binary mixtures still represents a concern, given the large degree of the blending curves' nonlinearity. However, empirical formulas have been developed, such as the double logarithmic equation and the cubic-root equation, proposed by Refutas and Kendall-Monroe, respectively. **(118)** The Refutas equation calculates the binary blend viscosity from viscosities and weight fractions of the single components via the viscosity blending index (ASTM D7152). The blend viscosity is calculated as:

$$\mu_{12} = \exp\left[\exp\left(\frac{A12-10.975}{14.534}\right)\right] \quad (4.1)$$

where A_{12} stands for the average viscosity blending index and is given by:

$$A_{12} = \chi_1 \cdot A_1 + \chi_2 \cdot A_2 \quad (4.2)$$

χ_i refers to the weight fraction of the *i*-th component and the coefficient A_i is obtainable as:

$$A_i = 14.534 \cdot \ln\left[\ln\left(\mu_i + 0.8\right)\right] + 10.975 \quad (i = 1,2) \quad (4.3)$$

where μ_i refers to kinematic viscosity of the i-th component. According to the Kendall-Monroe equation, the blend viscosity is given by the cubic root average of the component viscosities and is achievable as follows:

$$\mu_{12}{}^{1/3} = \chi_1 \cdot \mu_1{}^{1/3} + \chi_2 \cdot \mu_2{}^{1/3} \quad (4.4)$$

An alternative approach has been proposed by Arrhenius, whose equation provides the dynamic viscosity of a binary blend as follows:

$$\ln\eta_{12} = \chi_1 \cdot \ln\eta_1 + \chi_2 \cdot \ln\eta_2 \quad (4.5)$$

with χ_i (i = 1, 2), η_{12}, η_1 and η_2 being the *i-th* component fraction, overall dynamic viscosity and single component viscosities, respectively. Table 4.2 shows the ranges of the blends' viscosities, achieved via the aforementioned methods.

Table 4.2. The ranges of MF30 and MF50 viscosities obtained according to the commonly employed methodologies

	Refutas	**Kendall-Monroe**	**Arrhenius**
MF30	$1.27 \cdot 10^{-6}$ - $3.86 \cdot 10^{-6}$ m^2/s	$1.55 \cdot 10^{-6}$ - $3.87 \cdot 10^{-6}$ m^2/s	$1.41 \cdot 10^{-6}$ - $3.86 \cdot 10^{-6}$ m^2/s
MF50	$1.69 \cdot 10^{-6}$ - $3.99 \cdot 10^{-6}$ m^2/s	$2.15 \cdot 10^{-6}$ - $3.99 \cdot 10^{-6}$ m^2/s	$1.94 \cdot 10^{-6}$ - $3.98\ 10^{-6}$ m^2/s

The viscosities range is determined by fuel temperature monitored on the microcontroller.

4.3.2.2. Estimation of blend density

As with the calculation of blend viscosity, there is no general formula to estimate the overall density of a blend compounded with two miscible liquids. However, overall density is commonly calculated as:

$$\rho_{TOT} = \Sigma \chi_i \cdot \rho_i \quad (4.6)$$

where χ_i and ρ_i refer to weight fraction and density of the i-th component, respectively. Hence, it is assumed that overall densities of the here-employed fuel blends are achievable as follows:

$$\rho_{12} = \chi_1 \cdot \rho_1 + \chi_2 \cdot \rho_2 \quad (4.7)$$

Accordingly, the MF30 density ranges from 826.77 kg/m^3 to 850.14 kg/m^3; whilst the MF50 density ranges from 839.74 kg/m^3 to 866.18 kg/m^3.

4.4. Experimental results

For reasons of consistency, all the research activities of this thesis were undertaken at the same injection settings, achievable by matching injection pressures and backpressures listed in Table 3.1, for a total of 16 injection configurations.

4.4.1. Temporal development of fuel jets' plumes

For the sake of brevity, the charts plotting the temporal development of the diesel plumes' lengths, shown by Figure 3.5 of Chapter 3, have not been shown in this subsection.

Therefore, Figures 4.4 and 4.5 show the time history of MF30 and MF50 PL exiting the injector orifices and averaged over five consecutive shots.

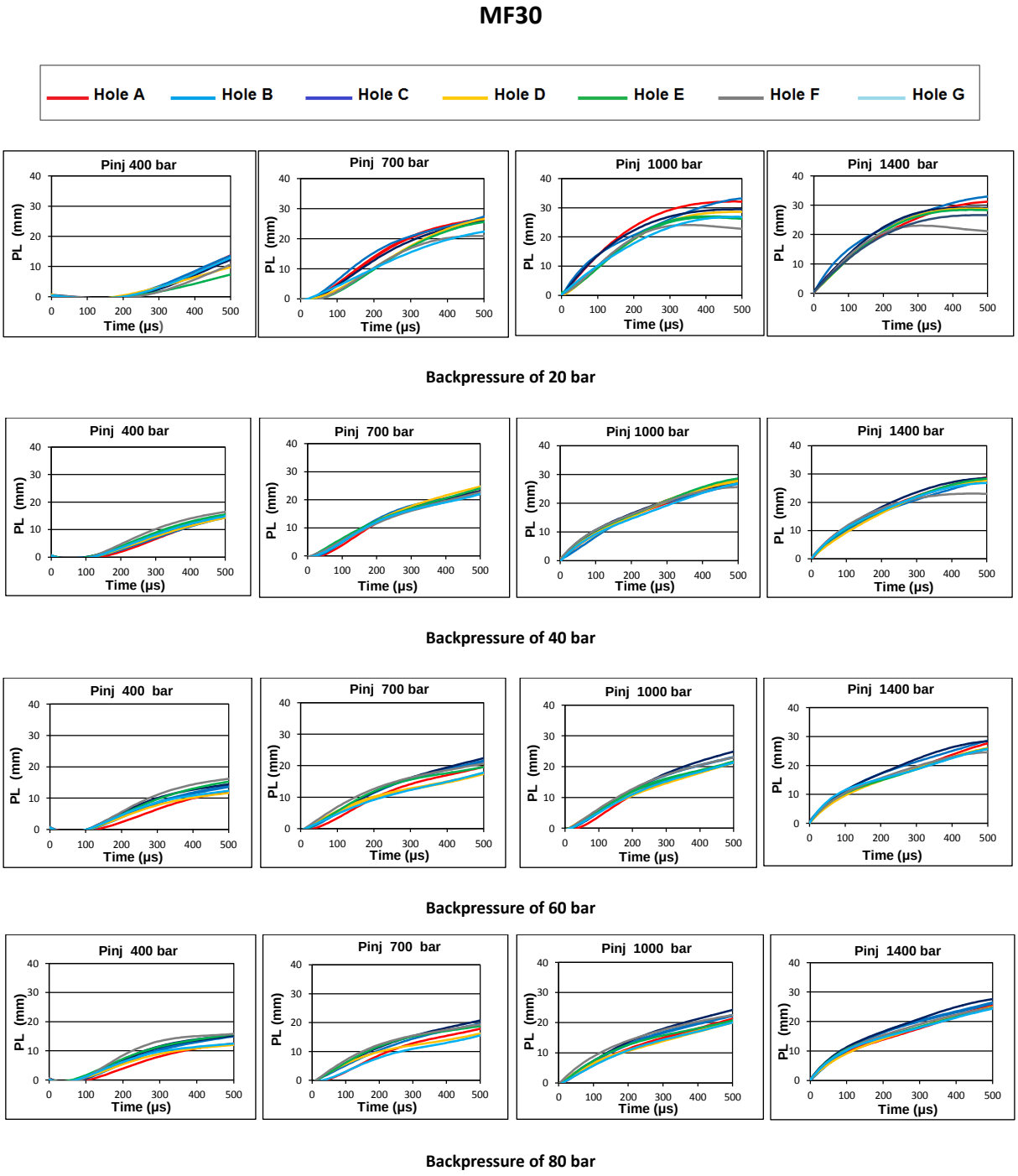


Figure 4.4. Time history of the averaged lengths of MF30 plumes

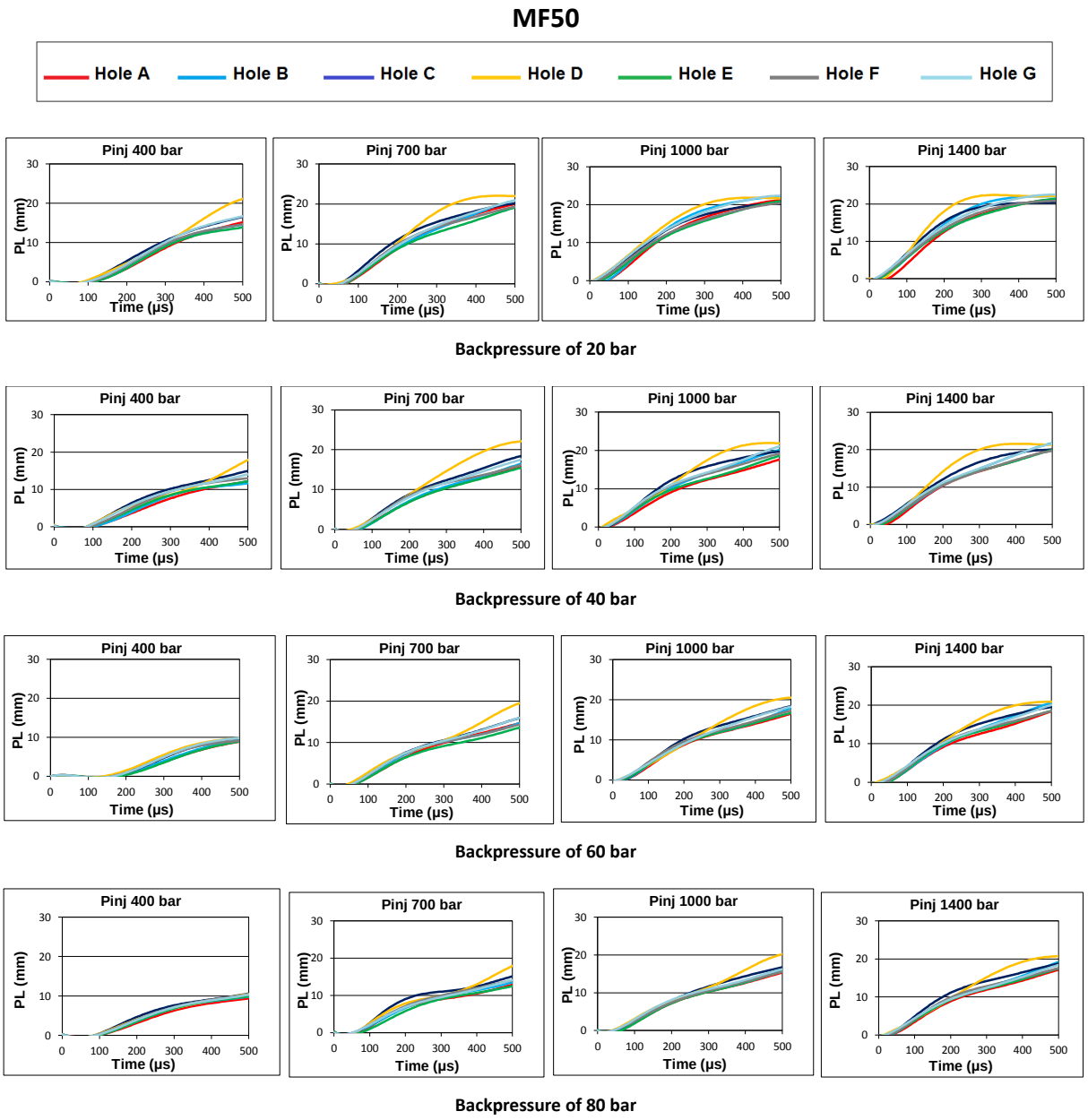


Figure 4.5. Time history of the averaged lengths of MF50 plumes

A quality review of the above charts leads to the argument that, along with greater propensity to prolong the injection start, MF50 yields expectedly shorter PLs in comparison with diesel and MF30. Moreover, at unvaried backpressure, increasing injection pressure is observed to narrow down the spread among the PL curves, when plotting the time-history of the MF30 and MF50 plumes' lengths. For MF30, at a constant injection pressure, the spread among the curves is more considerable at low backpressures.

With regard to MF50, although the PL curve referring to hole D reveals a propensity to

diverge from the rest of the jets in some cases, a smaller spread between the curves than for MF30 and diesel emerges. This smaller spread between the curves is indicative of a better uniformity of MF50 penetration rates in comparison with diesel and MF30.

Additionally, this difference is more observable at lower injection and backpressures. In this respect, the following subsections provide a more thorough analysis of above observations, focusing on standard deviations over the velocities of the fuel plumes exiting the injector.

4.4.1.1. The assessment of the orifice-to-orifice variability in fuel plumes' velocity

The averaged plume velocities and standard deviations are listed in Table 4.3 and 4.4 for MF30 and MF50, respectively. With regard to diesel, Table 3.3 of Chapter 3 shows its averaged plume velocities and standard deviations.

Table 4.3. Standard deviations of the averaged plumes' velocities detected at 40 μs of ASOI time (MF30)

	400 bar	**700 bar**	**1000 bar**	**1400 bar**
20 bar	50.72 m/s	32.04 m/s	31.46 m/s	25.06 m/s
40 bar	39.58 m/s	37.86 m/s	19.37 m/s	17.07 m/s
60 bar	56.05 m/s	47.38 m/s	40.76 m/s	17.94 m/s
80 bar	52.37 m/s	31.18 m/s	23.22 m/s	14.23 m/s

Table 4.4. Standard deviations of the averaged plumes' velocities detected at 40 μs of ASOI time (MF50)

	400 bar	**700 bar**	**1000 bar**	**1400 bar**
20 bar	27.34 m/s	29.69 m/s	10.25 m/s	45.62 m/s
40 bar	38.13 m/s	23.29 m/s	16.55 m/s	9.53 m/s
60 bar	20.43 m/s	21.12 m/s	15.67 m/s	22.15 m/s
80 bar	19.39 m/s	36.18 m/s	10.59 m/s	16.65 m/s

Figure 4.6 shows the surface maps referring to the MF30 and MF50 standard deviations as a function of injection pressure and backpressure.

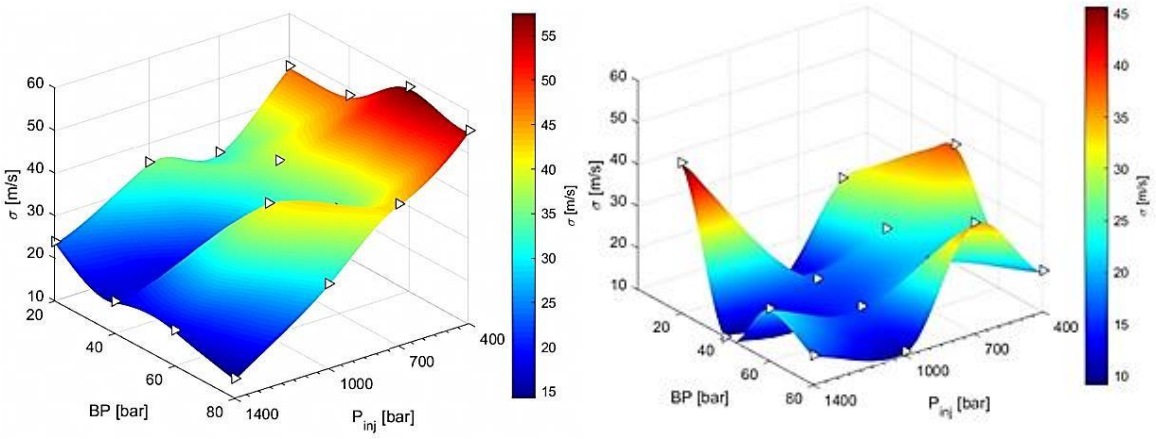


Figure 4.6. The standard deviations of MF30 a), and MF50 b), fuel plumes' velocities as a function of injection pressure and backpressure

Bearing in mind the surface map referring to diesel (Figure 3.8 in Chapter 3), and those in Figure 4.6 above, the comparison shows that MF50 injections yielded results deviating from the expectations based on Equation 3.5 in Chapter 3. In fact, at the highest injection pressure, the standard deviations are greater than for injections performed at lower injection pressures. More specifically, this emerges at injection settings of 1400-20 bar, 1400-60 bar and 1400-80 bar. In order to provide a better overview of the comparison between the tested fuels, the bar chart below enables the comparison between the standard deviations of averaged plumes' velocities measured at ASOI of 40 μs for each fuel (Figure 4.7).

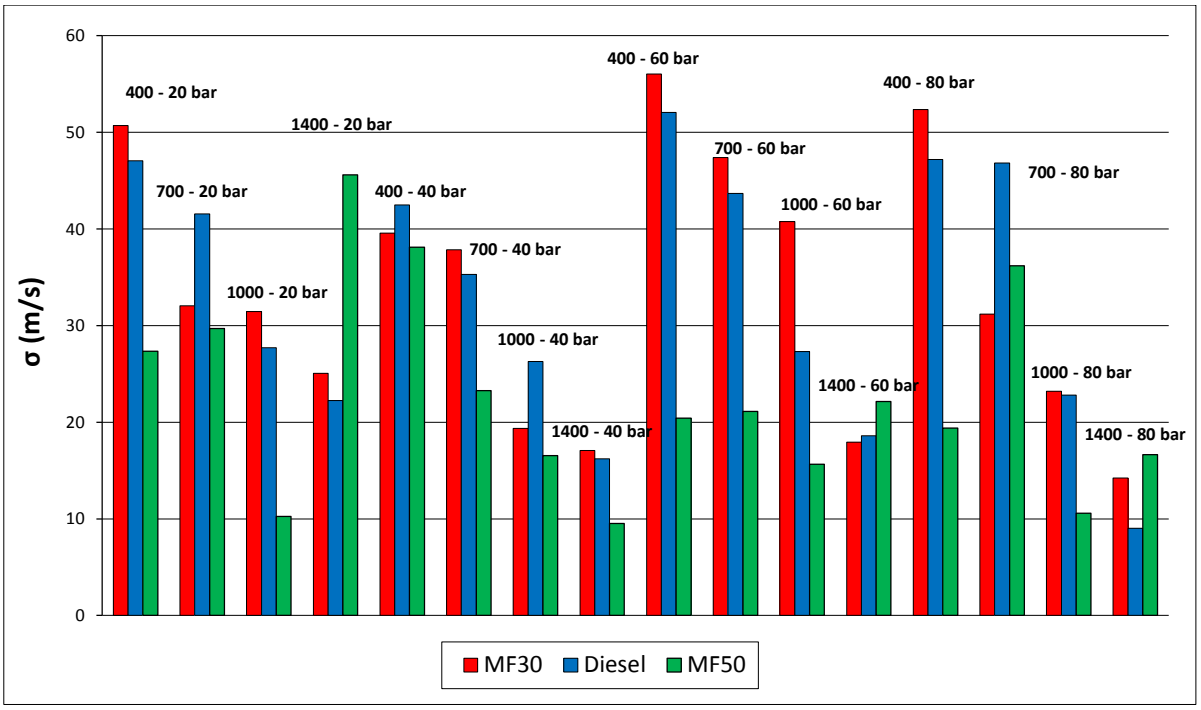


Figure 4.7. The standard deviations of the averaged plumes' velocities measured at early stages (≈ 40 μs) of the injection event

It can be seen that MF30 exhibits a worse distribution of plumes' velocities, given the larger standard deviations compared to diesel in the large majority of the cases. With regard to MF50, a better uniformity of the jets' velocities is observed, because of the lowest standard deviation in most cases. Accordingly, for diesel, its standard deviations are positioned between MF50 and MF30 in most cases.

It is noteworthy that, as with diesel, increasing injection pressure at a constant backpressure results in a decrease in standard deviation for MF30 injections; whilst MF50 exhibits an uneven trend of standard deviation. This resulted in unexpectedly greater values of standard deviation than for lower injection pressures. In particular, these results deviating from the expectations are observed for the injection configurations of 1400-20 bar, 1400-60 bar, 1400-80 bar and 700-80 bar.

The physical interpretation of these results is fully described in section 4.5. The explanation is

mainly focused on the competition between the effects of viscosity and density; whilst the uneven trends of the time history of MF50's standard deviation might be ascribed to hypothetical thermal effects. The effect of the higher backpressures on the uniformity of the plumes' velocities is further highlighted by the trend of the averaged reduction in standard deviation varying with backpressure (Tables 4.5-4.6). While, Table 3.11 of Chapter 3 lists the averaged reduction in standard deviation for diesel injections.

Table 4.5. Reductions in σ stemming from switching injection pressure to higher values at a constant backpressure (MF30**)**

	400 – 700 bar	**700 – 1000 bar**	**1000 – 1400 bar**	**Average of reduction in σ**
20 bar	18.68 m/s	0.58 m/s	6.41 m/s	8.55 m/s
40 bar	1.72 m/s	18.49 m/s	2.30 m/s	7.50 m/s
60 bar	8.67 m/s	6.61 m/s	22.82 m/s	12.70 m/s
80 bar	5.55 m/s	23.60 m/s	8.99 m/s	12.71 m/s

With regard to MF30, at a backpressure of 20 bar, varying injection pressure from 400 bar to 700 bar results in a reduction in standard deviation by approximately 18.68 m/s. Increasing injection pressure from 700 bar to 1000 bar and from 1000 bar to 1400 bar, reductions in standard deviation are approximately estimated at 0.58 m/s and 6.41 m/s, respectively. Similarly, the fifth column of Table 3.11 in Chapter 3 exhibits an increasing trend of overall reduction in standard deviation. The most dramatic reductions in the standard deviation of jet velocities are discernible at backpressures of 60 bar and 80 bar, where it reduces by ~ 12.70 m/s as the injection pressure is switched from 400 to 1400 bar. Whilst equal switching of injection pressure at a backpressure of 20 bar results in an average reduction by 8.55 m/s. Concerning the MF50, the following table shows the variation in σ stemming from switching injection pressure to higher values at a constant backpressure.

Table 4.6. Reductions in σ stemming from switching injection pressure to higher values at a constant backpressure (MF50)

	400 – 700 bar	**700 - 1000 bar**	**1000 - 1400 bar**	**Averages**
20 bar	-2.35 m/s	19.44 m/s	-35.37 m/s	-6.09 m/s
40 bar	14.84 m/s	6.74 m/s	7.02 m/s	9.53 m/s
60 bar	-0.69 m/s	5.45 m/s	-6.48 m/s	-0.57 m/s
80 bar	-20.92 m/s	29.72 m/s	-6.07 m/s	0.91 m/s

Although the standard deviation of the fuel's plumes' velocities is lower than for diesel and MF30 in the majority of the cases, indicating a better uniformity of the fuel's velocity distribution, the trend of variation is fairly uneven. From the last column, regarding the averages of variation in the standard deviation, it emerges that switching injection pressure to higher values does not result in positive effects for the uniformity of the jets' velocities. Accordingly, it might be presumed that, within certain viscosity and density ranges, a greater tendency towards the uniformity of plumes' velocity distribution characterises the injections if performed at a higher backpressure. Namely, if viscosity and density are within certain limits, the favouring effect of injection pressure on the uniformity of plumes' velocities is enhanced at increasing backpressures. Beyond certain ranges, it is presumable that, if on the one hand greater viscosity and density contribute to the minimisation of the non-uniformity of jets' velocities, on the other hand the beneficial impact of increasing injection pressure at higher backpressure tends to deteriorate. The reasons underlying this discrepancy are fully explained in section 4.5.

4.4.1.2. Assessment of hole-to-hole variability according to an alternative approach

As in Chapter 3, an assessment of the variability of the plumes' velocity was carried out according to an alternative statistical approach. The averages of the standard deviations of the fuel plumes' velocity exiting each hole were calculated over five consecutive shots. Table 3.12 of Chapter 3 and Tables 4.7-4.8 illustrate the averaged standard deviations referring to injections performed employing the fuels tested here.

Table 4.7. Averaged standard deviations of plumes' velocities at 40 μs of ASOI over five consecutive MF30 shots

	400 bar	**700 bar**	**1000 bar**	**1400 bar**
20 bar	53.89 m/s	60.36 m/s	24.67 m/s	37.53 m/s
40 bar	54.68 m/s	51.40 m/s	16.52 m/s	22.50 m/s
60 bar	62.64 m/s	37.31 m/s	45.29 m/s	23.43 m/s
80 bar	55.24 m/s	73.65 m/s	41.39 m/s	16.70 m/s

Table 4.8. Averaged standard deviations of plumes' velocities at 40 μs of ASOI over five consecutive MF50 shots

	400 bar	**700 bar**	**1000 bar**	**1400 bar**
20 bar	38.60 m/s	34.79 m/s	30.49 m/s	29.53 m/s
40 bar	45.76 m/s	34.09 m/s	18.69 m/s	34.92 m/s
60 bar	40.04 m/s	27.94 m/s	20.97 m/s	30.94 m/s
80 bar	26.39 m/s	35.56 m/s	29.01 m/s	16.42 m/s

The bar chart below illustrates the averaged standard deviations of MF30, MF50 and diesel plumes' velocities detected at 40 μs of ASOI (Figure 4.8).

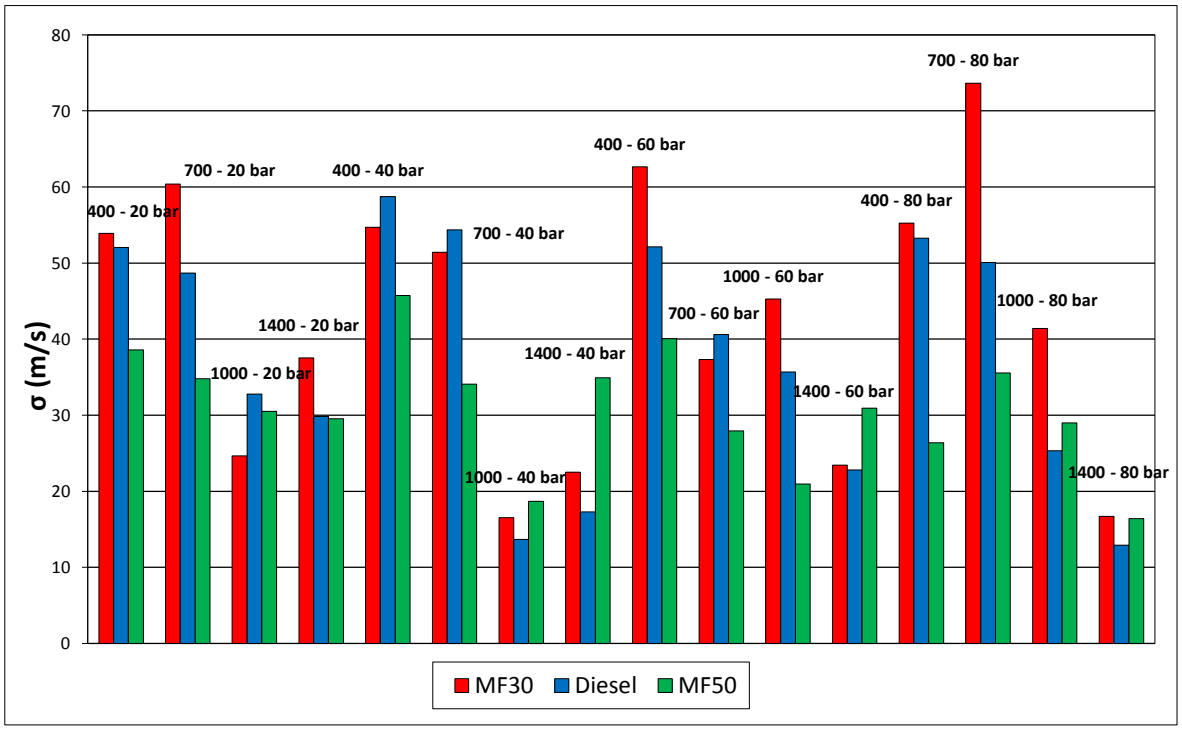


Figure 4.8. The standard deviations of plumes' velocities calculated according to the alternative statistical approach

Like the first statistical method, M30 tends to exhibit a greater variability of plumes' velocities in the majority of the cases; whilst MF50 shows the lowest standard deviations. With regards to diesel, standard deviations' values are positioned between MF30 and MF50 in most cases. Accordingly, it can be argued that MF50 shots are more prone to uniformity of the plumes' velocities in comparison with MF30 and diesel. However, some discrepancies can be observed. Diesel at injection settings of 1000-20 bar, 400-40 bar, 700-40 bar and 700-60 bar exhibits the highest standard deviations. Conversely, diesel also shows the lowest standard deviations at 1000-40 bar, 1400-40 bar, 1400-60 bar and 1400-80 bar.

Further disagreement can be seen for MF50, which exhibits the greatest standard deviation at injection configurations of 1000-40 bar, 1400-40 bar and 1400-60 bar. It is noteworthy that these disagreements arose at higher injection pressures, resulting in unexpectedly greater standard deviation than for lower injection pressures. Moreover, as with the first method, diesel and MF30 show a fairly decreasing trend of standard deviation in response to increasing injection pressure at constant backpressure; whilst MF50 exhibits an uneven trend. As previously mentioned, the reasons underlying these findings are explained in the next sections.

As with the previous subsection, an analysis of variation in standard deviation with backpressure was carried out. Table 3.13 of Chapter 3 and Tables 4.9-4.10 show the reduction in standard deviation stemming from an increase in injection pressure at higher backpressure.

As with diesel, MF30 injections are prone to present a more uniform distribution of the plumes' velocity when increases in injection pressure are set at a higher backpressure.

Table 4.9. Reductions in σ stemming from switching injection pressure to higher values at a constant backpressure (MF30)

	400 - 700 bar	**700 - 1000 bar**	**1000 - 1400 bar**	**Average**
20 bar	-6.48 m/s	35.69 m/s	-12.84 m/s	5.46 m/s
40 bar	3.29 m/s	34.872 m/s	-5.98 m/s	10.73 m/s
60 bar	25.33 m/s	-7.97 m/s	21.86 m/s	13.07 m/s
80 bar	-18.41 m/s	32.25 m/s	24.70 m/s	12.85 m/s

Nonetheless, it is observable that, at a backpressure of 20 bar, the standard deviation increases by 6.48 m/s and 12.84 m/s in response to switching the injection pressure from 400 bar to 700 bar and from 1000 bar to 1400 bar, respectively. At a backpressure of 40 bar, a similar discrepancy emerged from switching the injection pressure from 1000 bar to 1400 bar, which results in an increase in standard deviation by 5.98 m/s. With regards to a backpressure of 60 bar the inconsistency refers to varying the injection pressure from 700 bar to 1000 bar, implying an increase by 7.97 m/s. At 80 bar, varying the injection pressure from 400 bar to 700 bar, the standard deviation is observed to increase by 18.41 m/s. However, Tables 3.11, 3.13, 4.5 and 4.9 lead to the idea that the benefit of increasing injection pressure on the jets'

development uniformity is enhanced in the case of higher backpressure. Indeed, the average reductions in σ due to the increasing injection pressure exhibit a fairly increasing trend from backpressures of 20 bar to 80 bar. By contrast, MF50 injections revealed a different behaviour (Table 4.10).

Table 4.10. Reductions in σ stemming from switching injection pressure to higher values at a constant backpressure (MF50)

	400 - 700 bar	**700 - 1000 bar**	**1000 - 1400 bar**	**Averages**
20 bar	3.81 m/s	4.29 m/s	0.96 m/s	3.02 m/s
40 bar	11.67 m/s	15.39 m/s	-16.23 m/s	3.61 m/s
60 bar	12.10 m/s	6.97 m/s	-9.97 m/s	3.03 m/s
80 bar	-9.17 m/s	6.55 m/s	12.59 m/s	3.32 m/s

Indeed, a fairly uneven trend of averaged reduction in standard deviations, arisen in response to an increase in backpressure, is observable. In this respect, section 4.5 provides a full discussion explaining these findings.

4.4.2. The acquisition of injection delays

This subsection pertains to the acquisition of injection delays; the estimation of which is based on the appearance of plumes exiting each of seven injector holes. Being as diesel DOIs are shown in subsection 3.5.4 in Chapter 3, the following Tables 4.11-4.14 and 4.15-4.18 refer only to MF30 and MF50 delays, respectively.

Table 4.11. Delays of MF30 injections in μs detected at various injection pressures and a backpressure of 20 bar

	400 – 20 bar					**700 – 20 bar**						**1000 – 20 bar**					**1400 – 20 bar**				
A hole	320	320	320	360	280	120	80	80	80	40	0	0	0	0	0	0	0	0	0	0
B hole	280	280	280	320	280	120	80	40	40	40	0	0	0	0	0	0	0	0	40	0
C hole	320	320	320	320	280	120	80	80	80	40	40	0	0	0	0	40	0	0	0	0
D hole	320	320	360	360	280	120	80	80	80	40	40	0	0	0	0	40	0	0	0	0
E hole	360	360	320	320	320	120	160	80	40	80	40	0	0	0	0	40	0	0	0	0
F hole	360	360	360	360	320	160	160	80	80	80	40	0	0	0	0	40	0	0	0	0
G hole	320	320	280	320	280	120	80	80	40	40	40	0	0	0	0	0	0	0	0	0
Average	325.71	325.71	320	337.14	291.43	125.71	102.6	74.29	62.86	51.43	28.57	0	0	0	0	22.86	0	0	5.71	0
St. Dev.	27.60	27.60	32.66	21.38	19.52	15.12	39.04	15.12	21.38	19.52	19.52	0	0	0	0	21.38	0	0	15.12	0
Error	40	40	40	20	20	20	40	20	20	20	20	0	0	0	0	20	0	0	20	0

Table 4.12. Delays of MF30 injections in μs detected at various injection pressures and a backpressure of 40 bar

	400 – 40 bar					**700 – 40 bar**						**1000 – 40 bar**					**1400 – 40 bar**				
A hole	320	240	200	200	160	80	80	80	80	80	40	0	0	0	0	40	0	0	0	0
B hole	240	240	160	200	200	120	80	40	40	40	40	0	0	0	0	40	0	0	0	0
C hole	320	200	160	200	200	80	40	40	40	40	40	0	0	0	0	40	0	0	0	0
D hole	280	200	160	200	200	80	40	40	40	40	40	0	0	0	0	40	0	0	0	0
E hole	240	200	160	200	200	80	40	40	40	40	40	0	0	0	0	40	0	0	0	0
F hole	200	200	160	200	200	80	40	40	40	40	40	0	0	0	0	0	0	0	0	0
G hole	240	240	160	200	200	80	80	40	40	40	40	0	0	0	0	40	0	0	0	0
Average	262.86	217.14	165.71	200	194.29	85.71	57.14	45.71	45.71	45.71	40	0	0	0	0	34.29	0	0	0	0
St. Dev.	45.36	21.38	15.12	0	15.12	15.12	21.38	15.12	15.12	15.12	0	0	0	0	0	15.12	0	0	0	0
Error	60	20	20	0	20	20	20	20	20	20	0	0	0	0	0	20	0	0	0	0

Table 4.13. Delays of MF30 injections in µs detected at various injection pressures and a backpressure of 60 bar

	400 – 60 bar					700 – 60 bar					1000 – 60 bar					1400 – 60 bar				
A hole	200	200	200	200	200	80	80	40	40	40	80	80	80	80	80	0	0	0	0	0
B hole	200	200	160	160	160	80	80	40	80	40	80	80	40	40	40	0	0	0	0	0
C hole	160	160	160	160	160	80	80	40	40	40	80	80	40	40	40	0	0	0	0	0
D hole	160	160	160	160	160	80	80	40	40	40	80	40	40	40	40	0	0	0	0	0
E hole	160	160	160	160	160	80	80	40	80	40	80	40	40	40	40	0	0	0	0	0
F hole	160	160	160	160	160	40	40	40	40	40	80	40	40	40	40	0	0	0	0	0
G hole	160	160	160	160	160	120	80	40	40	40	80	80	40	40	40	0	0	0	0	0
Average	171.43	171.43	165.71	165.71	165.71	80	74.29	40	51.43	40	80	62.86	45.71	45.71	45.71	0	0	0	0	0
St. Dev.	19.52	19.52	15.12	15.12	15.12	23.09	15.12	0	19.52	0	0	21.38	15.12	15.12	15.12	0	0	0	0	0
Error	20	20	20	20	20	40	20	0	20	0	0	20	20	20	20	0	0	0	0	0

Table 4.14. Delays of MF30 injections in µs detected at various injection pressures and a backpressure of 80 bar

	400 – 80 bar					700 – 80 bar					1000 – 80 bar					1400 – 80 bar				
A hole	200	160	160	160	160	80	80	80	80	80	40	40	40	40	40	0	0	0	0	0
B hole	160	120	120	160	120	80	80	80	80	80	40	40	40	40	40	0	0	0	0	0
C hole	160	120	120	120	120	40	80	40	40	40	40	40	40	40	40	0	0	0	0	0
D hole	160	120	120	120	120	40	40	40	40	40	40	40	40	40	40	0	0	0	0	0
E hole	120	120	120	120	80	40	40	40	40	40	40	40	40	40	40	0	0	0	0	0
F hole	120	120	120	120	120	40	40	40	40	40	40	40	0	0	0	0	0	0	0	0
G hole	120	120	120	120	120	80	80	80	80	80	80	40	40	40	40	0	0	0	0	0
Average	148.57	125.71	125.71	131.43	120	57.14	62.86	57.14	57.14	57.14	45.71	40	34.29	34.29	34.29	0	0	0	0	0
St. Dev.	30.24	15.12	15.12	19.52	23.09	21.38	21.38	21.38	21.38	21.38	15.12	0	15.12	15.12	15.12	0	0	0	0	0
Error	40	20	20	20	40	20	20	20	20	20	20	0	20	20	20	0	0	0	0	0

Table 4.15. Delays of MF50 injections in µs detected at various injection pressures and a backpressure of 20 bar

	400 – 20 bar					700 – 20 bar					1000 – 20 bar					1400 – 20 bar				
A hole	160	160	160	160	160	120	80	80	80	120	80	80	40	40	40	40	40	80	40	
B hole	160	160	160	160	160	80	80	80	80	80	80	40	40	40	40	40	40	40	80	40
C hole	160	160	120	120	160	80	80	80	80	80	40	40	40	40	40	40	40	40	40	40
D hole	120	120	120	160	160	80	80	80	80	80	40	0	40	40	40	40	40	40	40	40
E hole	160	160	160	160	160	80	80	80	80	120	80	40	40	40	40	40	40	40	40	40
F hole	160	160	160	120	160	80	80	80	80	120	40	40	40	40	40	40	40	40	40	40
G hole	160	160	120	120	160	80	80	80	80	80	40	40	40	0	40	40	40	40	40	40
Average	154.29	154.29	142.86	142.86	160	85.71	80	80	80	97.14	57.14	40	40	34.29	40	40	40	40	51.43	40
St. Dev.	15.12	15.12	21.38	21.38	0	15.12	0	0	0	21.38	21.38	23.09	0	15.12	0	0	0	0	19.52	0
Error	20	20	20	20	0	20	0	0	0	20	20	40	0	20	0	0	0	0	20	0

Table 4.16. Delays of MF50 injections in µs detected at various injection pressures and a backpressure of 40 bar

	400 – 40 bar					700 – 40 bar					1000 – 40 bar					1400 – 40 bar				
A hole	160	160	160	120	160	120	80	80	80	80	40	40	80	40	40	40	80	80	40	40
B hole	160	120	160	120	160	120	80	80	120	80	40	40	80	40	40	40	80	80	40	40
C hole	120	120	120	120	120	120	80	80	80	80	40	40	80	40	40	40	40	80	40	0
D hole	120	120	120	120	120	120	80	80	80	80	40	40	80	40	40	40	80	80	40	0
E hole	120	120	120	120	120	160	80	80	80	80	40	40	80	40	40	40	40	80	40	40
F hole	120	120	160	120	160	120	80	80	80	80	40	40	80	40	40	40	40	80	40	40
G hole	120	120	120	120	120	120	80	80	80	80	40	40	80	40	40	40	40	80	40	0
Average	131.43	125.71	137.14	120	137.14	125.71	80	80	85.71	80	40	40	80	40	40	40	57.14	80	40	22.86
St. Dev.	19.52	15.12	21.38	0	21.38	15.12	0	0	15.12	0	0	0	0	0	0	0	21.38	0	0	21.38
Error	20	20	20	0	20	20	0	0	20	0	0	0	0	0	0	0	20	0	0	20

Table 4.17. Delays of MF50 injections in µs detected at various injection pressures and a backpressure of 60 bar

	400 – 60 bar					700 – 60 bar					1000 – 60 bar					1400 – 60 bar				
A hole	320	200	240	240	200	80	80	80	80	120	40	40	80	80	80	40	80	80	80	80
B hole	320	200	200	240	200	80	80	80	80	120	40	40	40	80	80	40	80	80	80	80
C hole	320	200	200	240	200	80	80	80	80	80	40	40	40	80	80	40	40	40	80	80
D hole	280	160	200	200	200	120	80	80	80	80	40	40	40	80	80	40	40	40	80	80
E hole	320	200	240	240	240	80	80	80	80	120	40	40	40	80	80	40	40	40	80	80
F hole	320	200	200	240	200	80	80	80	80	80	40	40	40	40	80	40	80	40	80	80
G hole	320	200	200	240	200	120	80	80	80	80	40	40	40	40	80	40	40	40	80	80
Average	314.29	194.29	211.43	234.29	205.71	91.43	80	80	80	97.14	40	40	45.71	68.5	80	40	57.14	51.43	80	80
St. Dev.	15.12	15.12	19.52	15.12	15.12	19.52	0	0	0	21.3	0	0	15.12	19.5	0	0	21.38	19.52	0	0
Error	20	20	20	20	20	20	0	0	0	20	0	0	20	20	0	0	20	20	0	0

Table 4.18. Delays of MF50 injections in μs detected at various injection pressures and a backpressure of 80 bar

	400 – 80 bar					700 – 80 bar					1000 – 80 bar					1400 – 80 bar				
A hole	120	160	160	160	160	120	80	120	120	120	120	80	80	80	80	40	40	40	80	80
B hole	120	160	160	160	120	80	80	120	80	80	120	40	40	80	80	40	40	40	80	80
C hole	120	120	160	160	120	80	80	120	80	80	120	40	40	80	80	40	40	40	80	40
D hole	120	120	160	160	120	80	80	120	80	80	80	40	40	80	80	40	40	40	80	80
E hole	120	160	160	160	160	120	80	120	120	120	120	40	40	80	80	40	40	40	80	80
F hole	120	120	160	160	120	80	80	120	80	80	120	40	40	80	80	40	40	40	80	80
G hole	120	160	160	160	120	80	80	120	80	80	80	40	40	80	80	40	40	40	40	80
Average	120	142.86	160	160	131.43	91.43	80	120	91.43	91.43	108.57	45.71	45.71	80	80	40	40	40	74.29	74.291
St. Dev.	0	21.38	0	0	19.52	19.52	0	0	19.52	19.52	19.52	15.12	15.12	0	0	0	0	0	15.12	15.12
Error	0	20	0	0	20	20	0	0	20	20	20	20	20	0	0	0	0	0	20	20

As expected, the averaged delays of MF50 injections are longer than those for MF30 and diesel. Tables 4.19-4.20 list the averages of the DOIs calculated over the values shown by the 8th rows of Tables 4.11-4.14 and 4.15-4.19, referring to MF30 and MF50, respectively.

Table 4.19. Delays of MF30 injections averaged over five injections

	400 bar	**700 bar**	**1000 bar**	**1400 bar**
20 bar	320 μs	83.43 μs	5.71 μs	5.71 μs
40 bar	208 μs	56 μs	8 μs	6.86 μs
60 bar	168 μs	57.14 μs	56 μs	0 μs
80 bar	130.29 μs	58.29 μs	37.71 μs	0 μs

Table 4.20. Delays of MF50 injections averaged over five injections

	400 bar	**700 bar**	**1000 bar**	**1400 bar**
20 bar	150.86 μs	84.57 μs	42.29 μs	42.29 μs
40 bar	130.29 μs	90.29 μs	48 μs	48 μs
60 bar	232 μs	85.71 μs	54.86 μs	61.71 μs
80 bar	142.86 μs	94.86 μs	72 μs	53.71 μs

With regards to diesel, Table 3.14 (see Chapter 3) shows the averages of the DOIs calculated over the values shown by the last rows of Tables 3.5-3.8. For MF30, except for the injection pressure of 1000 bar, a slightly decreasing trend of averaged DOI, arisen in response to increasing backpressure, is observed for all injection pressures. More specifically, at an injection pressure of 400 bar, an increase in backpressure generates a reduction in averaged DOI. Likewise, at an injection pressure of 700 bar and 1400 bar, a decreasing trend can be seen. Nonetheless, at an injection pressure of 700 bar, a negligible increase in averaged DOI is observed when backpressure varies from 40 bar to 60 bar. Similarly, at an injection pressure of 1400 bar, varying the backpressure from 20 bar to 40 bar gives rise to a negligible

increase in averaged DOI, from 5.71 μs to 6.86 μs.

Concerning the MF50 injection delays, except for the injection pressure of 400 bar, increasing the backpressure prolongs the averaged DOI. At an injection pressure of 400 bar, inconsistencies are observed when the backpressure switches from 20 bar to 50 bar and from 60 bar to 80 bar. Nevertheless, some inconsistencies emerged. At an injection pressure of 700 bar, switching the backpressure from 40 bar to 60 bar determines a reduction in averaged DOI from 90.29 μs to 85.71 μs. Whilst, at an injection pressure of 1400 bar, switching the backpressure from 60 bar to 80 bar shortens the averaged DOI from 61.71 μs to 53.71 μs. Noting the case of the injection pressure of 400 bar, the trend of the averaged DOI is fairly irregular. The following bar chart summarises the above results, enabling a comparison between the averaged DOIs of the tested fuels (Figure 4.9).

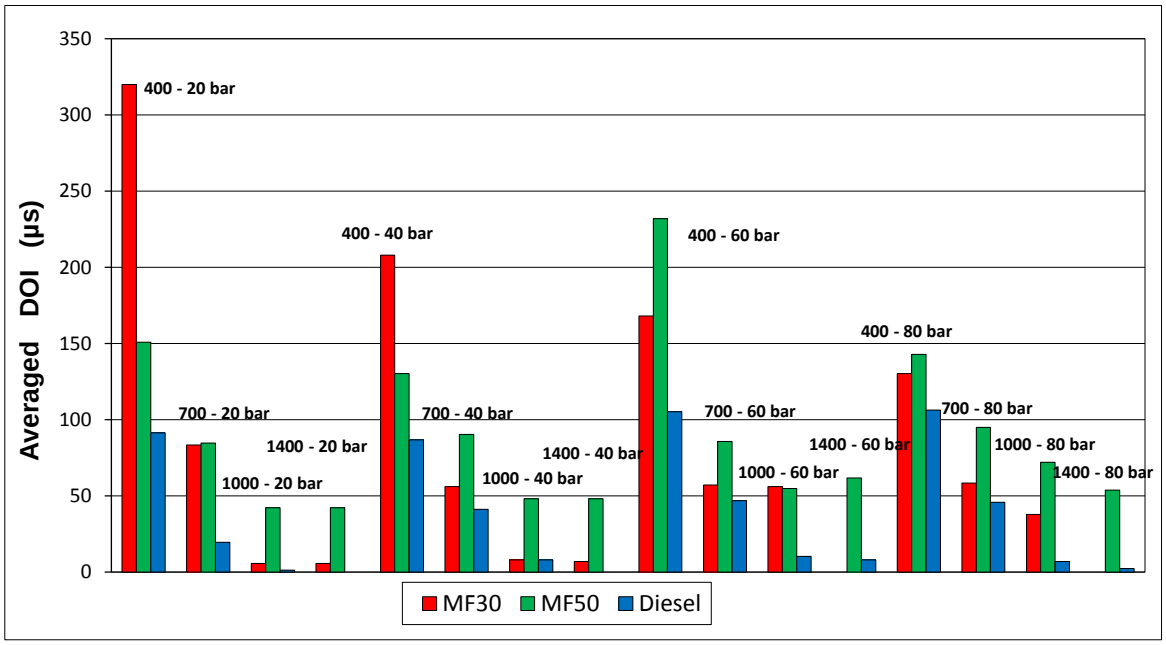


Figure 4.9. Averaged DOIs referring to diesel, MF30 and MF50 at various injection settings

The MF50 injections are characterised by the longest DOI, with the exception of the injection settings 400-20 bar, 700-20 bar and 1000-60 bar. With regards to diesel, it exhibited the shortest DOIs in most cases, except for injection configurations of 1400-60 bar and 1400-80

bar. Therefore, the averaged MF30 DOIs are mid-positioned between the MF50 and diesel cases. The physical interpretation underlying the emerged findings is provided in the following sections.

4.5. Discussion of the results

This section provides a physical interpretation of the findings and related inconsistencies; focusing on the influence of injection settings with fuel properties on needle motions, which govern the variability of the plumes' velocity and injection delays. The combined effect of the factors described below is thought to explain the observed results.

4.5.1. The impact of injection settings on needle motions

From the conclusions reached in Chapter 3, the results can be explained assuming that, at commencing injection, fuel momentum can be subdivided into the contribution transferred onto the needle and the contribution promoting flow towards the orifice inlet. **(105, 119)** As previously considered in Chapters 2 and 3, this assumption suggests that, at a constant injection pressure, low backpressure enhances flow towards the orifices. A decreased momentum transferrable to the needle ensues, leading to a slower needle lift. Being as off-axis motion is enhanced by a prolonged lift, wider oscillations arise, causing larger differences among the cross-sectional areas through which fuel flows. Larger orifice-to-orifice variability in the velocities of the fuel plumes thereby ensues. Likewise, under constant backpressure, decreasing injection pressure results in slower lift, leading to wider and prolonged needle oscillations. As the needle approaches the highest position, the effects of off-axis motion on variability decay, due to the negligibility of the needle axis misalignment at a longer distance from the needle seat.

Furthermore, keeping in mind Figure 3.14 in Chapter 3, the force on the needle can be subdivided into radial and axial components. In this respect, it has been demonstrated that the

needle axial displacement always outweighs the radial motion, given the mechanical constraints and traditional design of the needle-nozzle assembly. This explains the predominance of the axial component of the force over the radial component. **(64, 82-84)** These findings lead to conjecture that the predominance of needle lift over the radial motion is more significant at higher injection pressures. Likewise, given the observed reduction in standard deviation due to the increasing backpressure in most cases, axial motion outweighs the radial motion more significantly at higher backpressures. In other terms, the predominance of the force of the axial component over the radial component is more noticeable at higher injection pressure and increasing backpressures. Accordingly, the combined increase in injection pressure and backpressure benefits the uniformity of the jets' velocity distribution in most cases.

Nonetheless, some inconsistencies were observed. The disagreements might be ascribed to the action of higher backpressures on the needle. In fact, if on one hand greater backpressure is believed to promote fuel momentum onto the needle, on the other it is supposed to contribute moderately also to the misalignment. In this respect, the geometry of the needle protrusion might be a key-factor determining this aspect. However, the analysis of the results revealed that the detrimental impact of the radial component is more noticeable at the lowest injection pressures. It is worth noting that these findings lie within the results available in the literature review.

4.5.2. The impact of injector characteristics on needle motion

The subdivision of force acting on the needle leads us to presume that the geometry of protrusion might play a non-negligible role on the relationship between the axial and radial components of such a force. This hypothesis is further endorsed by the role played by the geometry of the needle protrusion, as emerged from Equation 2.1 and the related discussion.

In fact, in the light of Equation 2.1, it can be argued that several factors determine the needle acceleration over the ascending motion. Being as the off-axis motion is affected by needle lift, the arisen non-uniformity of the jets' development is believed to be determined also by the geometrical and mechanical characteristics of the injector. This prompts an experimental investigation addressed to assess the influence of the injector's characteristics; comparing the uniformity of the jets' development and injection delays at unvaried injection settings, and employing different injectors.

In this respect, it is well known that a piezo-electric injector works up to five times faster than a traditional solenoid-driven injector. The principles underlying the piezo injector indeed minimise the friction dramatically. In mechanical terms, at commencing injection, the needle experiences a more abrupt upward motion, thus minimising the detrimental impact of the off-axis motion. Accordingly, being as the needle is subjected to a more dramatic acceleration, a considerable contribution to the improvement of the hole-to-hole uniformity is provided.

Furthermore, along with fuel pressure within the control chamber, an additional contribution towards weakening the needle lift is given by the force arisen in response to commencing flow through the orifices, according to the following formula:

$$F \approx \rho \cdot \left(\frac{\pi\, d^2}{4}\right) \cdot U^2, \quad with\ U \approx \sqrt{\frac{2 \cdot (pINJ - BP)}{\rho}} \tag{4.8}$$

In the light of Equation 4.8, the orifice diameter affects this force, which exerts a curbing action on the needle-control piston assembly. Accordingly, in the case of a larger hole diameter, a slower flow is believed to occur, weakening the action of the force curbing the needle, to the advantage of the lift. The backpressure exerts a contrasting action on the flow through the orifice; this endorses the hypothesis that higher backpressure boosts needle lift. Hence, it can be argued that increasing backpressure and the ensuing flow slowdown mitigate the curbing effect on the needle lift.

4.5.3. Influence of fuel properties on needle radial motion

Equation 2.1 in Chapter 2 highlights the pivotal role of fuel properties, such as viscosity and density, on the characterisation of the injection process. Viscosity indeed determines shear stress on the needle, according to the formula:

$$\tau\text{shear} = \mu \cdot \frac{\delta U}{\delta y} \tag{4.9}$$

where τ, μ, U and y refer to the shear stress, fuel viscosity, the fluid velocity and coordinate, respectively (Figure 4.10).

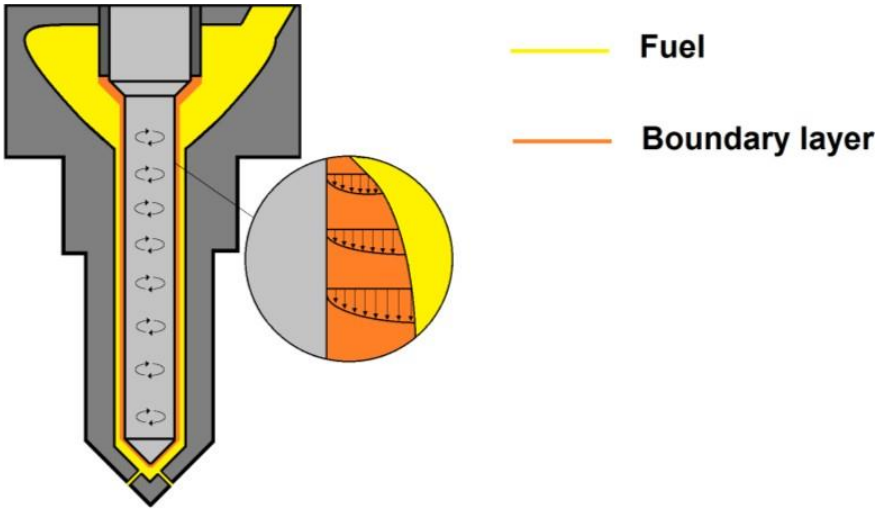


Figure 4.10. Lower viscosity implies weaker shear stress on the needle. As a consequence, needle oscillations are alleviated, minimising the imbalance of fuel flow through the orifices.

Hence, wider off-axis motion is expected to arise. This phenomenon may be also ascribable to the pressurised fuel flowing from the control chamber through the A-hole. Once the injector solenoid is energised, the valve ball is dragged up by the pilot-valve pin element, opening the A-hole through which the fuel flows from the control chamber. A dramatic pressure drop takes place within the control chamber, driving the lift of the control piston-needle assembly. Thereafter, the injection event commences. In the case of the MF30 injection, the higher viscosity curbs the flow through the A-hole if compared to the diesel case. The slower fuel flow, determined also by the greater MF30 density, softens the pressure drop within the

control chamber. Therefore, the control piston-needle motion is slower, prolonging the detrimental effect of the needle misalignment.

4.5.4. The impact of injection-induced pressure perturbation on needle radial motion

The unexpectedly greater uniformity of the MF50 plumes' velocity injections can be explained also by considerations drawn by Equation 3.6 in Chapter 3. As the injection starts, fuel flows through the orifices. Fuel pressure within the nozzle experiences a drop, arisen in response to the flow commencing. Bearing in mind the assumption of inviscid flow underlying Bernoulli's equation, greater density curbs the fuel velocity.

Additionally, even abandoning the assumption of inviscid flow, it is well known that higher viscosity slows fuel flow down, given the thicker boundary layer on the injector internal walls. As a result, the increase in fuel kinetic energy is alleviated, softening the pressure drop within the nozzle as well as the magnitude of the rarefaction wave stemming from the needle lift. Therefore, a weaker rarefaction wave causes the needle to be less perturbed, and a smaller misalignment ensues.

This interpretation explains the better uniformity of the plumes' velocity distribution exhibited by M50 injections. In this regard, besides the weaker rarefaction wave stemming from the needle lift, the MF50 density is presumed to effectively dampen needle misalignments due to shear stress; to the benefit of a reduction in the imbalance of the fuel flow.

In the light of this interpretation based on Bernoulli's equation, diesel is expected to show a worse uniformity in comparison with MF30. However, greater MF30 viscosity enhances the shear stress on the needle, promoting off-axis motion and worsening the uniformity of the plumes' velocity distribution. This aspect sheds light on the need for an assessment of the combined impact of viscosity, bulk modulus and density on the needle misalignments.

4.5.5. The competition between shear stress and orthogonal stress on the needle

The above considerations lead us to state that increasing viscosity worsens the orifice-to-orifice uniformity of the plumes' velocities. Accordingly, MF50 was expected to output the least distribution of the plumes' velocities. Nonetheless, the results emerging from the MF50 tests largely disagree with this assumption. Indeed, MF50 has greater density and viscosity with respect to MF30 and diesel. In mechanical terms, the dampening action of density on the off-axis motion is conceived to outweigh the effects of shear stress, generated by fuel viscosity.

Accordingly, the amplitude of needle wobbles is deemed to be appreciably governed by the competition between shear stress and orthogonal stress. Therefore, during needle lift, an imbalance of forces, acting on the needle, governs the uniformity of the plumes' velocity distribution. Thus, with the MF50 injections, the impact of shear stress is largely dampened by the action attributable to fuel density, lowering the standard deviations of PL velocities. In this respect, the results emerging from the MF50 injections leads us to presume that, beyond a certain limit, increasing viscosity and density might result in unexpected needle behaviour, affecting positively the imbalance of fuel flow. On the other hand, as it emerged from Tables 4.8 and 4.14, the largely greater viscosity and density than for diesel cancels the beneficial impact of increasing injection pressure at a higher backpressure. It is noteworthy that these results lie within the findings emerging from other studies.

Zhang *et al.* carried out an experimental investigation on the impact of fuel properties on needle off-axis motion via a high-speed X-ray imaging technique, employing diesel and biodiesel. **(86)** The tests revealed that biodiesel yields smaller needle oscillation if compared to diesel, due to high viscosity. Therefore, it could be stated that greater viscosity contributes to minimising needle oscillations underlying the imbalance of the injected flow rate.

By contrast, Torelli *et al.* conducted a numerical investigation of cavitation-induced hole-to-hole variation of injected flow rate, employing diesel and a gasoline-like fuel, referred to as SRG. **(90)** It was found that, in the case of diesel, the needle was subjected to wider oscillations if compared to the SRG case. Accordingly, it might be argued that fuel with greater viscosity and density promotes the needle's lateral motion, thus disagreeing with Zhang's findings.

Bearing in mind the findings emerging from this and the above studies, a ranking of fuels based on properties, such as density and viscosity, might prompt a physical interpretation of these results (Table 4.21).

Table 4.21. Fuel properties of fuel tested in this study and Zhang's research activity (T = 25° C)

Fuel	Kinematic viscosity (m^2/s)	Density (kg/m^3)	Dynamic viscosity (kg/m·s)
Diesel	$4.02 \cdot 10^{-6}$	827.41	0.0033
MF30	$4.10 \cdot 10^{-6}$	851.81	0.0035
MF50	$4.16 \cdot 10^{-6}$	868.07	0.0036
Biodiesel (**86**)	$5.4 \cdot 10^{-6}$	849.9	0.0046

In the light of the above rankings, it is expected that MF50 yields a worse uniformity of plumes' velocity than for diesel and MF30, given the greater viscosity. The greater density leads however to disagree with this conclusion. Therefore, a competition between shear stress, the magnitude of which is attributable viscosity, and dampening action determined by density, is believed to arise on the needle surface, governing the radial motion. In other terms, if viscosity and density values fall within certain limits, the favourable action of the higher injection pressure and greater backpressure on uniformity of the plumes' velocities is assured. Beyond certain ranges, it is conceivable that, if on one hand greater viscosity and density contribute to the minimisation of the non-uniformity of the jets' velocities, on the other the beneficial impact of increasing injection pressure at higher backpressure can deteriorate.

4.5.6. The assessment of injection delays

At unvaried injection settings, as expected MF-based blends were found to retard the injection

start in comparison with neat diesel. As mentioned above, greater fuel density curbs the fuel velocity. Besides greater density, higher viscosity provides a further contribution to fuel flow slowdown, given the more significant action of the boundary layer arising along the injector's internal walls.

As was expected, in most cases the MF50 injections showed the longest DOI (except for injection settings 400-20 bar, 700-20 bar and 1000-60 bar); whilst diesel exhibited the shortest DOIs (except for 1400-60 bar and 1400-80 bar).

The inconsistencies might be attributable to various phenomena, such as:

- injection-induced pressure fluctuations arisen in the rail;
- accentuation of internal frictions, engendering thermal effects within the fluid.

It is noteworthy that these incoherencies prompted the following chapter, which deals with the rail pressure fluctuations determining deviations from the expected injection characteristics.

4.5.6.1. The accentuation of internal frictions within fluid flow

With regard to the impact of the internal frictions on the DOIs, it could be argued that the combined increase in injection pressure with viscosity might explain some inconsistencies. In fact, the internal frictions within the fluid and along the orifice walls are promoted in the case of greater viscosity. Hence, appreciable thermal effects arise throughout the injection system, especially along the injector's walls. These thermal effects are believed to considerably preheat the fuel, leading to a local decrease in viscosity and density. Indeed, when MF50 injections were carried out, the microcontroller displayed temperatures spread out over a range from 30 °C to 54 °C. With regard to diesel and MF30 injections, the temperature ranged from 28 °C to 39 °C and 26 °C to 40 °C, respectively. As a consequence, when MF50 injections are executed an effective cooling system is required. Thus, some fluid particles might obtain greater velocity, determining the unexpected advance of the injection start. It

follows that an advanced appearance of the plumes' tips might be detected earlier than for less viscous fuels.

4.5.6.2. The impact of rail pressure fluctuations on DOIs

Diesel showed a longer DOI than for MF30 in some cases. Being as diesel is less viscous and dense than MF30 and MF50, the above thermal effects are deemed more negligible. Therefore, it is hypothesised that the longer DOIs are due to the damaging effect of injection-induced pressure fluctuations. Indeed, as the injector is triggered, the needle moves upward. A rarefaction wave is originated and travels towards the delivery chamber and the rail, where pressure fluctuations take place. These fluctuations are accentuated in the case of fuel with a low bulk modulus, as well as when consecutive shots are performed.

Additionally, from the bar chart in Figure 4.9, it can be seen that the diesel averaged DOIs are longer than those for MF30 at an injection pressure of 1400 bar, showing consistency with the findings related to the promoting action of higher injection pressure on diesel pressure fluctuations. Chapter 5 provides an accurate overview of this detrimental phenomenon, which underlies the observed inconsistencies. Diesel has the lowest bulk modulus. As such, it is characterised by a higher degree of unpredictability of the injection-induced pressure fluctuations.

Therefore, when the injector's solenoid is energised, diesel injection pressure differs from the set rail pressure. Accordingly, the injection pressure might be higher or lower than the set rail pressure, affecting the uniformity of the jets' development as well as the injection delays. This might explain the diesel DOIs, which are unexpectedly longer than for MF30 at injection settings of 1400-60 bar and 1400-80 bar. Similarly, MF30 has a lower bulk modulus than MF50. Hence, MF30 injections are more prone to be affected by injection-induced pressure fluctuations with respect to MF50. This might explain the inconsistencies at injection

configurations of 1000-60 bar, 400-20 bar and 400-40 bar.

4.6. Summary

Following on from the findings described in Chapter 3, a robust experimental campaign was undertaken focusing on the combined influence of injection settings with fuel properties on orifice-to-orifice variability in the plumes' velocities and injection delays. The experimental investigation was carried out to compare diesel and two furan-based blends (here referred to as MF30 and MF50, given the volumetric content of 30% and 50% 2-methylfuran in each blend, respectively). The results were analysed focusing on the impact of parameters, such as:

- fuel viscosity;
- fuel density;
- injection pressure;
- backpressure.

The following conclusions are summarised below.

Concerning the influence of the combined impact of fuel properties with injection settings on needle motions governing the hole-to-hole variability in plumes' velocity, it can be concluded that:

1. in the case of MF30 injections, given the larger standard deviations of the jets' velocities than for MF50 and diesel, it is presumable that the action attributable to fuel density does not suffice to dampen shear stress and is ascribable to viscosity and determining the needle's off-axis motion. In contrast, MF50 exhibits the lowest standard deviations, meaningful of a dampening action and attributable to density, which outweighs shear stress.

2. Diesel's standard deviations are positioned in the middle, indicating a more stable balance between these stresses acting on the needle.

3. Beyond certain ranges of density and viscosity, it is conceivable that the positive effect of increasing injection pressure on the uniformity of the plumes' velocities at greater backpressure might deteriorate.

With regard to the influence of injection settings with fuel properties on the DOI, it was seen as expected that at unvaried injection settings, diesel DOIs were the shortest, followed by MF30 and MF50. However, some inconsistencies were observed. More specifically:

4. MF50 exhibited a shorter averaged DOI than for MF30 in some cases. This might be ascribed to frictions arising within the fluid, engendering non-negligible thermal effects and a subsequent local decrease in viscosity and density; fluid flows more rapidly (but still slower if compared to diesel).

5. Diesel showed a longer DOI than for MF30 in some cases. Given the lowest viscosity and density, this incoherence cannot be attributed to thermal effects. It is hypothesised that longer DOIs are due to injection-induced pressure fluctuations, which lead the diesel injections to be performed at a lower or higher pressure than the set rail pressure, yielding unexpected results. As will be discussed in Chapter 5, these pressure fluctuations are particularly accentuated in diesel injections if compared to MF30 and MF50 cases.

In the light of these findings, MF50 and MF30-like biofuels, which do not belong to the furan family, may yield analogous results. Once this fuel has been found, additional tests would be necessary to verify that it yields analogous combustion characteristics and emissions. In fact, if on one hand equal viscosity and density are believed to provide analogous jets' development, they might not yield a similar combustion process, the characteristics of which are determined by other fuel properties. Additionally, greater viscosity of the furan-based blends improves the lubrication of the components compounding the injection system.

On the other hand, the components of a high-pressure pump are subjected to stronger stress, determining an increase in temperature throughout the layout of the injection system, and leading to considerable preheating of fuel. As a consequence, an effective cooling system is required. Moreover, greater viscosity, characterising the furan-based blends, may imply greater power consumption and a more frequent replacement of the high-pressure pump, especially in the case of higher injection pressures.

However, as seen from the MF50 tests, increasing viscosity and density benefit the uniformity of the jets' development, to the advantage of a more uniform distribution of the A/F ratio within the cylinder. Moreover, as widely discussed in Chapter 5, furan-based fuels are characterised by smaller rail pressure fluctuations if compared to diesel. This is meaningful of a minimised unpredictability of the time-history of rail pressure, to the benefit of the optimisation of the injection strategy, especially in the case of multiple injections.

In conclusion, taking into account the proven advantages in terms of emissions and combustion characteristics, the automotive industry is urged to find a trade-off solution, conciliating the above *pros and cons* related to the employment of furan-based blends.

CHAPTER 5

EXPERIMENTAL INVESTIGATION OF RAIL PRESSURE FLUCTUATIONS CORRELATED WITH INJECTION SETTINGS AND FUEL PROPERTIES

A substantial amount of this chapter has been presented at the SAE International 2020 Powertrains, Fuels and Lubricants Meeting (PF&L), a conference held on 22th - 23th September, 2020. The results have been published in the paper:

Coratella, C., Parry, L., & Xu, H. (2020). 'Experimental Assessment of the Impact of Fuel Properties on the Rail Pressure Fluctuations' (No. 2020-01-2122). *SAE Technical Paper*.

Following on from the publication of the paper, the results have been further analysed. The additional findings have been described in the manuscript:

Coratella, C., Parry, L., Li, Y., & Xu, H. (2021). 'Experimental Investigation of the Rail Pressure Fluctuations Correlated with Fuel Properties and Injection Settings'. *Automotive Innovation*, 4(2), pp 215-226.

These works have been here amended and written with the permission of all co-authors.

Introduction

In the light of the outcomes previously discussed, this chapter provides a further insight into the combined influence of injection settings and fuel properties on the characterisation of the injection process, focusing on the injection-induced pressure fluctuations within the rail. Similar to Chapter 4, the scope of this chapter falls within the need for the assessment of the

potentialities of MF-based blends, which represent an attractive candidate to supersede their fossil counterparts.

5.1. Injection-induced pressure fluctuations

The widespread introduction of electronically managed injection is mainly due to the flexibility and fast response of the injection components. Such a technology has been indeed demonstrated to appreciably improve the accuracy of the injected fuel amount, so as to smoothen the combustion process and increase thermal efficiency. Nonetheless, additional refinements on modern engines have been demanded by the stringent emission legislation. This has led to the design of the *MultiJet* system, which assures considerably faster injector actuations, enabling the injection cycle to be split up into eight separate shots. However, the fast dynamics of CR components, such as the piezo-injectors, accentuate pressure perturbations within the injection system. This gives rise to the greater injection-induced pressure fluctuations. In the light of Chapters 3 and 4, along with the fuel properties, these pressure fluctuations are supposed to play a pivotal role in the hole-to-hole non-uniformity of the jets' velocities. Therefore, an investigation of the impact of injection settings and fuel properties on the injection-induced pressure fluctuations is needed. This scope lies within the trend followed by the automotive field, in searching renewable sources of energy prompts to assess the impact of biofuels' properties on the characterisation of the injection process.

5.1.1. Literature review of injection pressure fluctuations

As the injection commences, the needle lift gives rise to a rarefaction wave travelling from the nozzle towards the rail. **(50, 57, 73-74)** A wide range of literature has demonstrated that injection-induced pressure fluctuations lead to the shot-to-shot variability underlying the deviations from the expected mass flow rate. **(50, 52, 57, 119-121)** Additionally, it is well known that also the stroke by stroke motion of the pump significantly contributes to rail

pressure fluctuations. This framework has driven the research community to develop several predictive models and devices to control or even compensate for rail pressure oscillations.

A thorough insight into the impact of injection-induced pressure oscillation on the CR hydraulic system was provided by Catania *et al.*, who designed a zero-dimensional mathematical model allowing the investigation of the highly unsteady wave propagation taking place in the CR system. **(50)** The model revealed that the influence of injection pressure fluctuations on the injected fuel volume is significantly determined by dwell time between consecutive injections. The study investigated also the relation between the period of the system's free oscillation and the energising time, giving rise to hydraulic resonance in the nozzle. The hydraulic frequency was compared to the natural frequencies of the CR layout's components, so as to single out possible mechanical resonance conditions which might accentuate the deviations from the expected injected fuel rate.

Catalano *et al.* developed a CFD code for simulating the unsteady flow in the pipes of the CR layout. **(51)** The CFD code was validated by a comparison with the experimental data. The main finding consisted of the demonstration that the reduction in injection pressure over a split injection cycle is mainly ascribable to dynamical effects, rather than to friction losses. This may lead to discourage all attempts to minimise the friction losses, which are commonly deemed the main factor responsible for the decrease in injection pressure. As such, this study suggests investigating the chance of exploiting the inertial effects, so as to trigger the injector when injection pressure is greater than the set pressure. The proposed CFD code indeed highlights the feasibility of exploiting the overpressure wave engendered by suddenly stopping the fuel flow through a dedicated acceleration branch. This solution is believed to recover pressure drop and even to overcome the set rail pressure.

In the wake of Catalano's findings, Amirante *et al.* conducted a research study addressed to analyse the dynamical effects taking place in the pipes of a CR system, focusing on the use of fast-response pressure sensors for the detection of the instantaneous fuel pressure in different sections. **(52)** This approach was applied both on single injections and on multiple injections, concluding that the second shot should be set before pressure reaches its peak, so as to exploit the compression wave reaching the nozzle. This study included also the assessment of the influence of a transducer on pressure detection. More specifically, a comparison between the pressure history computed without the pressure transducer and that computed with its presence was carried out. It emerged that the transducer affects the detection of pressure in various sections of the CR layout, particularly in the vicinity of the nozzle.

Beierer *et al.* designed a numerical model of a commercial CR system developed in the GT-FUEL (Gamma Technologies, Inc.) software environment. **(55)** The investigation demonstrated that pressure fluctuations are meaningfully determined by injection pressure, injection duration, and connection pipe geometry. It emerged that the minimisation of pressure variation is achievable via shorter injection duration combined with lower injection pressure. A further mitigation is obtainable via a larger diameter and shorter length of the supply pipe. Shortening the pipe thereby resulted in a smaller amplitude of pressure fluctuation; whilst an increase in the connection line diameter was found to be more advantageous for short injection periods and high injection pressures. However, the advantage of the reduced pressure variation from shortening the connection pipe was found to be minimised by setting a lower injection pressure and a longer injection time. In view of further decreased pressure fluctuations, these peculiarities are marked by the fact that geometrical characteristics of the system might be less binding if compared to other parameters affecting injection pressure fluctuations.

In the wake of previous work, Catania *et al.* proposed also an overall model predicting the dynamical effects and pressure wave propagation, taking:

- the thermo-fluid dynamics of hydraulic components;
- the mechanics of CR hydraulic components;
- the electromagnetics of the injector solenoid

into account. **(57)** Focusing on wave propagation, it was demonstrated that the high-frequency oscillations are mainly caused by the impulsive dynamics, typical of CR systems.

Similarly to Beierer, Pontoppidan *et al.* assessed pressure fluctuations arising at the injector's inlet, focusing on their impacts on the mixture preparation and spray stability. **(120)** The research activity was purposed to single out the areas where pressure oscillations arise, so as to assess the influence on the A/F ratio distribution and combustion efficiency. The experimental campaign was conducted employing an injector test bench provided with a backpressure vessel. Varying injection pressure was observed to determine the combustion behaviour, evidencing that pressure oscillations upstream of the nozzle hinder the spray stability. On the other hand, increasing the number of split injections was found to soften the influence of pressure fluctuations on spray stability.

Injection pressure oscillation was also explored by Herfatmanesh *et al.*, who conducted an experimental study employing a 2.2-L four-cylinder four-valve turbocharged diesel engine. **(121)** Rail pressure fluctuations were assessed via two approaches; firstly based on the fixed pulse width, and subsequently on the fixed fuel delivery amount. At various engine speeds and unvaried injection pulse, it was found that varying the interval between the pilot and main injections leads to oscillation of the fuel delivery amount. Similarly, the oscillating pulse width arises if the fuel delivery amount is set. Therefore, it was inferred that pressure waves

underlie fluctuations of the injected fuel rate, affecting adversely the mixture preparation and the pollutants' emissions.

A further contribution was provided by Ubertini, who developed a multidimensional code to simulate pressure pulsations taking place upstream of the CR injector nozzle. **(122)** More specifically, numerical simulations of a 3D virtual spray injected into a vessel revealed the significant role of injection pressure fluctuations in the injected flow rate and spray characteristics. It emerged also that higher injection pressures lead to a larger amplitude of fluctuations. The main peculiarity of the physical model with respect to conventional 1D/3D coupling consists of its easy implementation. The computational cost was indeed found to be negligible with respect to the 3D thermofluidic dynamics' simulation. On the other hand, this implied that the modelling approach is not able to predict the small oscillations' amplitude.

De Risi *et al*. carried out an experimental investigation, from which emerged the sensible impact of injection pressure fluctuations on soot and NO_X emissions when a multiple injection strategy is performed. **(123)** The study includes the assessment of the exhaust gas, employing in-cylinder combustion images and two fuel ducts of different lengths. The shorter duct was found to engender a pressure peak during the main injection; whilst the longer duct generates a pressure valley. More specifically, the 0.37-m duct exhibits more stable pressure behaviour as a result of the main injection if compared to a 0.74-m pipe. The analysis of the combustion images' output results in agreement with the findings which emerged from the exhaust gas assessment; confirming the impact of injection pressure fluctuations on the pollutants' emission.

In order to obtain a fast-tracking performance, Hong *et al.* designed a robust control algorithm for light-duty diesel engines based on an empirical model, representing the physical relationship between the current driving the pressure control valve and rail pressure. **(124)** In

particular, the rail pressure and the driving current of the pressure control valve were set as a performance variable and a control input, respectively. In order to compensate for the modelling error of the algorithm, an integral feedback action was included. Afterwards, the rail pressure control algorithm was validated through a comparison with experimental data, revealing an accurate tracking performance and robustness with 0.3 seconds of settling time.

Wang *et al.* proposed a mathematical model aimed to control rail pressure. **(125)** The model was implemented in MATLAB/Simulink and included three subsystems, standing for the high-pressure pump, rail and injector. The outcomes were validated by a comparison with both the professional CR system model implemented in AMESim and with a PID controller. From the comparison, it emerges that the model excels for overshoot, fast tracking and reducing fluctuations of rail pressure.

Likewise, Gupta *et al.* designed a model predicting rail pressure oscillations. **(126)** An angle-varying internal model was implemented in an AMESim environment, taking the periodic dynamics of the incoming and outgoing flows into account. In particular, the dynamics of the rail pressure were represented in the rotational angle domain, which is periodic due to the stroke by stroke motion of the pump and the injection event occurring on an angular basis. The model is based on the one-dimensional flow equations and was demonstrated to be able to capture rail pressure pulsations. This peculiarity enables the identification of the location where the actuator can be installed for an effective action, compensating for or even suppressing rail pressure pulsation.

Besides the investigation of parameters governing injection pressure fluctuations, several devices have been designed to regulate or even suppress the fuel pressure pulsation occurring at the injector inlet and within the rail. **(127-133)**

5.1.2. The state of the art of MF-based blends

Chapter 4 provides a detailed literature review concerning MF-based blends.

5.1.3. The proposed study

This framework prompted the author to undertake a robust experimental campaign of injection tests employing different fuels, such as diesel and 2-MF/diesel blend, under various injection scenarios. Besides the injection setting, this study identifies:

- viscosity;
- density;
- bulk modulus;
- surface tension

as key parameters for an accurate characterisation of rail pressure fluctuations. This work is justified also by the need to assess the unpredictability of those fluctuations. As stated by Catalano *et al.*, this may lead us to suppose that the injection strategy should be set, enabling the injector triggering as injection pressure exceeds the set rail pressure in favour of jet penetration length and break-up timing. Additionally, the previous chapters shed light on the role of higher injection pressures and backpressures benefiting the uniformity of jets' velocities. Therefore, once the time-history of rail pressure was plotted, it is necessary to acquire the time required by fuel pressure to retrieve or even exceed the value preceding the shot, so as to trigger the injector at a more convenient timing. Moreover, the paucity of data concerning the injection of MF-based bends has prompted this stage of the thesis' work.

The chapter is outlined as follows. Section 5.2 describes the test facilities, followed by section 5.3 describing the calculation of fuel blend properties. The tests and analysis of the results are fully discussed in section 5.4 and 5.5, respectively. Section 5.6 provides further physical explanations of the findings. The conclusions are summarised in section 5.7.

5.2. Test facilities

In order to assess the combined impact of injection settings and the fuel properties on rail pressure fluctuations, the CR test rig in the Department of Mechanical Engineering at the University of Birmingham was employed. The set-up of the rig does not differ from the one employed for the assessment of the needle lift sensor. However, because of the purpose of this research, the CR injector was deprived of the needle lift sensor. Figure 5.1 shows the injector mounted on the high-pressure vessel.



Figure 5.1. The CR injector is mounted perpendicularly onto the flanged top of the high-pressure vessel

The rail is provided with a fuel pressure sensor, manufactured by Bosch and designed to detect pressures up to 1500 bar. The sensor has an accuracy range of 1.5% at full scale and a response time of 2 ms. The pressure sensor is connected to an oscilloscope, which enables the visualisation of the time-history of the rail pressure. In order to visualise the current profile driving the injector, the oscilloscope is connected also to the injector solenoid.

5.3. Calculation of fuel blend properties

Table 5.1 provides the bulk modulus of diesel and 2-MF. Along with the fuel properties listed in Table 4.1, bulk modulus is indeed deemed to significantly determine pressure oscillations.

Table 5.1. The bulk modulus of the fuels constituting the blends

Fuel	Bulk modulus (MPa)
2-MF	1958.41 - 2071.65
diesel	1545

Bearing in mind that the temperatures detected here range from 30 ºC to 55 ºC, the diesel viscosities were obtained according to the correlation found by Wang *et al.* **(101)** The densities were calculated on the basis of findings achieved by Esteban *et al.* **(116)** Concerning the 2-MF, Jezak *et al.* demonstrated that temperature exerts a noticeable impact on the MF density. **(117)** The study includes also the calculation of the speed of sound across the MF-based fuels at various temperatures. For the purpose of this study, the estimation of the bulk modulus is approximately achievable via the formula:

$$c \approx \sqrt{\frac{K}{\rho}} \tag{5.1}$$

with c, K and ρ being the speed of sound, bulk modulus and density, respectively. In this regard, it is merely inferred that greater bulk modulus promotes wave propagation. **(134)** Table 5.1 enables the calculation of the properties of the MF-based blends. In this respect, the previous chapter provides an accurate review of the methods calculating the overall viscosity and density of the liquid blends.

5.4. Experimental tests

In order to analyse rail pressure fluctuations, a comprehensive investigation was conducted. For consistency, the tests were performed at the injection configurations set for the assessment of the sensor and the investigations of the variability of the jets' velocities. Figures 5.2-5.5 depict the curves plotting the time-history of the rail pressure and the current

profile related to a series of four consecutive injections. The red line refers to MF30, whilst the green and blue lines stand for MF50 and diesel, respectively.

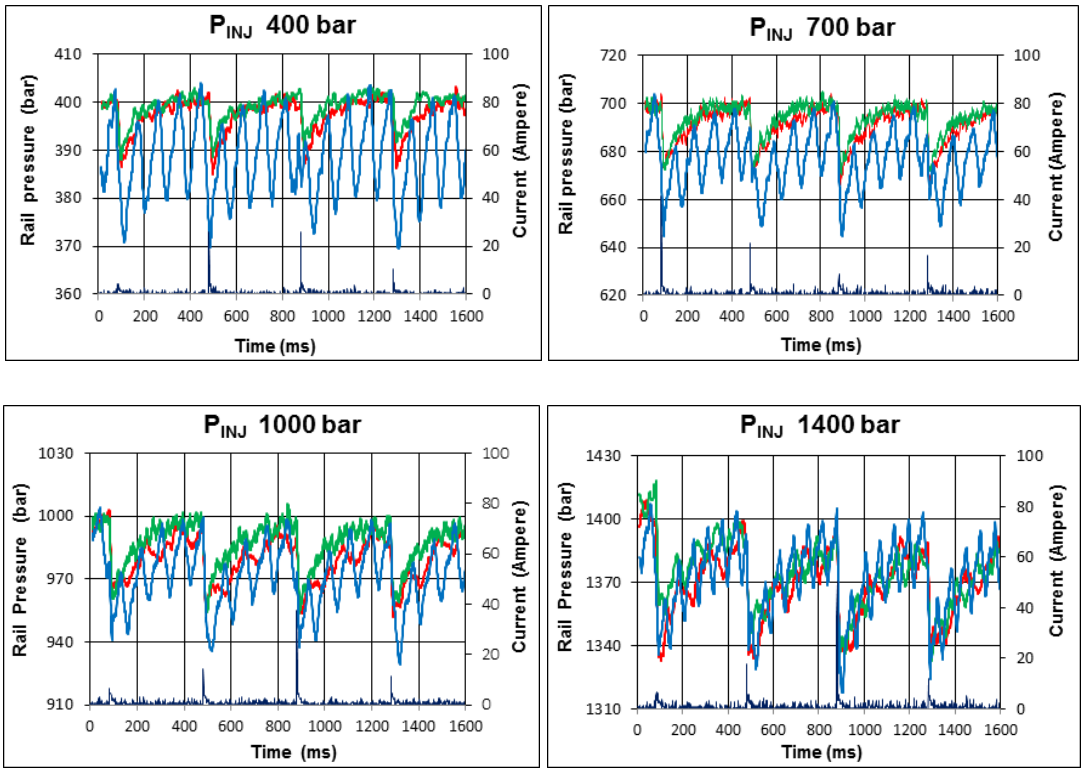


Figure 5.2. The time-history of rail pressure at various injection pressures and a backpressure of 20 bar

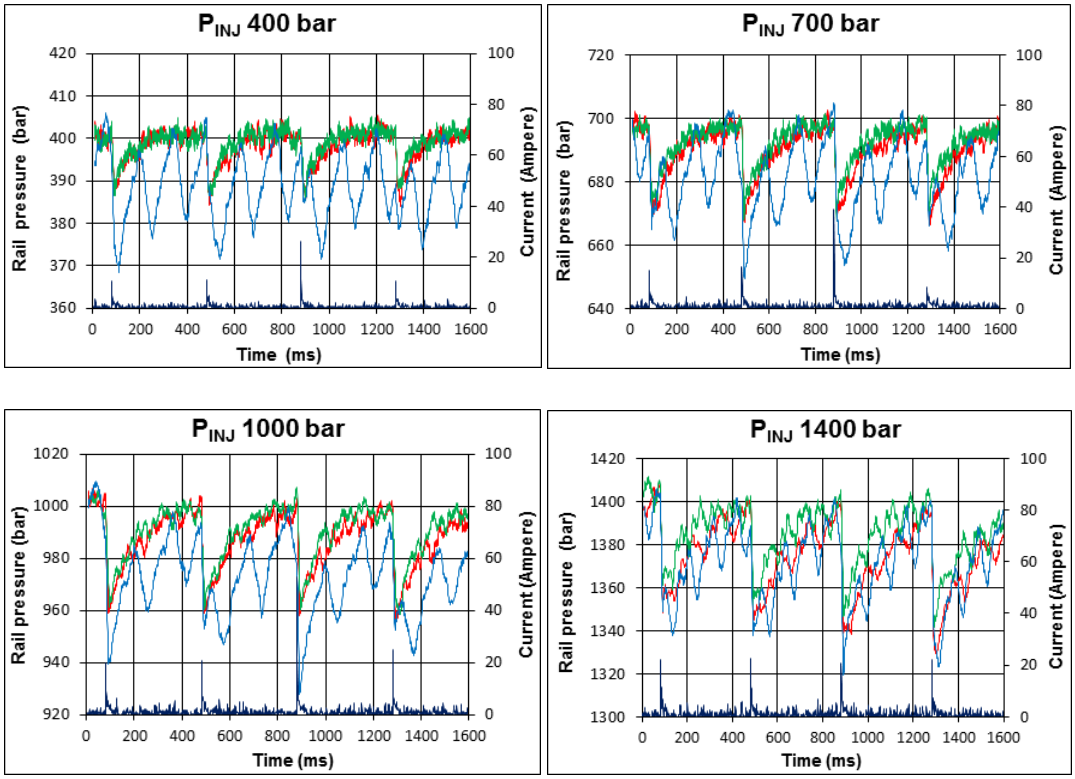


Figure 5.3. The time-history of rail pressure at various injection pressures and a backpressure of 40 bar

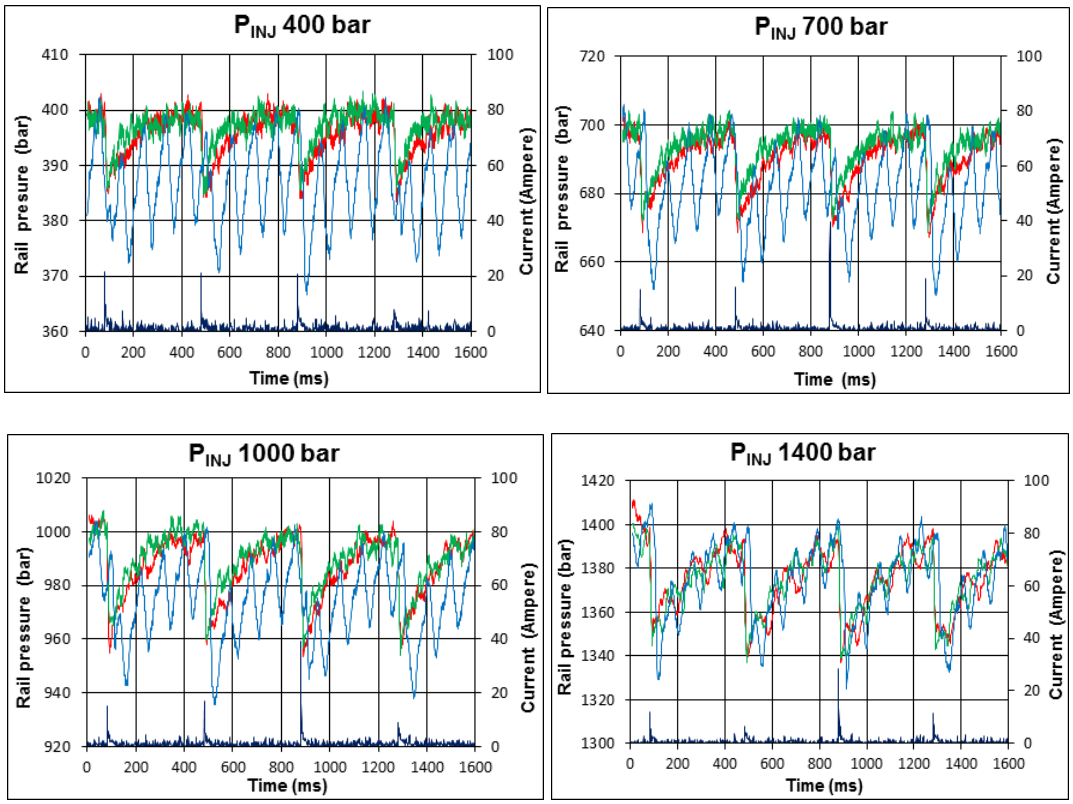


Figure 5.4. The time-history of rail pressure at various injection pressures and a backpressure of 60 bar

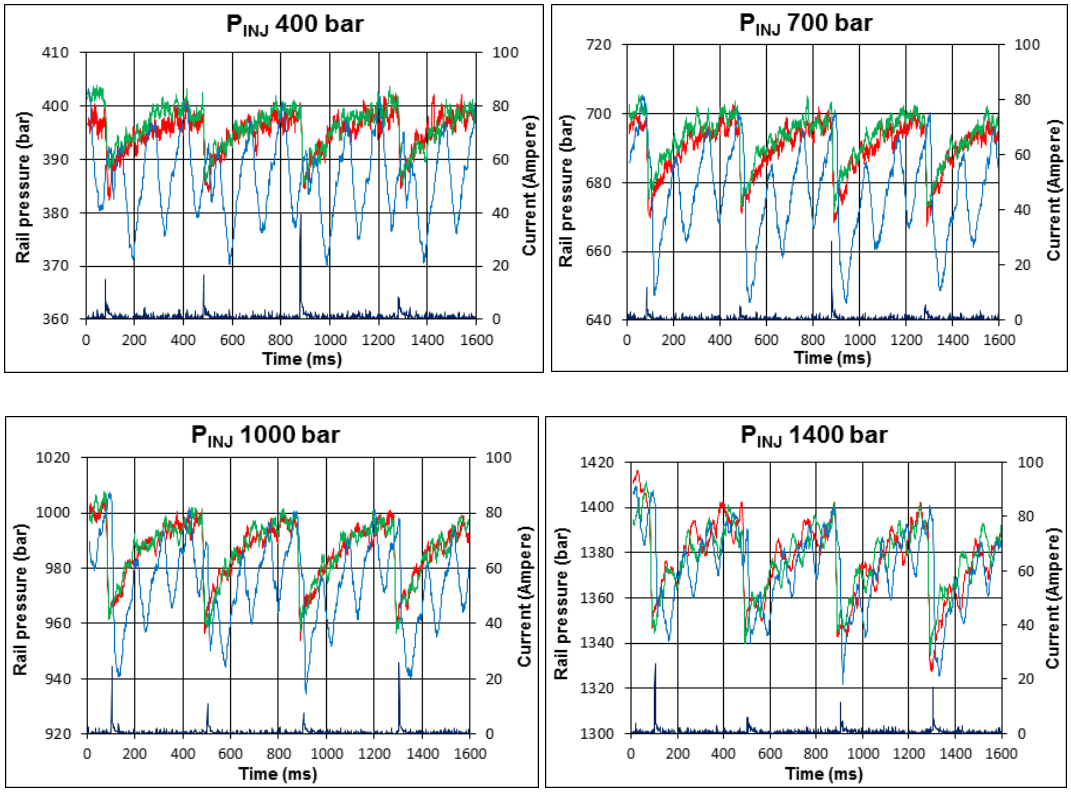


Figure 5.5. The time-history of rail pressure at various injection pressures and a backpressure of 80 bar

As expected, higher injection pressures accentuate pressure drop, which was revealed to vary with the fuel characteristics. The curves reveal also that as the injection commences, fuel pressure is firstly subjected to a steep drop, followed by an increase, until it stabilises around the set rail pressure. Furthermore, the time interval between the lowest pressure and the one preceding the shot is observed to vary both with injection settings and with fuel properties. Moreover, a discrepancy between the set energising time and the current duration energising the injector is observable. This phenomenon is believed to be due to the on-board capacitors, which are charged with current over a set period before discharging at a higher current for a shorter period. The findings are fully discussed in section 5.5.

5.5. Analysis of the findings

The following paragraphs provide an accurate explanation of the findings, singling out:

- pressure drop stemming from needle lift;
- the retrieving time, namely the time interval between the lowest pressure and the one preceding the following shot;
- the amplitude of rail pressure fluctuations;
- the time between two consecutive pressure peaks during the increasing stage

as the key characteristics describing the dynamical effects in the rail.

5.5.1. The assessment of rail pressure drops

According to Catania *et al.* **(50, 57)**, once injection commences, the delivery chamber and rail experience different fuel pressure variations. As shown by Figure 1.8 in Chapter 1, a sketch of the sectional view of a diesel injector, the needle and control piston keep in contact over the injection event. As such, the needle and control piston are assumed to constitute a system assembly; its motion being governed by the fuel pressure acting on top of the control piston and the needle protrusion. Fuel pressure on the needle causes the upward motion, determining the injector opening; whilst fuel pressure on the control piston top pushes the

assembly downwards in the closing direction. At the stand-by configuration, the second force prevails, since the rail delivers the pressurised fuel flowing into the control chamber through the *Z*-hole. Once the solenoid is energised, the ball valve is dragged up by the anchor pin valve, allowing the fuel to flow across the *A*-hole. Hence, a dramatic reduction in pressure occurs within the control chamber. The upward motion of the needle-control piston assembly ensues, thanks also to fuel pressure acting on the needle. As a consequence, the injection commences.

However, the reduction in control chamber volume, stemming from the assembly lift, gives rise to a compression wave, which is conveyed to the rail. Additionally, the steep reduction in fuel pressure, caused by needle lift, generates a rarefaction wave propagating through the supply duct towards the rail. Due to the difference in path lengths, the compression wave precedes the rarefaction wave. **(50, 57)** Moreover, it must be kept in mind that, once the rarefaction wave reaches a changing section, it gives rise to a reflecting compression wave, which travels back to the delivery chamber.

These wave phenomena are the main factors responsible for the difference between the pressure variation in the nozzle and the one taking place in the rail. Tables 5.2-5.4 list the rail pressure drops detected for all tested fuels at each injection configuration.

Table 5.2. Diesel pressure drops (in bar) arising after the start of injection

	1st Shot	2nd Shot	3rd Shot	4th Shot	Average	Error
400 – 20 bar	32	33	28	33	30.6	2.5
700 – 20 bar	59	48	56	50	53.6	5.5
1000 – 20 bar	63	65	60	67	63.4	3.5
1400 – 20 bar	72	85	65	65	69.8	10
400 – 40 bar	37	34	28	22	31.4	7.5
700 – 40 bar	32	52	51	34	44.2	10
1000 – 40 bar	70	46	72	55	62.6	13
1400 – 40 bar	68	62	80	77	69.6	9
400 – 60 bar	25	26	34	30	29	4.5
700 – 60 bar	52	50	47	52	48.2	2.5
1000 – 60 bar	62	66	57	59	62.8	4.5
1400 – 60 bar	80	65	78	60	71.8	10
400 – 80 bar	22	30	30	30	27.4	4
700 – 80 bar	58	55	56	51	53.6	3.5
1000 – 80 bar	67	55	66	57	59.4	6
1400 – 80 bar	69	50	78	75	67.4	14

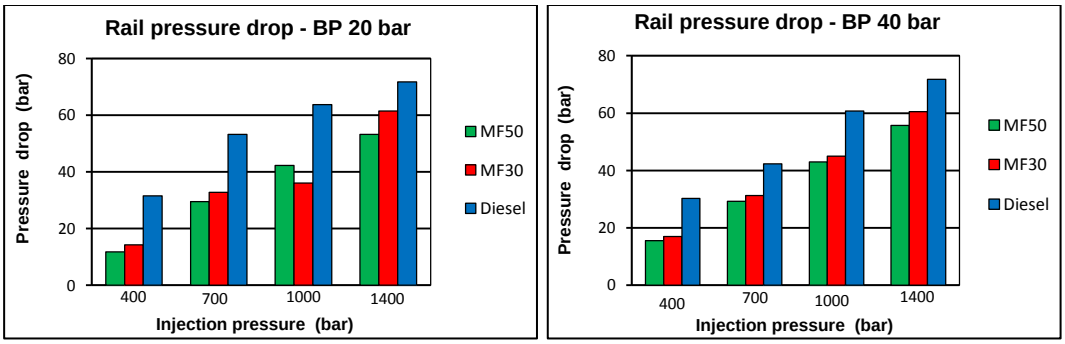
Table 5.3. MF30 rail pressure drops (in bar) arising after the start of injection

	1st Shot	2nd Shot	3rd Shot	4th Shot	Average	Error
400 – 20 bar	13	17	12	15	14.2	2.5
700 – 20 bar	30	31	35	35	32.8	2.5
1000 – 20 bar	38	35	35	36	36.8	1.5
1400 – 20 bar	66	68	60	52	61.8	8
400 – 40 bar	14	19	16	19	17.2	2.5
700 – 40 bar	28	34	30	33	31.4	3
1000 – 40 bar	45	45	45	45	45	0
1400 – 40 bar	60	54	63	65	61.4	5.5
400 – 60 bar	16	17	16	17	16.8	0.5
700 – 60 bar	28	27	28	32	29.4	2.5
1000 – 60 bar	50	42	48	47	46.6	4
1400 – 60 bar	50	54	58	58	56	4
400 – 80 bar	17	15	15	17	16.8	1
700 – 80 bar	29	28	30	31	29.2	1.5
1000 – 80 bar	40	44	42	41	42.4	2
1400 – 80 bar	70	60	60	70	63	5

Table 5.4. MF50 rail pressure drops (in bar) arising after the start of injection

	1st Shot	2nd Shot	3rd Shot	4th Shot	Average	Error
400 – 20 bar	12	12	13	10	11.4	1.5
700 – 20 bar	28	30	30	30	29.4	1
1000 – 20 bar	38	45	46	40	41	4
1400 – 20 bar	58	47	60	48	54	6.5
400 – 40 bar	16	16	16	14	15.6	1
700 – 40 bar	27	32	30	28	29.4	2.5
1000 – 40 bar	42	40	48	42	42.8	4
1400 – 40 bar	50	50	58	65	58	7.5
400 – 60 bar	14	15	14	15	14.6	0.5
700 – 60 bar	28	29	28	31	28.8	1.5
1000 – 60 bar	43	42	44	43	41.8	1
1400 – 60 bar	50	52	60	58	55.8	5
400 – 80 bar	14	17	15	16	15.2	1.5
700 – 80 bar	26	29	30	27	28.4	2
1000 – 80 bar	46	42	39	40	41.4	3.5
1400 – 80 bar	65	62	58	68	60.6	5

Figure 5.6 illustrates the bar charts referring to pressure drops averaged over four injection shots. The diagrams mark the dependence of pressure drop on the fuel properties.



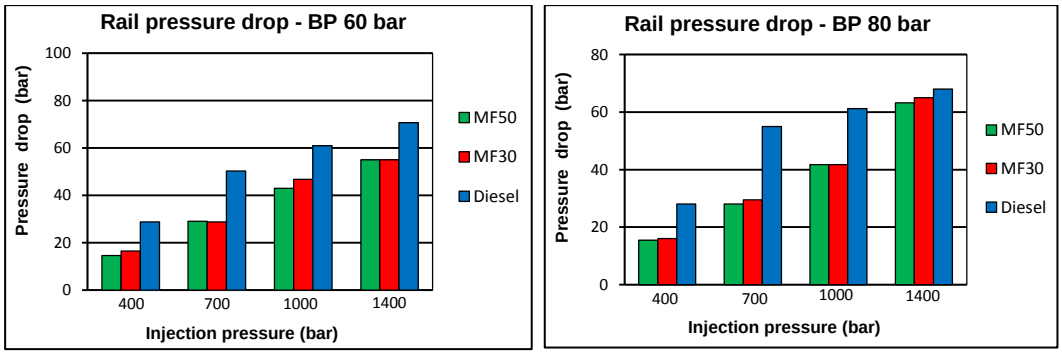


Figure 5.6. The averaged reductions in rail pressure, arising after the injection start, at each of 16 injection settings

As expected, increasing density is revealed to alleviate pressure drop induced by the commencing injection. These findings can be explained by Bernoulli's equation, which describes the inviscid fluid flow. Greater injection pressure indeed boosts fluid velocity, according to the formula:

$$U \approx \sqrt{\frac{2 \cdot (P_{inj} - BP)}{\rho_{FUEL}}} \tag{5.2}$$

where U, P_{inj}, BP and ρ stand for fuel velocity, injection pressure, backpressure and fuel density, respectively. Decreasing density thereby results in greater fuel velocity, which in turn implies greater pressure drops.

However, even abandoning the assumption of inviscid flow, these results can be explained by the influence of viscosity on the fuel flow through the injector orifices. Indeed, it is well known that, on equal injection settings, lower viscosity promotes the velocity of the fuel flow through the holes. **(43, 101)** This is mainly due to the smaller boundary layer, which accentuates the velocity gradient (Figure 5.7).



a) ***b)*** ***c)***

Figure 5.7. Lower viscosity *(a)* results in a less thick boundary layer. This minimises the impact of the friction losses at the nozzle walls, boosting fuel flow velocity. By contrast, greater viscosity slows down fuel flow *(b)*, because of accentuated friction at the orifice walls *(c)*.

As a consequence, greater fluid velocity engenders a larger pressure drop in the nozzle. By contrast, higher viscosity accentuates the boundary layer arisen at the orifice walls, to the detriment of the velocity gradient. Therefore, MF50 fuel flow is characterised by the accentuation of the energy dissipation, which results in the slowest fuel motion alleviating a pressure drop in comparison with diesel and MF30. Additionally, it can be observed that, along with injection pressure, backpressure plays a pivotal role in determining the injection-induced pressure drop. An accurate explanation is provided in section 5.5.3.

5.5.2. Analysis of rail pressure fluctuations

From the curves, it emerges that the initial dramatic pressure drop is followed by an increasing trend, until it approaches the value preceding the occurred injection. The increasing trend is observed to vary with the fuel properties and injection settings.

5.5.2.1. Analysis of the retrieving time

Tables 5.5-5.7 list the so-called *retrieving time*, namely the time required by the rail pressure to retrieve the set value. In other terms, the retrieving time is an interval measured between the timings corresponding to the lowest pressure and the pressure preceding the injection start.

Table 5.5. Time required (in ms) by diesel rail pressure to return to set rail pressure

	1st Shot	2nd Shot	3rd Shot	4th Shot	Average	Error
400 – 20 bar	230	250	300	250	257.5	35
700 – 20 bar	320	320	310	340	322.5	15
1000 – 20 bar	380	320	310	310	330	35
1400 – 20 bar	350	500	500	350	425	75
400 – 40 bar	250	250	230	140	217.5	55
700 – 40 bar	350	250	260	320	295	50
1000 – 40 bar	250	350	370	300	317.5	60
1400 – 40 bar	340	400	390	320	362.5	40
400 – 60 bar	220	250	250	220	235	15
700 – 60 bar	230	240	280	330	270	50
1000 – 60 bar	220	320	350	320	302.5	65
1400 – 60 bar	350	380	330	330	347.5	25
400 – 80 bar	250	250	250	250	250	0
700 – 80 bar	340	350	340	350	345	5
1000 – 80 bar	335	325	290	315	316.25	22.5
1400 – 80 bar	350	360	380	380	367.5	15

Table 5.6. Time required (in ms) by MF30 rail pressure to return to set rail pressure

	1st Shot	2nd Shot	3rd Shot	4th Shot	Average	Error
400 – 20 bar	200	250	200	200	212.5	25
700 – 20 bar	220	300	250	250	255	40
1000 – 20 bar	250	280	300	300	282.5	25
1400 – 20 bar	370	400	350	290	352.5	55
400 – 40 bar	110	130	160	100	125	30
700 – 40 bar	350	250	260	250	277.5	50
1000 – 40 bar	330	280	260	320	297.5	35
1400 – 40 bar	370	380	350	320	355	30
400 – 60 bar	160	160	180	180	170	10
700 – 60 bar	250	260	300	250	265	25
1000 – 60 bar	220	260	240	290	252.5	35
1400 – 60 bar	300	300	380	370	337.5	40
400 – 80 bar	250	260	250	160	230	50
700 – 80 bar	300	330	320	340	322.5	20
1000 – 80 bar	280	320	320	310	307.5	20
1400 – 80 bar	300	380	350	310	335	40

Table 5.7. Time required (in ms) by MF50 rail pressure to return to set rail pressure

	1st Shot	2nd Shot	3rd Shot	4th Shot	Average	Error
400 – 20 bar	130	150	100	90	117.5	30
700 – 20 bar	160	210	200	250	205	45
1000 – 20 bar	160	250	200	250	215	45
1400 – 20 bar	300	300	350	280	307.5	35
400 – 40 bar	120	120	100	100	110	10
700 – 40 bar	240	220	180	250	222.5	35
1000 – 40 bar	210	260	210	250	232.5	25
1400 – 40 bar	210	280	200	350	260	75
400 – 60 bar	160	130	100	150	135	30
700 – 60 bar	220	200	180	220	205	20
1000 – 60 bar	210	220	210	300	235	45
1400 – 60 bar	350	380	320	250	325	65
400 – 80 bar	160	260	280	200	225	60
700 – 80 bar	200	260	220	250	232.5	30
1000 – 80 bar	340	310	290	260	300	40
1400 – 80 bar	320	300	350	300	317.5	25

In order to represent the observations in a coherent manner, the following bar charts refer to the averaged *retrieving times*.

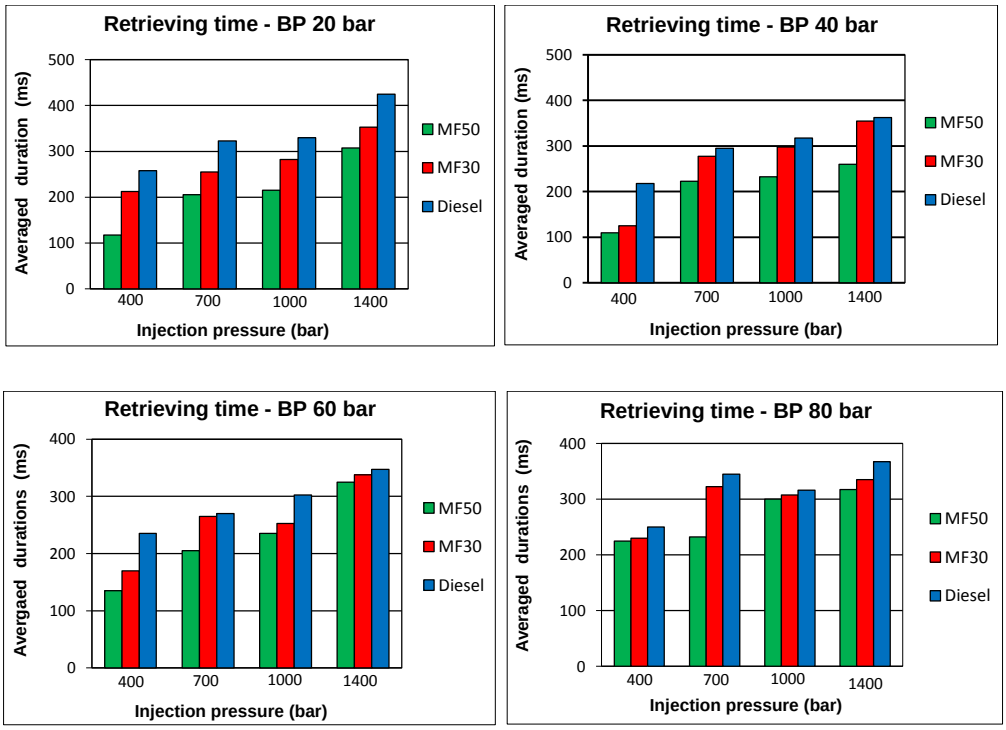


Figure 5.8. The averages of time required by rail pressure to recover the value preceding the previous injection shot

It emerges that the time interval varies with the fuel properties, and particularly with MF50 injections, they exhibit shorter retrieving times in most cases. Similar to the rail pressure drop, backpressure is observed to exert a non-negligible role on the retrieving time. The reasons underlying this finding are fully described in section 5.5.3.

5.5.2.2. Analysis of amplitudes characterising rail pressure oscillations

Over the retrieving time, rail pressure is subjected to a series of smaller oscillations, the amplitude of which depends on the fuel properties and injection settings (Figure 5.9).

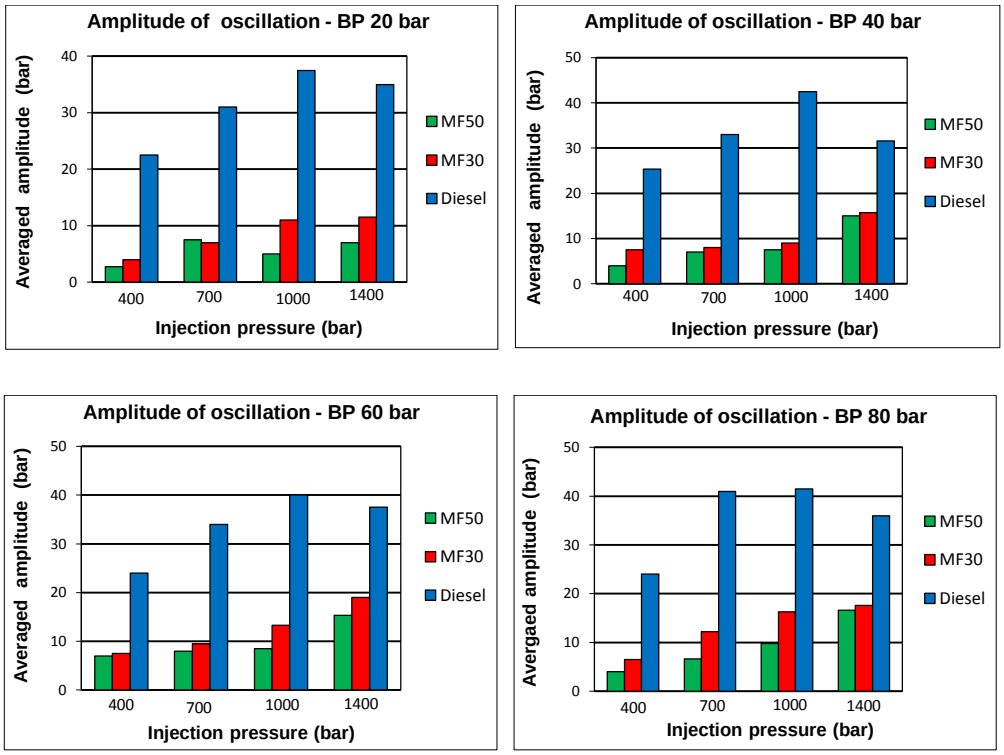


Figure 5.9. The averaged amplitudes of rail pressure fluctuations at various injection pressures and backpressures

As expected, the averaged amplitude is strongly correlated with the fuel properties.

5.5.2.3. Analysis of time interval between injection pressure peaks

Figure 5.10 shows the bar charts referring to the averaged time interval between two consecutive pressure peaks, providing an indication of the pressure pulsations' frequency. In this regard, a spectral analysis of the pressure trace should be performed, in order to extract the dominant frequency.

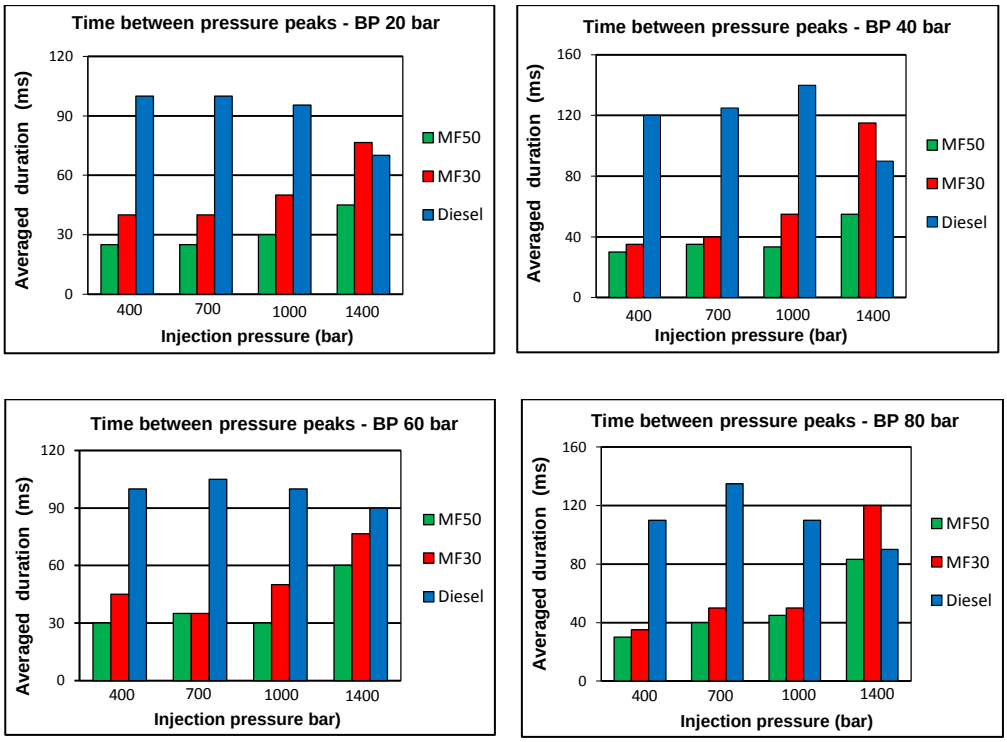


Figure 5.10. Time interval between two consecutive pressure peaks, at various injection pressures and backpressures

Diesel is seen to experience the largest amplitude of rail pressure and the longest time between two consecutive pressure peaks. By contrast, adding MF to the blend composition contributes to the reduction in amplitude as well as to the decrease in the time interval. However, Figure 5.10 exhibits some inconsistencies at injection settings of 1400-20 bar, 1400-40 bar, and 1400-80 bar. Indeed, MF30 rail pressure is seen to require a longer time than diesel. This might be ascribed to pressure instability, which is enhanced by the combined influence of the lowest bulk modulus with higher injection pressure.

5.5.3. The influence of backpressure on rail pressure fluctuations

The reasons underlying the non-negligible role of backpressure on pressure drop and retrieving time are explained in the following sub-sections.

5.5.3.1. The influence of backpressure on rail pressure drop

Tables 5.8-5.10 show pressure drops averaged over four injections and refer to the bar charts illustrated in Figure 5.6.

Table 5.8. Rail pressure drops (in bar) induced by diesel injection at various injection scenarios

	400 bar	**700 bar**	**1000 bar**	**1400 bar**
20 bar	30.6	53.6	63.4	69.4
40 bar	31.4	44.2	62.6	69.6
60 bar	29	48.2	62.8	71.8
80 bar	27.4	53.6	59.4	67.4

Table 5.9. Rail pressure drops (in bar) induced by MF30 injection at various injection scenarios

	400 bar	**700 bar**	**1000 bar**	**1400 bar**
20 bar	14.2	32.8	36.8	61.8
40 bar	17.2	31.4	45	61.4
60 bar	16.8	29.4	46.6	56
80 bar	16.8	29.2	42.4	63

Table 5.10. Rail pressure drops (in bar) induced by MF50 injection at various injection scenarios

	400 bar	**700 bar**	**1000 bar**	**1400 bar**
20 bar	11.4	29.4	41	54
40 bar	15.6	29.4	42.8	58
60 bar	14.6	28.8	41.8	55.8
80 bar	15.2	28.4	41.4	60.6

As expected, the fuels exhibited an increasing trend in the pressure drop as a result of higher injection pressure. Moreover, in the case of unvaried injection scenarios, the pressure drops of the MF-based fuels are lower than those for diesel. Greater viscosity and density lead to greater frictions at the orifice walls, causing a reduction in jet velocities. As a result, a reduced pressure drop ensues.

However, it is worth noting that at increasing backpressure and unvaried injection pressure, different trends of pressure drop emerge according to the fuel being tested. With regard to diesel, increasing backpressure leads to a slightly decreasing trend in the pressure drop, given the stronger contrasting action exerted by the pressurised vessel's ambiance on the fuel flow exiting the orifices. By contrast, MF-based blends exhibit a gradually increasing trend of pressure drops, which are always lower than those for diesel. However, MF50 revealed a more observable increasing trend in comparison with MF30.

The difference from diesel might be ascribable to the role exerted by the increasing backpressure on the needle's motion. As discussed in the first and second chapters, if on one hand higher backpressure exerts a stronger barrier to fuel flow, on the other it may be assumed to boost needle lift. Accordingly, at a constant injection pressure, a greater backpressure serves as a stronger barrier to fuel flow, mitigating the fuel momentum towards the orifices to the benefit of the momentum transferrable onto the needle.

Therefore, it might be presumed that the additional contribution of backpressure to needle lift is more appreciable for more viscous fuels. This might be due to the more effective lubrication outweighing the frictions between the needle-control piston assembly and the internal part of the injector body. As a result, the needle moves upward more rapidly if compared to lower fuel viscosity (but still greater than for diesel), causing the opening of the cross-sectional area, through which the fuel flows, to occur immediately. In response to a more immediate needle lift, fuel experiences a greater dramatic increase in kinetic energy, which causes a more abrupt reduction in pressure within the nozzle, according to Bernoulli's equation.

On the other hand, the greater viscosity enhances the internal frictions within the fluid. Higher pressure and backpressure are thought to promote the development of thermal effects caused by the internal frictions. In physical terms, greater injection pressure and backpressure promote the effects of higher viscosity on the thermal effects arising within the fluid particle. Therefore, higher temperature, induced by thermal effects, reduces the viscosity of the fluid, which flows more rapidly towards the orifice. As a consequence, a smaller pressure drop ensues. However, this aspect, concerning the combined impact of injection setting with fuel viscosity on the thermal effects within the fluid, is worthy of a thorough investigation.

5.5.3.2. The role of backpressure in rail pressure fluctuations

Tables 5.11-5.13 show the averaged retrieving times, referring to the charts in Figure 5.8.

Table 5.11. Time intervals (in ms) required by rail pressure to retrieve the value preceding the diesel injection

	400 bar	**700 bar**	**1000 bar**	**1400 bar**
20 bar	257.5	322.5	330	425
40 bar	217.5	295	317.5	362.5
60 bar	235	270	302.5	347.5
80 bar	250	345	316.3	367.5

Table 5.12. Time intervals (in ms) required by rail pressure to retrieve the value preceding the MF30 injection

	400 bar	**700 bar**	**1000 bar**	**1400 bar**
20 bar	212.5	255	282.5	352.5
40 bar	125	277.5	297.5	355
60 bar	170	265	252.5	337.5
80 bar	230	322.5	307.5	335

Table 5.13. Time intervals (in ms) required by rail pressure to retrieve the value preceding the MF50 injection

	400 bar	**700 bar**	**1000 bar**	**1400 bar**
20 bar	117.5	205	215	307.5
40 bar	110	222.5	232.5	260
60 bar	135	205	235	325
80 bar	225	232.5	300	317.5

It is observed that the diesel retrieving time is longer than that for MF30, which in turn is larger than for MF50 in most cases. This is ascribable to the greater elasticity of MF-based blends. Moreover, as expected, the increase in injection pressure at unvaried backpressure prolongs the retrieving time; whilst increasing backpressure shortens the retrieving time. Greater backpressure is indeed meaningful of a stronger barrier effect on the fuel flow. A lower flow velocity ensues, giving rise to a smaller pressure drop. Nonetheless, the 700-80 bar case represents an inconsistency. The discrepancy might be ascribed to the great instability of rail pressure fluctuations induced by diesel injection.

By contrast, the MF30 and MF50 injections' trends differ significantly from that of diesel. At higher viscosities, a greater backpressure indeed results in a longer retrieving time. However, given the stronger opposing force of MF-based blends for counterbalancing the inertial effect

originating from pressure perturbation, the MF30 and MF50 retrieving times are revealed to be shorter than for diesel. The trend of the MF-based blends' retrieving times might be explained by the effect of greater viscosity combined with higher backpressure on the needle. As mentioned above, greater viscosity indeed promotes the additional acceleration supplied by the backpressure on the needle. The needle experiences a more abrupt lift, giving rise to an extra dramatic pressure drop. The ensuing rarefaction wave is provided with a larger magnitude. Once it reaches the rail, a longer time is required by the rail pressure to retrieve the value preceding the shot.

An additional explanation might be provided by taking the arising thermal effects into account. Larger viscosity promotes frictions, which give rise to thermal effects, determining a local reduction in viscosity (but still larger than in the case of diesel). As a result, some fluid particles tend to flow more rapidly, leading to greater pressure drops in comparison with MF30.

5.5.3.3. The impact of backpressure on the amplitude of rail pressure fluctuations

The following tables list the amplitudes of pressure fluctuations over the retrieving time.

Table 5.14. Amplitudes of rail pressure fluctuations (in bar) arisen as a result of diesel injection

	400 bar	**700 bar**	**1000 bar**	**1400 bar**
20 bar	22.5 ± 2.5	31 ± 6.5	37.5 ± 2.5	35 ± 5
40 bar	25.33 ± 3	33 ± 6.5	42 ± 2.5	31.6 ± 2.5
60 bar	24 ± 3	34 ± 2	40 ± 4	37.5 ± 2.5
80 bar	24 ± 2	41 ± 1	41.5 ± 3.5	36 ± 5

Table 5.15. Amplitudes of rail pressure fluctuations (in bar) arisen as a result of MF30 injection

	400 bar	**700 bar**	**1000 bar**	**1400 bar**
20 bar	4 ± 1	7 ± 2	11 ± 1	11.5 ± 1.5
40 bar	7.5 ± 0.5	8 ± 0.5	9 ± 3	15.7 ± 3
60 bar	7.5 ± 2.5	9.5 ± 5.5	13.3 ± 3.5	19 ± 3
80 bar	6.5 ± 2.5	12.2 ± 5.5	16.3 ± 2.5	17.6 ± 2.5

Table 5.16. Amplitudes of rail pressure fluctuations (in bar) arisen as a result of MF50 injection

	400 bar	**700 bar**	**1000 bar**	**1400 bar**
20 bar	2.8 ± 0.25	7.5 ± 2.5	5 ± 0.5	7 ± 2.5
40 bar	4 ± 1	7 ± 1	7.5 ± 2.5	15 ± 3
60 bar	7 ± 3	8 ± 2.5	8.5 ± 1.5	15.3 ± 5
80 bar	4 ± 1	6.6 ± 2.5	9.8 ± 4	16.6 ± 7.5

Diesel injection engenders larger amplitudes in comparison with MF30 and MF50 injections. Additionally, at unvaried backpressure, higher injection pressures lead to larger amplitudes. This might be due to the greater pressure drop, which amplifies the magnitude of the rarefaction wave.

On the other hand, at unvaried injection pressure, an increase in backpressure results in larger amplitudes in most cases. More specifically, this is more observable for MF-blends. Indeed, the boosting action of backpressure on the needle is further favoured by better lubrication due to the greater viscosity. As a result, a greater rarefaction wave (but smaller if compared to diesel) arises, generating wider amplitudes of rail pressure fluctuation.

5.5.3.4. The influence of backpressure on the time between rail pressure peaks

The tables below list the averaged time between two consecutive peaks, providing an indication of the pressure pulsations' frequency.

Table 5.17. Duration of the time interval (in ms) between two consecutive pressure peaks (diesel injection)

	400 bar	**700 bar**	**1000 bar**	**1400 bar**
20 bar	100 ± 5	100 ±	95.5 ± 5	70 ± 10
40 bar	120 ± 5	125 ± 12.5	140 ± 20	90 ± 10
60 bar	100 ± 5	105 ± 5	100 ± 5	90 ± 10
80 bar	110 ± 10	135 ± 15	110 ± 10	90 ± 10

Table 5.18. Duration of the time interval (in ms) between two consecutive pressure peaks (MF30 injection)

	400 bar	**700 bar**	**1000 bar**	**1400 bar**
20 bar	40 ± 10	40 ± 5	50 ± 10	76.6 ± 25
40 bar	35 ± 15	40 ± 10	55 ± 5	115 ± 15
60 bar	45 ± 10	35 ± 5	50 ± 10	76.6 ± 25
80 bar	35 ± 5	50 ± 10	50 ± 10	120 ± 20

Table 5.19. Duration of the time interval (in ms) between two consecutive pressure peaks (MF50 injection)

	400 bar	**700 bar**	**1000 bar**	**1400 bar**
20 bar	25 ± 5	25 ± 5	30 ± 10	45 ± 5
40 bar	30 ± 10	35 ± 5	33.3 ± 15	55 ± 15
60 bar	30 ± 5	35 ± 5	30 ± 10	60 ± 20
80 bar	30 ± 10	40 ± 10	45 ± 5	83.3 ± 15

It can be seen that diesel injection leads to a longer time interval between two consecutive pressure peaks in comparison with MF30 and MF50. Namely, the period of the diesel pressure fluctuations is significantly larger than that for MF-based blends. Furthermore, an increase in injection pressure prolongs the time intervals. Likewise, at unvaried injection pressure, greater backpressure leads to a longer time. Therefore, differently from pressure drops and retrieving time, increasing viscosity (but still greater than for diesel) does not cause any increasing trend at unvaried injection pressure and increasing backpressure.

5.6. The physical principles underlying the findings

The findings can be explained by focusing on the impact of the fluid properties on the waves' propagation across a fluid.

5.6.1. Influence of the bulk modulus on wave propagation

From Equation 5.1, it emerges that the speed c of wave propagation across a liquid is enhanced by higher bulk modulus. Assuming that liquid fuel is compounded with layers, wave propagation is indeed faster thanks to the promoted reflection between the layers, to the detriment of the wave absorption. Such reflection generates inertial effects resulting in smaller oscillations' amplitude. Therefore, being as greater bulk modulus is indicative of a greater fluid stiffness, the fluid layers are more prone to reflect the wave energy. In mechanical terms, the layers are more constrained if compared to fluid provided with lower bulk modulus, which is meaningful of greater propensity to absorb the wave energy, in favour of amplitude oscillation.

Hence, it is deducible that the lower bulk modulus accentuates pressure fluctuations underlying the spray's non-uniformity, which affects adversely both the A/F ratio and the combustion efficiency. In the wake of these considerations, it may be inferred that the wave energy which is potentially transferrable to the fuel can be divided into two components. One component is associated with the wave reflection and is enhanced by higher bulk modulus; whilst the other refers to the wave absorption, which contributes to the amplitude of the pressure fluctuations. The magnitude of the single factors is determined by the fuel properties. Additionally, while rail pressure is approaching the value preceding the start of the previous injection, the temporal interval between two consecutive pressure peaks is lower in the case of the greater bulk modulus. A further explanation may be provided by d'Alembert's equation, which describes wave propagation through a fluid and is given by:

$$\frac{\delta^2 p(x)}{\delta x^2} + \frac{\delta^2 p(y)}{\delta y^2} + \frac{\delta^2 p(z)}{\delta z^2} = \frac{1}{c^2} \frac{\delta^2 p(t)}{\delta t^2} \tag{5.3}$$

with *p*, *c* and *t* being pressure acting on the fluid region involved by the wave propagation, wave speed and time, respectively. In the present case, d'Alembert's equation may describe the fluid pressure gradient arising in response to a wave perturbation travelling at velocity *c*. Keeping in mind that increasing bulk modulus boosts the speed of the pressure wave, it may be conjectured that a faster wave propagation softens the impact on the pressure gradient arisen in the surrounding fluid region (Figure 5.11).

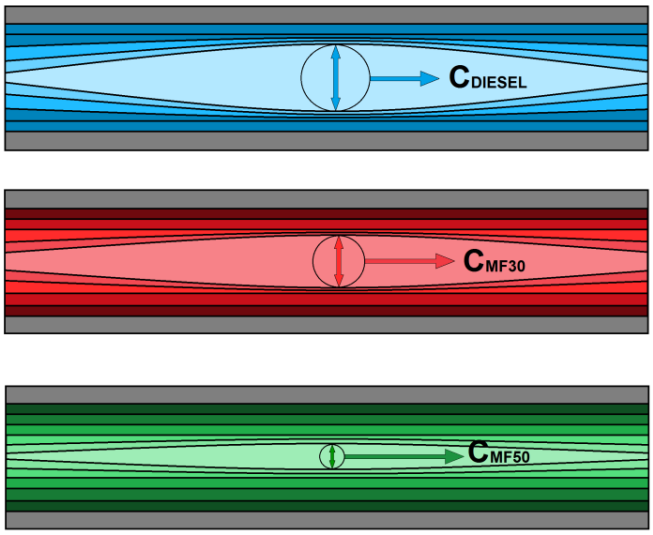


Figure 5.11. Increasing bulk modulus boosts the speed of the pressure wave, mitigating the effect on the surrounding fluid region, where a less accentuated gradient pressure arises

Indeed, higher speed *c* does not allow the wave energy to be sufficiently transferred to the fluid region involved in the wave propagation.

Furthermore, paying attention to the curves and graphs, it may be argued that bulk modulus quantifies the propensity of the fluid to recover the status preceding perturbation. Accordingly, the fluid provided with the largest bulk modulus tends to approach more rapidly the pressure preceding the occurred injection event, because of the smaller oscillation amplitude.

5.6.2. The impact of fluid elasticity on pressure oscillations

Once a fluid is perturbed by a pressure wave, it experiences deformation, which results in a volume change. Opposing forces, determined by the fuel properties, arise in response to such a deformation. Indeed, according to Hooke's law applied to fluids, the opposing forces are determined by the fluid's elasticity, which provides an estimation of the fluid's propensity to retrieve the conditions preceding the perturbation.

These forces counterbalance the inertial effects caused by the pressure wave, until the fluid status preceding the perturbation is retrieved. Additionally, as the compressibility is an

estimation of the change in volume induced by a variation in pressure, it might be presumed that greater compressibility results in a weaker opposing force. Accordingly, diesel pressure requires a longer time to retrieve the initial value. By contrast, greater density and bulk modulus, which are indicative of more closely positioned fluid particles, make the MF-based blends less prone to a volume change in response to a pressure wave perturbation. Thus, the opposing forces are stronger, shortening the retrieving time.

5.6.3. The impact of surface tension and fuel viscosity on pressure oscillations

Besides the bulk modulus, surface tension and viscosity contribute to the magnitude of the opposing forces. Surface tension is indeed believed to determine considerably the opposing reaction Δp, which contrasts to the fluid deformation caused by wave perturbation. Assuming that infinitesimal fluid particles are ideally spherically shaped, the opposing reaction Δp is proportional to the ratio of surface tension Θ with the radius R, according to the generalised Young-Laplace equation of capillarity:

$$\Delta p \approx \frac{2 \cdot \Theta}{R} \tag{5.4}$$

Table 5.20 lists the values of diesel's surface tension as a function of temperature. **(135)**

Table 5.20. Diesel's surface tension as a function of temperature

T (˚C)	σ (N/m)
20	$29.46 \cdot 10^{-3}$
25	$29.04 \cdot 10^{-3}$
30	$28.74 \cdot 10^{-3}$
35	$28.40 \cdot 10^{-3}$
40	$28.02 \cdot 10^{-3}$
45	$27.76 \cdot 10^{-3}$
50	$27.34 \cdot 10^{-3}$
55	$26.96 \cdot 10^{-3}$
60	$26.66 \cdot 10^{-3}$

With regard to the MF-based properties, a survey of the literature showed the paucity of experimental data for pure DMF. **(136, 137)** Nonetheless, the literature concerning the furan-based fuels **(37, 138)** states that MF30 and MF50 surface tensions are greater than diesel. This conclusion was drawn also in the light of the longer delay of the disintegration of the MF-based fuels' spray, due to the stronger intermolecular interactions which are determined by the surface tension. Hence, it can be merely inferred that diesel's surface tension engenders a weaker opposing force contrasting to the injection-induced inertial effects.

Concerning viscosity, it is thought it provides an indication of a fluid's ability to dampen the oscillations, generating an opposing force F_V approximately calculable as:

$$F_V \approx \frac{\mu \cdot V}{L^2} \tag{5.5}$$

where μ, V and L stand for: fuel viscosity; the relative velocity between the liquid and the surrounding gas; and the unit of length of the fluid particle, respectively. It is deducible that, along with the supposed greater surface tension, higher fuel viscosity generates stronger actions, which alleviate the fluid's instability stemming from the wave perturbation.

5.6.4. Peculiarities of MF-blends benefiting rail pressure fluctuations

The above considerations lead us to conclude that the MF-blends' properties minimise the unpredictability of the dynamic effects arising after the injection start. In fact, it is revealed that the rail pressure retrieves its value recorded previous to the injection, more rapidly. This minimises the risk that the injector's solenoid is energised when the dynamical effects make injection pressure lower than the set value of the rail pressure, to the detriment of the jet's non-uniformity. This represents a potential benefit for the optimisation of the injection strategy; where its set-up is devoted to trigger the injector when the injection pressure equals the set rail pressure or exceeds it. This then would enhance the spray's penetration length and

jet disintegration. Furthermore, keeping in mind that modern injection systems enable the injection cycle to be split up into eight separate shots, the peculiarities of MF-based blends are further marked by the consequential decrease in the dwell times between two consecutive shots, characterising the modern *MultiJet* system.

5.7. Summary

An experimental investigation was conducted to study in depth the combined impact of injection settings and fuel properties on pressure fluctuations occurring in a CR injection system. Along with injection pressure, the study singled out viscosity, density and bulk modulus as the key factors determining rail pressure fluctuations, and affecting meaningfully the non-uniformity in jets' velocities. The analysis of the results was focused on aspects of the dynamics' effects such as:

- pressure drop stemming from needle lift;
- pressure fluctuations' amplitude;
- the retrieving time, namely the interval between the lowest pressure and the one preceding the start of injection;
- time between two consecutive pressure peaks.

The conclusions drawn from the experimental activity are summarised below.

1. For all tested fuels, pressure drop, arising after the start of injection, is strongly correlated with the fuel properties. As expected, higher viscosity and greater density soften pressure drop, which is accentuated by higher injection pressure.
2. At unvaried injection pressure, greater backpressure softens the diesel pressure drop within the rail. By contrast, MF30 and MF50 pressure drops tend to increase in response to greater backpressure.

3. At unvaried injection pressure and greater backpressures, lower viscosity (but still higher than diesel) tends to alleviate the increase in rail pressure drop in most cases.
4. Diesel's retrieving time is longer than for MF30; which in turn is greater than that for MF50 in most of the cases. At unvaried injection pressure, diesel's retrieving time tends to be shortened in response to increasing backpressure in most cases. Conversely, increasing backpressure tends to prolong MF30 and MF50 retrieving times.
5. The discrepancies may be ascribed to the thermal effects arising from the combined action of the injection settings and greater viscosity. This determines frictions, engendering the reduction in local fluid viscosity, and generating the behaviour of less viscous fluids.
6. The discrepancy may be ascribed also to the combined impact of backpressure with fuel viscosity on the time-history of the needle lift.
7. Furan-based blends, which have a greater bulk modulus, are subjected to lower pressure fluctuations. Increasing bulk modulus is indeed believed to not allow the wave energy to be sufficiently transferred to the fluid region involved in wave perturbation.
8. Fuels with lower bulk modulus are more prone to absorb the wave energy wave, generating wider amplitudes of pressure oscillation. This was shown especially with diesel injections, and results in high margins in the unpredictability of injection pressure fluctuations.
9. During the stage when rail pressure approaches the value preceding the previous injection, the temporal interval between two consecutive pressure peaks is shorter in the case of smaller bulk modulus.

The findings emphasise the combined action of the injection settings with the fluid characteristics on injection pressure fluctuations, which are thought to contribute to the imbalance of fuel flow through the orifices. It can be seen that greater viscosity and bulk modulus alleviate significantly these fluctuations, minimising the unpredictability of the rail pressure time-history. In the light of the presented findings, which highlight the peculiarities of MF-based blends, it would be desirable that the automotive industry employs great resources to assess their applicability on IC engines. This step would further unlock the potentialities of the MF-based blends, which represent an appealing solution for petroleum-free mobility.

CHAPTER 6

CONCLUSIONS AND FUTURE WORKS

Introduction

This thesis was focused on the identification of the physical principles governing the orifice-to-orifice variability in jets' velocities.

The first step was the design and testing of an innovative sensor for needle lift measurement, followed by high-fidelity tests devoted to the investigation of the orifice-to-orifice non-uniformity in jets' velocities at the early stages of the injection event. Thereafter, an experimental investigation of injection-induced pressure oscillations occurring in the rail was undertaken. In order to keep consistency among the stages compounding the development of the thesis' work, the same injection settings were applied for each of the covered topics.

The thesis thereby covered four main topics, reviewing the combined impact of injection settings with the fuel properties and injector geometry on the variability.

This chapter summarises the findings emerging from the thesis, key points which lead to the conception of novel methodologies; their development it is believed will further improve the quality of the injection. On the basis of the findings emerging from this work, the physical principles underlying these solutions are analysed, followed by a preliminary assessment of the margins of feasibility.

6.1. Summary of the thesis

From the experimental campaign, it emerged that:

- backpressure considerably determines the time history of needle displacement over the injection event;

- along with injection pressure, backpressure plays an effective role in the orifice-to-orifice variability of jets' velocities;
- at unvaried injection pressure, backpressure exerts a non-negligible impact on injection-induced pressure fluctuations within the rail;
- fuel properties, such as:
    a. viscosity
    b. density
    c. bulk modulus
    d. surface tension

play a decisive role on the characterisation of phenomena governing the non-uniformity of fuel jets' development. These findings are thought to provide a further insight into the combined impact of injection settings and fuel properties on the jets' characterisation.

6.2. Summary of the findings

This section summarises the findings which emerged from each research activity included in this thesis.

6.2.1. The assessment of needle motion over the injection event

The second chapter pertains to the design of a novel transducer, able to overcome the limitations typically characterising actual needle lift sensors. An optical-fibre-based transducer was developed and rigorously tested at various injection scenarios. The tests demonstrated that, alongside injection pressure, backpressure plays a crucial role in needle motion over the injection process. More specifically, it was found that:

1. at constant injection pressure and energising time, higher backpressures boost needle lift.
2. At constant injection pressure and energising time, higher backpressures prolong the stage during which the control piston-needle assembly is at the maximum position.

3. At unvaried injection pressure, an increase in backpressure results in a faster injector closure.

These observations led us to assume that the pressurised fuel momentum can be divided into two components, namely:

1. a component acting on the needle protrusion and promoting needle lift;
2. a component promoting fuel flow towards the orifice inlet.

The findings emerging from the tests are believed to further ascertain the advantages of the proposed technique.

6.2.2. The assessment of orifice-to-orifice variability of diesel jets' velocities

The third chapter provides a detailed insight into the combined influence of backpressure with injection pressure on the non-uniformity of diesel jets' development. The assessment included the analysis of the delays of the injection. In the light of findings emerging from the experimental campaign, it can be concluded that:

1. at a constant backpressure, an increase in injection pressure shortens the range over which the DOI values are spread out.
2. At a constant backpressure, increasing injection pressure reduces the standard deviation of diesel plumes' velocities, indicating an improved uniformity of the jets' development.
3. The combined increase in injection pressure with backpressure promotes the fuel momentum transferrable onto the needle, giving rise to a faster lift and softening the harmful impact of needle wobbles on the uniformity of the diesel jets' development.
4. If on one hand higher backpressure is thought to enhance needle lift, on the other it is presumed to promote needle wobbles.
5. Given the nozzle design, needle lift outweighs off-axis motion more significantly at higher injection pressures and greater backpressures.

6.2.3. The hole-to-hole variability of diesel jets' velocities compared to MF-based blends

A detailed examination of the combined influence of injection settings with fuel properties on hole-to-hole non-uniformity of the fuel plumes' velocities and injection delays is provided in the fourth chapter.

The findings are summarised below.

1. In the case of MF30 injections, given the larger standard deviations of the jets' velocities than for MF50 and diesel, it is presumable that the action attributable to fuel density does not suffice to dampen shear stress, determining the needle's off-axis motion.
2. Diesel's standard deviations are positioned in the middle, indicating a more stable balance between these stresses acting on the needle.

Concerning the influence of injection settings with fuel properties on the DOI, MF50 exhibited the longest DOIs in most cases, followed by MF30 and diesel. However, some inconsistencies were observed.

3. MF50 exhibited a shorter DOI than for MF30 in some cases. This might be attributed to frictions within the fluid, engendering a local decrease in viscosity and density.
4. Diesel showed a longer DOI than for MF30 in some cases. It is conceivable that longer DOIs are due to injection-induced pressure fluctuations, which lead the diesel injections to be performed at a lower pressure than the set rail pressure, yielding unexpected results

.

6.2.4. The investigation of injection-induced pressure fluctuations within the rail

An accurate examination of the combined influence of injection settings with fuel properties on the injection-induced pressure fluctuations arising in the rail is provided in the fifth chapter. The conclusions are summarised below.

1. At unvaried injection pressure and greater backpressures, lower viscosity (but still greater than for diesel) softens the pressure drop if compared with the case of a more viscous fuel.
2. The diesel retrieving time is longer than that for MF30, which in turn is greater than that of MF50 in most of the cases. Additionally, at unvaried injection pressure and greater backpressures, lower viscosity (but still higher than in the case of diesel) prolongs the retrieving time.
3. These inconsistencies may be due to the thermal effects arising from the combined action of the injection settings and greater viscosity.
4. The discrepancies may be ascribed also to the combined impact of backpressure with fuel viscosity on the time-history of the needle lift.
5. Greater bulk modulus, characterising the MF-based blends, softens rail pressure fluctuations. Increasing bulk modulus is indeed believed to not allow the wave energy to be sufficiently transferred to the fluid region involved in the wave propagation.
6. Lower bulk modulus allows the fluid to absorb the wave energy wave, generating wider amplitudes of rail pressure fluctuations.

6.3. Recommendations for future research activities

The outcomes of this study suggest future research activities be undertaken; aiming to clarify the concerns arising from this thesis. The following sections describe some studies which are indeed believed to provide a further insight into the injection process.

6.3.1. Technique for increasing injection pressure

The statistical analysis of the hole-to-hole variability in jets' velocities highlighted that increasing injection pressure shortens the range over which the velocities are spread out. Increasing injection pressure has also been demonstrated to improve fuel injection in terms of

penetration length, radial propagation and break-up timing, to the advantage of the A/F mixing within the cylinder. On the other hand, increasing rail pressure implies a higher consumption of energy is required by the overall system. Moreover, higher pressures increase the risk of fuel leakages, requiring additional devices. Furthermore, from the MF50 testing it emerged that the energy consumption of the high-pressure pump is further increased in the case of very viscous fuels. Additionally, greater injection pressure gives rise to criticalities related to the need to dynamically adjust the maximum pressure according to the engine operating scenarios. **(51, 139)**

6.3.1.1. Layout of the proposed method

The drawbacks related to increasing rail pressure led the author to conceive a methodology; the working principles of which are based on the water hammer effect, originating in response to a sudden stop of fuel flowing through a dedicated acceleration duct (Figure 6.1).

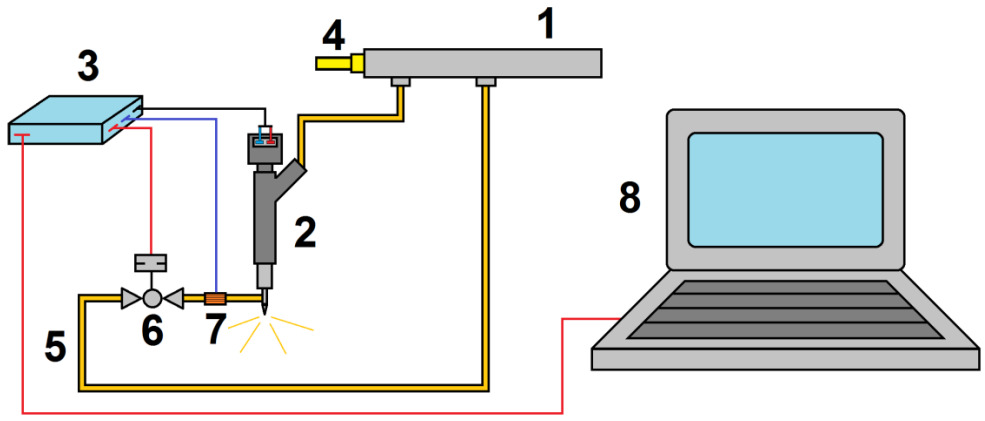


Figure 6.1. The sketch of the proposed technique to induce greater injection pressures, so as to recover the pressure gaps originated from the dynamic effects within the rail: 1 – rail; 2 – CR injector; 3 – ECU; 4 – fuel pressure sensor; 5 – fuel acceleration duct; 6 – electronically managed shutdown valve; 7 – strain gauge; 8 – computer

A shutdown valve, electronically managed via a signal delivered by the ECU or any FAQ device, is placed on the acceleration duct. The layout includes a strain gauge on the acceleration duct, to be positioned between the shutdown valve outlet and the nozzle. This

solution would allow detection of the fuel pressure along the acceleration duct; acquiring also the magnitude of the water hammer effect due to the sudden stop of the fuel flow. The choice of the strain gauge is mainly justified by the high cost of the fuel pressure sensor traditionally placed on the injector nozzle.

6.3.1.2. Working principle of the proposed method

As the shutdown valve is activated, the fuel flow is suddenly stopped, engendering a water hammer effect. Fuel kinetic energy is thereby converted into a compression wave, which propagates towards the nozzle. Hence, a local increase in nozzle pressure takes place. As a consequence, it is desirable that the injector's solenoid is energised as the nozzle pressure overcomes the set rail pressure thanks to water hammer effect, favouring the jets' penetration length, the radial dispersion and the break-up timing. This would lead to set the injection strategy according to the timing of the valve activation, so as to commence the injection when the water hammer effect has not yet started to decay.

6.3.1.3. Possible drawbacks related to the induced increase in injection pressure

As fiercely assessed in Chapter 5, greater injection pressure accentuates pressure drops stemming from needle lift, promoting the dynamics' effects and the unpredictability of rail pressure time-history, especially in the case of low fuel-bulk modulus.

Therefore, for the feasibility of the proposed technique, it would be worth investigating the competition between the greater pressure gap and the possibility to recover it via the sudden stopping of the flow in the acceleration duct. This concern might lead to a deeper assessment of the suitability of using MF-based blends within a CI engine. In fact, MF-based blends can retrieve the previously set rail-pressure value more rapidly compared to neat diesel, as the pressure gap is recovered faster.

Thus, the benefiting impact of the water hammer action is presumed to prevail over the ensuing dynamic effects, originating from the rail pressure drop and underlying the subsequent injection pressure gaps.

6.3.1.4. Further development of this research activity

The generation of water hammer effects raises concerns about compression wave propagation through the duct connecting the shutdown valve outlet and the nozzle inlet. In order to optimise the benefiting effect of the water hammer, it would be worthwhile to assess the combined impact of fuel properties and the internal geometry of the system; including:

- the acceleration duct;
- the interface with the nozzle inlet;
- and the shutdown valve

on the magnitude of the water hammer effect and their subsequent influence on the spray characteristics. Additionally, it would be worthy of interest to investigate wave propagation through the system, positioning additional strain gauges along:

- the duct between the outlet of the shutdown valve and the nozzle inlet;
- the duct between the injector inlet and the rail,

so as to attain mapping of the wave propagating through the injection layout. This approach is thought to provide a further insight into the combined influence of the fuel properties with layout geometry and injection settings on waves' propagation through the system.

6.3.2. CFD for the assessment of the combined action of viscosity with density on needle wobbles

The investigation of the hole-to-hole variability of jets' velocities shed light on the combined action of fuel viscosity with density on needle off-axis motion at the early stages of the injection event. Particularly, despite the lower viscosity engendering weaker shear stress on

the needle, MF30 fuel exhibits a more uneven jet development in comparison with MF50. By contrast, although having greater viscosity, MF50 shows a more uniform jet development. Being as MF30 had a lower density, it might be hypothesised that density does not suffice to dampen the oscillations stemming from the shear stress on the needle.

Although these assumptions plausibly explain the findings emerging here, high-fidelity numerical investigations are desirable, so as to clarify the concerns about the competition between fuel density and viscosity on the needle's off-axis motions.

6.3.3. The needle's off-axis sensor

The investigations of the hole-to-hole variability of jets' velocities raised the issue related to the need to detect needle wobbles. In this regard, several research activities turned attention to the impact of the needle's off-axis motion on the unbalance of the injected flow rate. **(81, 89-97)** The assessments were carried out via numerical methodologies. Therefore, an experimental approach would be desirable in view of possible lab activities devoted to assess the fuel jet's development at various injection scenarios and employing different fuels.

6.3.3.1. Main criticalities related to the detection of needle wobbles

Several criticalities discourage the experimental approach. In fact, likewise to the issues related to needle lift measurement, the narrow areas within the nozzle make the physical accessibility very difficult. Moreover, the annular gap between the internal walls and the needle surface is very small, and the installation of an external device is likely to disturb fuel flow towards the orifice. Therefore, it would be desirable to employ a heavy-duty injector or an injector for marine applications.

Furthermore, being as the nozzle pressure is very high, additional devices are required to prevent leakages. This solution is preferably viable by means of a clamp adapter **(52, 73, 74)**, which tightens the detecting device on the nozzle. In this regard, the clamp adapter is not

installed in the vicinity of the nozzle tip. The injector nozzle is indeed placed into the engine head or the HPV top, reducing significantly the physical accessibility to the area.

6.3.3.2. Possible techniques for the detection of needle wobbles

In order to maximise the detection of needle wobbles, the detecting device should be positioned within correspondence distance of the needle tip. This approach is justified by the greater sensitivity of the needle tip to the cantilever effect. Despite these criticalities, the viability of various solutions might be worthy of thorough assessment.

6.3.3.2.1. Electromagnetic fields-based solution

A possible solution is based on the electromagnetic fields generated by the needle tip made of ferromagnetic material. The ferromagnetic tip must be tightly stuck to the needle body. As the injection commences, this part is presumed to be highly sensitive to the cantilever effect characterising the needle lift. The mutual position between the tip and the detector changes more significantly in comparison with the remaining needle body. Hence, the ensuing variation of electromagnetic fields, meaningful of needle wobbles, is larger.

On the other hand, likewise to the eddy current transducer devoted to measure needle lift, electromagnetic interferences altering the cleanliness of the wobbles' signal might arise at the injector triggering. This drawback is supposed to be overcome by means of a plate mounted on the injector body, so as to shield the needle tip region. This would allow the insulation of the electromagnetic field originating from the needle tip, preventing harmful interference with the fields originating in the area of the injector's solenoid.

6.3.3.2.2. The optical technique

An alternative pathway is represented by working principles based on light transmission. This potential solution basically consists of an emitter and a receiver detecting light travelling

through the measurement area, which is characterised by tiny slots machined on the nozzle and on the needle (Figure 6.2).

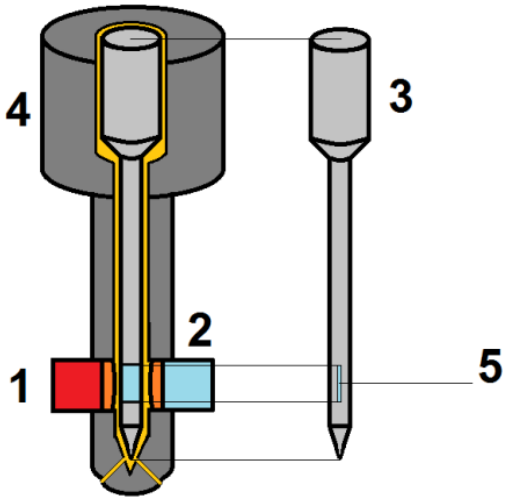


Figure 6.2. The sketched layout of the optical solution: 1 – emitter; 2 – receiver; 3 – needle; 4 – nozzle; 5 – slot machined on the needle

Due to the sensitivity of the needle tip to the cantilever effect, this slot is presumed to be machined close to the needle tip. It would be preferable that the slot width is very small, so as to increase the detector's sensitivity to wobbles. Both emitter and the receiver must be tightly stuck into the nozzle; whilst the characteristics of the beam should enable the light to travel through the fuel, minimising the scattering phenomena. On the other hand, similar to the technique proposed by Amirante *et al.* and aimed to measure needle lift, the presence of fuel within the measurement area can hinder the travelling light beam, to the detriment of the cleanliness of the output signal. **(73, 74)**

Similar to the technique based on the generation of electromagnetic fields, this approach is invasive. As such, an external device mounted close to the needle tip might disturb fuel flow through the annular gap between the needle and the nozzle's internal walls, altering the acquisition of the signal.

REFERENCES

1. https://hiconsumption.com/1955-mercedes-benz-300-sl-gullwing/
2. Buzzonetti, D., & Forghieri, M. (2008). Mauro Forghieri, 30 anni di Ferrari [e oltre]. Giunti.
3. Cozza, E. (2017). Con la Maserati nel cuore. Giunti
4. http://megadeluxe.com/cars/1954-mercedes-benz-w196-grand-prix-racing-car
5. https://www.flickr.com/photos/digitalslrphotos/32066359836/
6. https://silodrome.com/1964-ferrari-158/
7. https://www.boschautoparts.com/en/bosch-for-gdi/gm-3.6l-buick
8. Xu, H., Wang, C., Ma, X., Sarangi, A. K., Weall, A., & Krueger-Venus, J. (2015). Fuel injector deposits in direct-injection spark-ignition engines. Progress in Energy and Combustion Science, 50, 63-80.
9. Wang, B., Jiang, Y., Hutchins, P., Badawy, T., Xu, H., Zhang, X., ... & Tafforeau, P. (2017). Numerical analysis of deposit effect on nozzle flow and spray characteristics of GDI injectors. Applied Energy, 204, 1215-1224.
10. Wang, B., Badawy, T., Hutchins, P., Tu, P., Xu, H., & Zhang, X. (2017). Numerical investigation of the deposit effect on GDI injector nozzle flow. Energy Procedia, 105, 1671-1676.
11. Wang, B., Badawy, T., Jiang, Y., Xu, H., Ghafourian, A., & Zhang, X. (2017). Investigation of deposit effect on multi-hole injector spray characteristics and air/fuel mixing process. Fuel, 191, 10-24.
12. Wang, C., Xu, H., Herreros, J. M., Wang, J., & Cracknell, R. (2014). Impact of fuel and injection system on particle emissions from a GDI engine. Applied Energy, 132, 178-191.
13. Wang, Z., Ma, X., Jiang, Y., Li, Y., & Xu, H. (2017). Influence of deposit on spray behaviour under flash boiling condition with the application of closely coupled split injection strategy. Fuel, 190, 67-78.
14. http://motori.quotidiano.net/autoemotonews/alfa-romeo-le-innovazioni-tecniche-piu-importanti.htm
15. Stumpp, G. and Ricco, M., 1996. Common rail-an attractive fuel injection system for passenger car DI diesel engines (No. 960870). SAE Technical Paper.
16. https://www.automotiveworld.com/news-releases/10-million-bosch-common-rail-systems-for-commercial-vehicles/
17. https://www.wtryskiwacz.com/jakie-mamy-pompy-wysokiego-cisnienia-Delphi-a-jakie-Bosch-naprawa-regeneracja.html
18. https://www.bosch-mobility-solutions.com/en/solutions/fuel-supply/high-pressure-rail/
19. https://carbiketech.com/fuel-injector/
20. https://www.topspeed.com/cars/car-news/audi-r10-tdi-record-lap-at-sebring-ar29661/pictures.html
21. http://www.dieselstation.com/Peugeot/908-HDi-FAP-2010/Peugeot-908-HDi-FAP-2010-wallpaper-ds11-i3169.html

22. Adewale, P., Dumont, M. J., & Ngadi, M. (2015). Recent trends of biodiesel production from animal fat wastes and associated production techniques. Renewable and Sustainable Energy Reviews, 45, 574-588.
23. Jones, C. S., & Mayfield, S. P. (2012). Algae biofuels: versatility for the future of bioenergy. Current opinion in biotechnology, 23(3), 346-351.
24. Patil, A. R., & Taji, S. G. (2013). Effect of oxygenated fuel additive on diesel engine performance and emission: A review. IOSR Journal of Mechanical and Civil Engineering (IOSR-JMCE), 30-35.
25. National Research Council. (2008). Transitions to alternative transportation technologies: A focus on hydrogen. National Academies Press.
26. Saini, S., Meghendra, S., & Kumar, A. (2018). Global warming and climate change: next generation biofuels and role of biotechnology. Intl J Life Sci Pharma Res, 8(2), 52-57.
27. Aro, E. M. (2016). From first generation biofuels to advanced solar biofuels. Ambio, 45(1), 24-31.
28. Amirante, R., Coratella, C., Distaso, E., & Tamburrano, P. (2015). A small size combined system for the production of energy from renewable sources and unconventional fuels. Energy Procedia, 81, 240-248.
29. Dragone, G., Fernandes, B. D., Vicente, A. A., & Teixeira, J. A. (2010). Third generation biofuels from microalgae.
30. Román-Leshkov, Y., Barrett, C. J., Liu, Z. Y., & Dumesic, J. A. (2007). Production of dimethylfuran for liquid fuels from biomass-derived carbohydrates. Nature, 447(7147), 982-985.
31. LORNE, D. B., A. 2019. Biofuels in the Road Transport Sector [Online]. IFP Energies Nouvelles. Available: https://www.ifpenergiesnouvelles.com/article/biofuels-dashboard-2019 [Accessed 03/02/2020 2020].
32. Hardenberg, H. O., & Schaefer, A. J. (1981). The use of ethanol as a fuel for compression ignition engines (No. 811211). SAE Technical paper.
33. Battistoni, M., Mariani, F., Risi, F., & Poggiani, C. (2015). Combustion CFD modeling of a spark ignited optical access engine fueled with gasoline and ethanol. Energy Procedia, 82, 424-431.
34. Mancaruso, E., & Vaglieco, B. M. ETHANOL AND DIESEL FUEL IN EURO5 SINGLE CYLINDER RESEARCH ENGINE. XXXIV Meeting of the Italian Section of the Combustion Institute. http://www.combustion-institute.it/proceedings/XXXIV-ASICI/papers/34proci2011.I8.pdf
35. Lapuerta, M., Armas, O., & Herreros, J. M. (2008). Emissions from a diesel–bioethanol blend in an automotive diesel engine. Fuel, 87(1), 25-31.
36. Brassat, A., Thewes, M., Müther, M., Pischinger, S., Lee, C., Fernandes, R. X., ... & Uygun, Y. (2012). Analysis of the effects of certain alcohol and furan-based biofuels on controlled auto ignition (No. 2012-01-1135). SAE Technical Paper.
37. Thewes, M., Muether, M., Pischinger, S., Budde, M., Brunn, A., Sehr, A., ... & Klankermayer, J. (2011). Analysis of the impact of 2-methylfuran on mixture formation and combustion in a direct-injection spark-ignition engine. Energy & Fuels, 25(12), 5549-5561.

38. Román-Leshkov, Y., Chheda, J. N., & Dumesic, J. A. (2006). Phase modifiers promote efficient production of hydroxymethylfurfural from fructose. Science, 312(5782), 1933-1937.
39. Edwards, P. P., Kuznetsov, V. L., David, W. I., & Brandon, N. P. (2008). Hydrogen and fuel cells: towards a sustainable energy future. Energy policy, 36(12), 4356-4362.
40. Ahmed, A., Al-Amin, A. Q., Ambrose, A. F., & Saidur, R. (2016). Hydrogen fuel and transport system: A sustainable and environmental future. International journal of hydrogen energy, 41(3), 1369-1380.
41. Lipman, T. E. (2020). Vehicle technologies for achieving near and longer term fuel economy and climate goals. In Transportation, Land Use, and Environmental Planning (pp. 217-236). Elsevier.
42. Gillingham, K. (2007). Hydrogen internal combustion engine vehicles: a prudent intermediate step or a step in the wrong direction. Department of Management Science & Engineering Global Climate and Energy Project Precourt Institute for Energy Efficiency of Stanford University.
43. Wang, C., Sahu, A., Coratella, C., Xu, C., Saul, J., & Xu, H. (2019). Spray characteristics of a gasoline-diesel blend (ULG75) using high-speed imaging techniques. Fuel, 239, 677-692.
44. Bullis, K. (2015). Why we don't have battery breakthroughs.
45. Zhao, S., & You, F. (2019). Comparative life-cycle assessment of Li-ion batteries through process-based and integrated hybrid approaches. ACS Sustainable Chemistry & Engineering, 7(5), 5082-5094.
46. Wang, Z., Wyszynski, M. L., Xu, H., Abdullah, N. R., & Piaszyk, J. (2015). Fuel injection and combustion study by the combination of mass flow rate and heat release rate with single and multiple injection strategies. Fuel Processing Technology, 132, 118-132.
47. Dahlander, P., Iemmolo, D., & Tong, Y. (2015). Measurements of time-resolved mass injection rates for a multi-hole and an outward opening piezo GDI injector (No. 2015-01-0929). SAE Technical Paper.
48. Ferrari, A., Mittica, A., Paolicelli, F., & Pizzo, P. (2016). Hydraulic characterization of solenoid-actuated injectors for diesel engine Common Rail systems. Energy Procedia, 101, 878-885.
49. Bianchi, G. M., Falfari, S., Brusiani, F., Pelloni, P., Osbat, G., & Parotto, M. (2005). Numerical investigation of critical issues in multiple-injection strategy operated by a new CR fast-actuation solenoid injector (No. 2005-01-1236). SAE Technical Paper.
50. Catania, A. E., Ferrari, A., & Manno, M. (2008). Development and application of a complete multijet common-rail injection-system mathematical model for hydrodynamic analysis and diagnostics. Journal of Engineering for Gas Turbines and Power, 130(6).
51. Catalano, L.A., Tondolo, V.A., and Dadone, A., "Dynamic Rise of Pressure in the Common Rail Fuel Injection System," SAE Technical Paper 2002-01-0210, 2002, doi:10.4271/2002- 01-0210. 14.
52. Amirante, R., Catalano, L.A., Dadone, A., and Lombardo, V., "On the Use of Fast-Response Pressure Transducers in a Common Rail Diesel Injection System," in 8th

Biennial ASME, Conference on Engineering Systems Design and Analysis (ESDA) Torino (IT), July 2006, 4-7.

53. Payri, F., Luján, J. M., Guardiola, C., & Rizzoni, G. (2006). Injection diagnosis through common-rail pressure measurement. Proceedings of the Institution of Mechanical Engineers, Part D: Journal of Automobile Engineering, 220(3), 347-357.
54. Chan, Q. N., Bao, Y., & Kook, S. (2014). Effects of injection pressure on the structural transformation of flash-boiling sprays of gasoline and ethanol in a spark-ignition direct-injection (SIDI) engine. Fuel, 130, 228-240.
55. Beierer, P., Huhtala, K., Lehto, E., & Vilenius, M. (2005). Study of the impact of system characteristics on pressure oscillations in a common rail diesel fuel injection system (No. 2005-01-0910). SAE Technical Paper.
56. Zhong, L., Singh, I. P., Han, J. S., Lai, M. C., Henein, N. A., & Bryzik, W. (2003). Effect of cycle-to-cycle variation in the injection pressure in a common rail diesel injection system on engine performance (No. 2003-01-0699). SAE Technical Paper.
57. Catania, A. E., Ferrari, A., Manno, M., & Spessa, E. (2008). Experimental investigation of dynamics effects on multiple-injection common rail system performance. Journal of Engineering for Gas Turbines and Power, 130(3).
58. Payri, F., Margot, X., Patouna, S., Ravet, F., & Funk, M. (2009). A CFD study of the effect of the needle movement on the cavitation pattern of diesel injectors (No. 2009-24-0025). SAE Technical Paper.
59. Viera, J. P., Payri, R., Swantek, A. B., Duke, D. J., Sovis, N., Kastengren, A. L., & Powell, C. F. (2016). Linking instantaneous rate of injection to X-ray needle lift measurements for a direct-acting piezoelectric injector. Energy Conversion and Management, 112, 350-358.
60. Arcoumanis, C., Flora, H., Gavaises, M., Kampanis, N., & Horrocks, R. (1999). Investigation of cavitation in a vertical multi-hole injector. SAE transactions, 661-678.
61. Desantes, J. M., Salvador, F. J., Carreres, M., & Martínez-López, J. (2015). Large-eddy simulation analysis of the influence of the needle lift on the cavitation in diesel injector nozzles. Proceedings of the Institution of Mechanical Engineers, Part D: Journal of Automobile Engineering, 229(4), 407-423.
62. Devassy, B. M., Edelbauer, W., & Greif, D. (2015). Numerical simulation of the effect of 3D needle movement on cavitation and spray formation in a Diesel injector. In Journal of Physics: Conference Series (Vol. 656, No. 1, p. 012092). IOP Publishing.
63. Meister, G. F., Alajbegovic, A., Lai, M. C., & Yoo, J. H. (2002). Transient simulation of DGI engine injector with needle movement (No. 2002-01-2663). SAE Technical Paper.
64. Chiavola, O., & Palmieri, F. (2007). Modeling needle motion influence on nozzle flow in high pressure injection system (No. 2007-01-0250). SAE Technical Paper.
65. Chaves, H., Kirmse, C., & Obermeier, F. (2004). Velocity measurements of dense diesel fuel sprays in dense air. Atomization and sprays, 14(6).
66. Chaves, H., Kirmse, C., & Obermeier, F. (2000, October). The influence of nozzle inlet curvature on unsteady cavitation in transparent diesel injection nozzles. In Proc. 1st International Colloquium on Microhydrodynamics, Paris, France.

67. Kirmse, C., Chaves, H., & Obermeier, F. (2004). Spray Velocity Measurements of a Common-Rail Injection System at High Gas Density by Correlation Velocimetry. Proceedings 19th ILASS Europe, 260-265.
68. Miranda, R., Chaves, H., Martin, U., & Obermeier, F. (2003). Cavitation in a transparent real size VCO injection nozzle. Proceedings of ICLASS, Sorrento Italy.
69. Badock, C. (1998). Fundamental study of the influence of cavitation on the internal flow and atomization of diesel sprays. Proc. Thirteenth Institute for Liquid Atomization and Spray Systems-Europe, 224-229.
70. Badock, C., Wirth, R., Fath, A., & Leipertz, A. (1999). Investigation of cavitation in real size diesel injection nozzles. International journal of heat and fluid flow, 20(5), 538-544.
71. Som, S., Aggarwal, S. K., El-Hannouny, E. M., & Longman, D. E. (2010). Investigation of nozzle flow and cavitation characteristics in a diesel injector. Journal of Engineering for Gas Turbines and Power, 132(4).
72. Soriano, O., Sommerfeld, M., & Burkhardt, A. (2008, September). Validation of a cavitation and turbulence induced model for the primary breakup of diesel jets. In ILASS-Europe 2008, 21 Annual Conference on Liquid Atomization and Spray Systems.
73. Amirante, R., Catalano, L. A., & Coratella, C. (2013). A new optical sensor for the measurement of the displacement of the needle in a common rail injector (No. 2013-24-0146). SAE Technical Paper.
74. Amirante, R., Coratella, C., Distaso, E., Rossini, G., & Tamburrano, P. (2017). Optical device for measuring the injectors opening in common rail systems. International Journal of Automotive Technology, 18(4), 729-742.
75. Coppo, M., Dongiovanni, C., & Negri, C. (2007). A Linear optical sensor for measuring needle displacement in common-rail diesel injectors. Sensors and Actuators A: Physical, 134(2), 366-373.
76. Sienkiewicz, F., & Shukla, A. (1997). A simple fiber-optic sensor for use over a large displacement range. Optics and lasers in engineering, 28(4), 293-304.
77. He, G., Patania, A., Kluzner, M., Vokovich, D., Astrakhan, V., Wall, T., & Wlodarczyk, M. (1993). Low-cost spark plug-integrated fiber optic sensor for combustion pressure monitoring (No. 930853). SAE Technical Paper.
78. Molin, D., Achten, F., Van Meer, W., Medawar, A., Kuyt, G., Boon, M., & Sillard, P. (2009). Multimode fiber bending sensitivity for multi-gigabit Ethernet application. In Proc. 58th International Wire & Cable Symposium, Charlotte, NC, USA (p. 442).
79. Martins, A., Rocha, A. M., Neto, B., Teixeira, A. L. J., Facão, M., Nogueira, R. N., ... & Andre, P. S. (2009). Modeling of Bend Losses in Single-Mode Optical Fibers. Institutu de Telecomunicacoes, Portugal, 3.
80. King, S. (2008). Luminous Intensity of an LED as a Function of Input Power. ISB J. Phys, 2(2), Paper-number.
81. Battistoni, M., Xue, Q., Som, S., & Pomraning, E. (2014). Effect of off-axis needle motion on internal nozzle and near exit flow in a multi-hole diesel injector. SAE international Journal of Fuels and Lubricants, 7(1), 167-182.

82. Chiavola, O., & Palmieri, F. (2017). On a Modified VCO Nozzle Layout for Diesel Common Rail Injectors under Actual Needle Displacement. Energy Procedia, 126, 1027-1034.
83. Chiatti, G., Chiavola, O., Frezzolini, P., & Palmieri, F. (2017). On the link between diesel spray asymmetry and off-axis needle displacement. Applied Sciences, 7(4), 375.
84. Chiatti, G., Chiavola, O., Palazzoni, M., & Palmieri, F. (2015). Diesel spray modeling under off-Axis needle displacement (No. 2015-01-0922). SAE Technical Paper.
85. Palmieri, F. (2013). The influence of actual layout and off-axis needle stroke on diesel nozzle flow under ballistic needle displacement. Journal of engineering for gas turbines and power, 135(10).
86. Zhang, X., Liu, J., & Wang, J. (2016). Effect of fuel and nozzle geometry on the off-axis oscillation of needle in diesel injectors using high-speed X-ray phase contrast imaging. Journal of Instrumentation, 11(05), C05015.
87. Huang, W., Moon, S., Gao, Y., Li, Z., & Wang, J. (2017). Eccentric needle motion effect on near-nozzle dynamics of diesel spray. Fuel, 206, 409-419.
88. Churchill, S. W. (1988). The Practical Use of Theory-Viscous Flows.
89. Mitroglou, N., Gavaises, M., & Arcoumanis, D. (2012). Spray stability from VCO and a new Diesel nozzle design concept. In Fuel Systems for IC Engines (pp. 279-290). Woodhead Publishing.
90. Torelli, R., Matusik, K. E., Sforzo, B. A., & Kastengren, A. L. (2018, May). In-Nozzle Cavitation-Induced Orifice-to-Orifice Variations Using Real Injector Geometry and Gasoline-Like Fuels. In in 10th International Symposium on Cavitation (CAV2018), Baltimore MD, USA.
91. Torelli, R., Sforzo, B. A., Matusik, K. E., Kastengren, A. L., Fezzaa, K., Powell, C. P., ... & Traver, M. (2018, July). Investigation of shot-to-shot variability during short injections. In Proceedings of the 14th Triennial International Conference on Liquid Atomization and Spray Systems (pp. 22-26).
92. Torelli, R., Matusik, K. E., Nelli, K. C., Kastengren, A. L., Fezzaa, K., Powell, C. F., ... & Traver, M. (2018). Evaluation of shot-to-shot in-nozzle flow variations in a heavy-duty diesel injector using real nozzle geometry. SAE International Journal of Fuels and Lubricants, 11(4), 379-396.
93. Magnotti, G. M. (2017). Modeling the influence of nozzle-generated turbulence on diesel sprays (Doctoral dissertation, Georgia Institute of Technology).
94. Powell, C. F., Kastengren, A. L., Liu, Z., & Fezzaa, K. (2011). The effects of diesel injector needle motion on spray structure. Journal of Engineering for Gas Turbines and Power, 133(1).
95. Najafi, M., Elhami, B., Ommi, F., & Pour, V. F. (2012). Modeling and Experimental Investigation of Injection Process in Micro motor Combustion Chamber of Liquid Fuel Missile. European Journal of Experimental Biology, 2(5), 1807-1819.
96. Duke, D. J., Kastengren, A. L., Matusik, K. E., Swantek, A. B., Powell, C. F., Payri, R., ... & Parrish, S. (2017). Internal and near nozzle measurements of Engine Combustion Network “Spray G” gasoline direct injectors. Experimental Thermal and Fluid Science, 88, 608-621.

97. Pos, R., Wardle, R., Cracknell, R., & Ganippa, L. (2017). Spatio-temporal evolution of diesel sprays at the early start of injection. Applied Energy, 205, 391-398.
98. Li, Y., & Xu, H. (2016). Experimental study of temporal evolution of initial stage diesel spray under varied conditions. Fuel, 171, 44-53.
99. Wang, Z., Ma, X., Jiang, Y., Li, Y., & Xu, H. (2017). Influence of deposit on spray behaviour under flash boiling condition with the application of closely coupled split injection strategy. Fuel, 190, 67-78.
100. https://scialert.net/fulltext/?doi=jas.2010.107.115
101. Wang, Z., Ding, H., Wyszynski, M. L., Tian, J., & Xu, H. (2015). Experimental study on diesel fuel injection characteristics under cold start conditions with single and split injection strategies. Fuel processing technology, 131, 213-222.
102. Armas, O., Martínez-Martínez, S., Mata, C., & Pacheco, C. (2016). Alternative method for bulk modulus estimation of Diesel fuels. Fuel, 167, 199-207.
103. Rodriguez-Anton, L. M., Casanova-Kindelan, J., & Tardajos, G. (2000). High pressure physical properties of fluids used in diesel injection systems. SAE transactions, 2155-2165.
104. Das, M., Sarkar, M., Datta, A., & Santra, A. K. (2018). Study on viscosity and surface tension properties of biodiesel-diesel blends and their effects on spray parameters for CI engines. Fuel, 220, 769-779.
105. Coratella, C., Parry, L., Sahu, A., & Xu, H. (2019). Optical Sensor for the Needle Lift Detection in the Common Rail Injector (No. 2019-24-0193). SAE Technical Paper.
106. Wang, C., Xu, H., Daniel, R., Ghafourian, A., Herreros, J. M., Shuai, S., & Ma, X. (2013). Combustion characteristics and emissions of 2-methylfuran compared to 2, 5-dimethylfuran, gasoline and ethanol in a DISI engine. Fuel, 103, 200-211.
107. Zhao, H., Holladay, J. E., Brown, H., & Zhang, Z. C. (2007). Metal chlorides in ionic liquid solvents convert sugars to 5-hydroxymethylfurfural. Science, 316(5831), 1597-1600.
108. Zhong, S., Daniel, R., Xu, H., Zhang, J., Turner, D., Wyszynski, M. L., & Richards, P. (2010). Combustion and emissions of 2, 5-dimethylfuran in a direct-injection spark-ignition engine. Energy & Fuels, 24(5), 2891-2899.
109. Daniel, R., Tian, G., Xu, H., Wyszynski, M. L., Wu, X., & Huang, Z. (2011). Effect of spark timing and load on a DISI engine fuelled with 2, 5-dimethylfuran. Fuel, 90(2), 449-458.
110. Brassat, A., Thewes, M., Müther, M., Pischinger, S., Lee, C., Fernandes, R. X., ... & Uygun, Y. (2012). Analysis of the effects of certain alcohol and furan-based biofuels on controlled auto ignition (No. 2012-01-1135). SAE Technical Paper.
111. Wang, C., Xu, H., & Lattimore, T. (2013). Impacts of Low-Level 2-Methylfuran Content in Gasoline on DISI Engine Combustion Behavior and Emissions (No. 2013-01-1317). SAE Technical Paper.
112. Hoppe, F., Burke, U., Thewes, M., Heufer, A., Kremer, F., & Pischinger, S. (2016). Tailor-Made Fuels from Biomass: Potentials of 2-butanone and 2-methylfuran in direct injection spark ignition engines. Fuel, 167, 106-117.

113. Wei, H., Feng, D., & JiaYing, P. A. N. (2017). Effects of Multiple Parameters on Cyclic Variation of a SI Engine Fueled with 2-Methylfuran Gasoline Blends (No. 2017-01-0654). SAE Technical Paper.
114. Ma, X., Jiang, C., Xu, H., Ding, H., & Shuai, S. (2014). Laminar burning characteristics of 2-methylfuran and isooctane blend fuels. Fuel, 116, 281-291.
115. Zhang, Q., Chen, G., Zheng, Z., Liu, H., Xu, J., & Yao, M. (2013). Combustion and emissions of 2, 5-dimethylfuran addition on a diesel engine with low temperature combustion. Fuel, 103, 730-735.
116. Esteban, B., Riba, J. R., Baquero, G., Rius, A., & Puig, R. (2012). Temperature dependence of density and viscosity of vegetable oils. Biomass and bioenergy, 42, 164-171.
117. Jężak, S., Dzida, M., & Zorębski, M. (2016). High pressure physicochemical properties of 2-methylfuran and 2, 5-dimethylfuran–second generation biofuels. Fuel, 184, 334-343.
118. Zhmud, B. (2014). Viscosity blending equations. Lube Mag, 121, 24-9.
119. Coratella, C., Sahu, A., Parry, L., Xu, H., & Ma, X. (2020). Experimental investigation of the orifice-to-orifice variability in jet velocities in a diesel injector. Fuel, 280, 118353.
120. Pontoppidan, M., Ausiello, F., Bella, G., & Ubertini, S. (2004). Study of the impact on the spray shape stability and the combustion process of supply pressure fluctuations in CR-diesel injectors. SAE transactions, 15-41.
121. Herfatmanesh, M. R., Peng, Z., Ihracska, A., Lin, Y., Lu, L., & Zhang, C. (2016). Characteristics of pressure wave in common rail fuel injection system of high-speed direct injection diesel engines. Advances in Mechanical Engineering, 8(5), 1687814016648246.
122. Ubertini, S. (2006). Injection pressure fluctuations model applied to a multidimensional code for diesel engines simulation.
123. de Risi, A., Naccarato, F., & Laforgia, D. (2005). Experimental analysis of common rail pressure wave effect on engine emissions (No. 2005-01-0373). SAE Technical Paper.
124. Hong, S., Shin, J., Park, I., Sunwoo, M., Jeon, J., & Choi, C. (2013). Robust common rail pressure control algorithm for light-duty diesel engines. IFAC Proceedings Volumes, 46(21), 717-722.
125. Wang, H. P., Zheng, D., & Tian, Y. (2016). High pressure common rail injection system modeling and control. ISA transactions, 63, 265-273.
126. Gupta, V. K., Zhang, Z., & Sun, Z. (2011). Modeling and control of a novel pressure regulation mechanism for common rail fuel injection systems. Applied Mathematical Modelling, 35(7), 3473-3483.
127. Li, P., Zhang, Y., Li, T., & Xie, L. (2015). Elimination of fuel pressure fluctuation and multi-injection fuel mass deviation of high pressure common-rail fuel injection system. Chinese Journal of Mechanical Engineering, 28(2), 294-306.
128. Robinson, B., Bennett, J., & Kilgore, J. (1998). U.S. Patent No. 5,845,621. Washington, DC: U.S. Patent and Trademark Office.

129. Kawano, T., Yoshinaga, T., Tanaka, K., Kanehara, K., Nakase, Y., Takeyama, M., ... & Imamura, T. (2002). U.S. Patent No. 6,401,691. Washington, DC: U.S. Patent and Trademark Office.
130. Usui, S., Tamura, S., Miyazaki, K., Takahashi, S., Suganami, M., & Hashida, M. (2013). U.S. Patent No. 8,393,881. Washington, DC: U.S. Patent and Trademark Office.
131. Kilgore, J. T., & Robinson, B. S. (2001). U.S. Patent No. 6,314,942. Washington, DC: U.S. Patent and Trademark Office.
132. Tsuchiya, H., Ogata, T., Mizuno, K., Takikawa, K., Serizawa, Y., Imura, I., & Nishizawa, H. (2005). U.S. Patent No. 6,901,913. Washington, DC: U.S. Patent and Trademark Office.
133. Eshleman, E. S., & Shuler, D. C. (1997). U.S. Patent No. 5,617,827. Washington, DC: U.S. Patent and Trademark Office.
134. Shames, I.H. and Shames, I.H., 1982. Mechanics of fluids (Vol. 2). New York: McGraw-Hill.
135. Das, M., Sarkar, M., Datta, A., & Santra, A. K. (2018). Study on viscosity and surface tension properties of biodiesel-diesel blends and their effects on spray parameters for CI engines. Fuel, 220, 769-779.
136. da Silva Jr, J. L., & Aznar, M. (2014). Thermophysical properties of 2, 5-dimethylfuran and liquid–liquid equilibria of ternary systems water+ 2, 5-dimethylfuran+ alcohols (1-butanol or 2-butanol or 1-hexanol). Fuel, 136, 316-325.
137. Mejía, A., Segura, H., & Cartes, M. (2013). Isobaric vapor–liquid equilibrium and isothermal interfacial tensions for the system ethanol+ 2, 5-dimethylfuran. Journal of Chemical & Engineering Data, 58(11), 3226-3232.
138. Lomba, L., Giner, B., Lopéz, M. C., Aldea, L., & Lafuente, C. (2014). Thermophysical properties of furfural compounds. Journal of Chemical & Engineering Data, 59(2), 329-338.
139. Bakar, R. A., Ismail, S., & Ismail, A. R. (2008). Fuel injection pressure effect on performance of direct injection diesel engines based on experiment. American Journal of Applied Sciences, 5(3), 197-202.